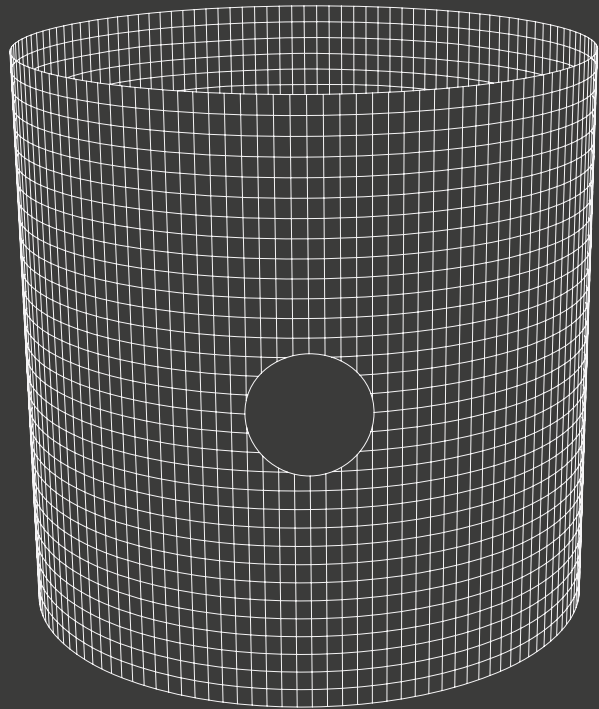
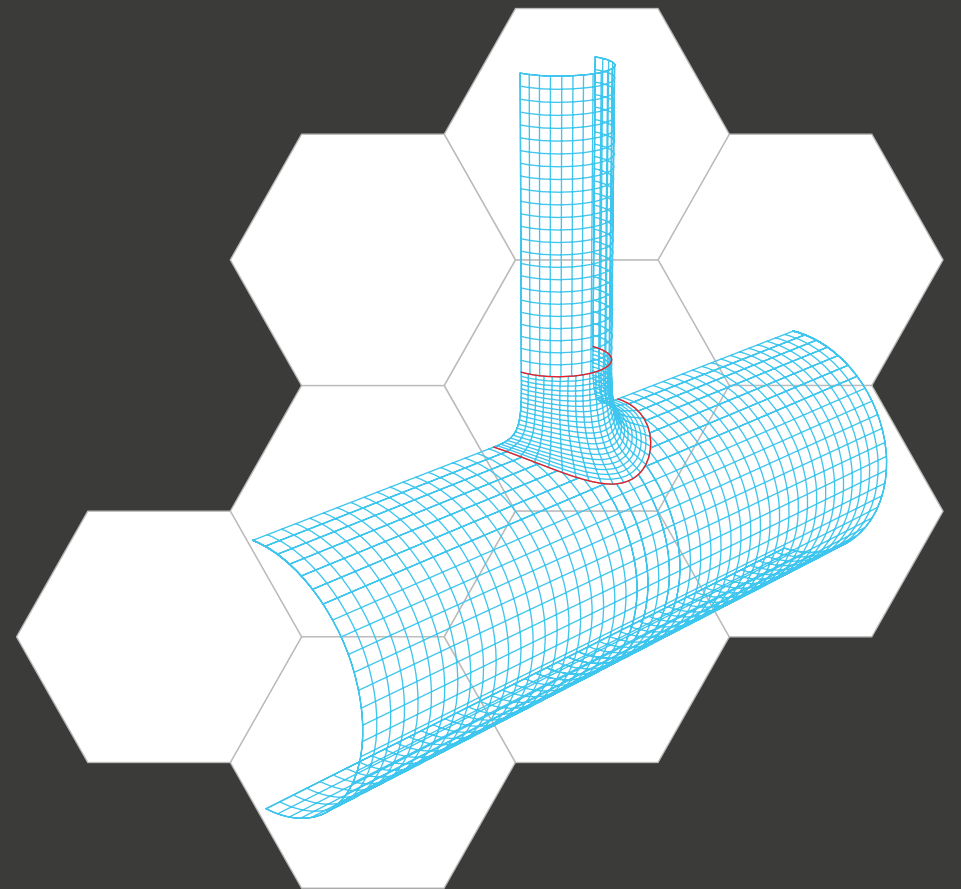


Thin-walled composite structures excel in optimal load-carrying behavior and are of major importance in the design of aerospace structures. Isogeometric analysis is an ideal candidate for the modeling and simulation of shell structures which profit from the exact description of the geometry and from the higher continuity properties of NURBS. The demand for an accurate 3D stress state within laminates is mainly driven by the need to identify and to evaluate potential damage of lamina structures. While a full 3D layerwise (LW) model is computationally expensive, a combined approach considering equivalent-single-layer (ESL) and LW, seems to be a natural choice to tackle the computational costs of increasing model size and model complexity.



Isogeometric Analysis for Thin-walled Composite Structures

## Isogeometric Analysis for Thin-walled Composite Structures



Yujie Guo

 TU Delft

ISBN 978-94-6186-552-6

Yujie Guo

**Isogeometric analysis for thin-walled  
composite structures**



# Isogeometric analysis for thin-walled composite structures

Proefschrift

ter verkrijging van de graad van doctor  
aan de Technische Universiteit Delft,  
op gezag van de Rector Magnificus Prof.ir. K.C.A.M. Luyben,  
voorzitter van het College voor Promoties,  
in het openbaar te verdedigen op  
maandag 18 januari 2016 om 10.00 uur

door

Yujie GUO

Master of Science, Southeast University, Nanjing, China  
geboren te Jiangsu, China

Dit proefschrift is goedgekeurd door de promotor:  
Prof. Dr. C. Bisagni

Co-promotor: Dr.-Ing. habil. M. Ruess

Samenstelling promotiecommissie:

Rector Magnificus	voorzitter
Prof. Dr. C. Bisagni	Technische Universiteit Delft, promotor
Dr.-Ing. habil. M. Ruess	Technische Universiteit Delft, copromotor
Prof. dr. ir. C. Vuik	Technische Universiteit Delft
Prof. Dr.-Ing. habil. S. Klinkel	RWTH Aachen University
Prof. Dr.-Ing. L. De Lorenzis	Technische Universität Braunschweig
Dr. A. Reali, Associate Professor	University of Pavia
Prof. dr. A. Rothwell,	Technische Universiteit Delft, reservelid



Keywords: Isogeometric, Composite Laminates, Layerwise, Thin-walled Structures, Multi-patch, Finite Cell Method

ISBN 978-94-6186-552-6

Copyright ©2016 by Yujie Guo

All rights reserved. No part of the material protected by this copyright notice may be reproduced or utilized in any form or by any means, electronic or mechanical, including photocopying, recording or by any information storage and retrieval system, without written permission of the author.

Printed by Ipskamp Drukkers B.V., Enschede, The Netherlands.  
Typeset by the author with the L<sup>A</sup>T<sub>E</sub>X Documentation System.

大學之道，在明明德，  
在親民，在止于至善。

*The way of great learning consists in manifesting one's bright virtue,  
consists in loving the people,  
consists in stopping in perfect goodness.*

- The Great Learning

By Confucius

Translation by A. Charles Muller

*To my wife and my family*



# Summary

The conceptual ideas behind isogeometric analysis (IGA) are aimed at unifying computer aided design (CAD) and finite element analysis (FEA). Isogeometric analysis employs the non-uniform rational B-spline functions (NURBS) used for the geometric description of a structure to approximate its physical response in an isoparametric sense. Due to the tensor product property of multi-variate NURBS, it is difficult to represent complex topological shapes with a single NURBS patch. Multiple, often non-conforming patches are needed to tackle increasing complexity of the geometry. To further facilitate the modeling of complex shapes and geometric features trimming technology is widely used in CAD software, however, the trimmed domain is only visually unseen and the trimming features can not be utilized directly for the analysis. To overcome these difficulties, extra efforts are needed to make isogeometric methods adapted to engineering related cases.

Thin-walled structures, such as plates and shells, excel in optimal load-carrying behavior and are of major importance in the design of aerospace components and the automotive engineering. Isogeometric analysis is an ideal candidate for the modeling and simulation of shell structures, especially for rotation-free Kirchhoff-Love type shells, which profit from the exact description of the geometry and from the higher continuity properties of NURBS. Furthermore, it favorably supports continuity requirements for flexible through-the-thickness design of laminate composites.

Laminated composite materials are increasingly used in the aerospace industry this asks for reliable and computationally efficient lamina theories. The classical lamination theory belongs to the class of equivalent-single-layer methods (ESL), it is computationally efficient but often fails to capture the 3D stress state accurately. The demand for an accurate 3D stress state within laminates is mainly driven by the need to identify and to evaluate potential damage of lamina structures. While a full 3D layerwise (LW) model is computationally expensive, a combined approach considering both concepts, ESL and LW, seems to be a natural choice to tackle the computational costs of increasing model size and model complexity.

In this thesis, a layerwise method for laminated composite structures is proposed in the framework of isogeometric analysis. A highly accurate prediction of the state of stress for thick and moderately thick laminate composite shells including transverse normal and shear stresses is demonstrated. The layerwise theory is successfully

extended to linear buckling analysis of delaminated composites where a contact formulation is added to eliminate physically inadmissible buckling states which may result from overlapping plies. Furthermore, a Nitsche type formulation is introduced to enforce both weakly, essential boundary conditions and multi-patch coupling constraints for trimmed and non-conforming isogeometric rotation-free Kirchhoff-Love shell patches. The proposed formulation is variationally consistent and excels in a high level of stability and accuracy. A built-in stabilization, used to ensure coercivity of the formulation, prevents ill-conditioning of the physical problem. The inherent trimming problem is tackled with a fictitious domain extension for the trimming domain following the principles of the finite cell method to facilitate the workflow for geometrically complex structures in engineering practice. Computational efficiency is significantly increased with a blended coupling, taking continuum-like shell elements and thin shells elements, according to the theory of Kirchhoff-Love, into account. The blended approach provides access to the full 3D state of stress within selected subdomains while preserving the computational efficiency of the overall analysis.

# Contents

<b>Summary</b>	<b>v</b>
<b>1 Introduction</b>	<b>1</b>
1.1 Background and motivation . . . . .	1
1.2 State of the art . . . . .	3
1.2.1 Design and analysis of laminate composites . . . . .	3
1.2.2 Isogeometric multi-patch modeling . . . . .	5
1.2.3 Analysis with trimmed geometries . . . . .	6
1.3 Thesis layout . . . . .	7
<b>2 Design-through-analysis: the isogeometric analysis framework</b>	<b>9</b>
2.1 Geometric modeling using NURBS . . . . .	11
2.1.1 B-spline functions . . . . .	11
2.1.2 B-spline geometries . . . . .	12
2.1.3 NURBS and NURBS geometries . . . . .	13
2.1.4 Refinement of B-splines and NURBS . . . . .	14
2.2 Isogeometric analysis - basic concept . . . . .	17
2.2.1 Fundamental aspects of continuum mechanics . . . . .	17
2.2.2 NURBS-based isoparametric finite elements . . . . .	21
2.3 The concept of trimming and finite cell method . . . . .	22
<b>3 Isogeometric methods for laminate composites</b>	<b>27</b>
3.1 Equivalent-single-layer methods . . . . .	28
3.2 Layerwise methods . . . . .	29
3.2.1 Layerwise shell model . . . . .	31
3.2.2 Layerwise shell discretization . . . . .	33
3.3 Through-the-thickness modeling . . . . .	34
3.3.1 Cylindrical bending of laminates . . . . .	34
3.3.2 Laminate composite square plate . . . . .	36
3.3.3 Laminate cylindrical shell . . . . .	40
3.4 Trimmed geometries - free edge stress analysis . . . . .	45
3.5 Summary . . . . .	47

<b>4</b>	<b>Multi-lamina-model analysis with delaminations: strong coupling and linear buckling</b>	<b>51</b>
4.1	Strong coupled multi-model approach . . . . .	53
4.1.1	Multi-model stress analysis . . . . .	54
4.1.2	Initial delaminations . . . . .	57
4.2	Linear buckling analysis . . . . .	60
4.2.1	Contact model enriched buckling analysis . . . . .	61
4.3	Buckling of delaminated composites . . . . .	64
4.3.1	Convergence study and contact demonstration . . . . .	65
4.3.2	Midplane delamination of a $[0^\circ/0^\circ]$ laminate . . . . .	68
4.3.3	Influence of the axial location of delamination . . . . .	70
4.3.4	Influence of the contact constraints . . . . .	71
4.3.5	A model with two delaminations . . . . .	72
4.4	Summary . . . . .	74
<b>5</b>	<b>Analysis of multi-patch models for thin-walled structures</b>	<b>77</b>
5.1	Isogeometric rotation-free Kirchhoff-Love shells . . . . .	78
5.1.1	Governing equations and isogeometric discretizations . . . . .	81
5.2	Weakly enforced essential boundary conditions . . . . .	82
5.2.1	Governing equations of the Nitsche extension . . . . .	82
5.2.2	Discretization aspects . . . . .	86
5.2.3	Treatment of trimmed boundaries . . . . .	87
5.3	Weakly enforced coupling constraints . . . . .	88
5.4	Numerical examples: weak boundary conditions . . . . .	90
5.4.1	Scordelis-Lo shell problem . . . . .	90
5.4.2	Bending of an embedded circular plate . . . . .	91
5.5	Numerical examples: weak coupling constraints . . . . .	93
5.5.1	Plate bending – simply supported rectangular domain . . . . .	94
5.5.2	Plate bending – cantilever plate . . . . .	96
5.5.3	Scordelis-Lo roof . . . . .	97
5.5.4	Shell structures with folds – T-beam problem . . . . .	98
5.5.5	Pipe junction under pressure loading . . . . .	101
5.6	Summary . . . . .	103
<b>6</b>	<b>Blending of multi-patch composite shell models</b>	<b>107</b>
6.1	Nitsche’s method for coupling constraints in blended shell models . . . . .	108
6.1.1	Isogeometric solid-like shells . . . . .	108
6.1.2	Nitsche’s extension of coupling constraints . . . . .	108
6.1.3	Blended coupling of composite laminates: evaluation of stabilization constants . . . . .	110
6.2	Numerical examples . . . . .	113
6.2.1	Consideration of refined patches – pinched cylinder problem . . . . .	113
6.2.2	Blended coupling of Scordelis-Lo roof . . . . .	114
6.2.3	Frequency analysis of a stringer stiffened shell panel . . . . .	116

6.2.4	Laminated plate with hole: free edge analysis . . . . .	117
6.2.5	Stiffened cylinder panel with opening . . . . .	119
6.3	Summary . . . . .	121
<b>7</b>	<b>Conclusions and future work</b>	<b>123</b>
7.1	Summary . . . . .	123
7.2	Future work . . . . .	126
<b>A</b>	<b>Derivatives of Kirchhoff-Love shell quantities w.r.t the displacement variables</b>	<b>129</b>
	<b>Bibliography</b>	<b>130</b>
	<b>Acknowledgements</b>	<b>151</b>
	<b>Curriculum Vitae</b>	<b>153</b>
	<b>List of Publications</b>	<b>155</b>



# Chapter 1

## Introduction

### 1.1 Background and motivation

Thin-walled structures are widely used in the aerospace, automotive and shipbuilding industries. Typical applications are fuselage structures, automobile bodies, the hulls of submarines and rockets. With a much better strength-to-weight ratio compared to metallic structures, laminate composites have become increasingly important over the decades in lightweight designs, and have superseded conventional engineering structures in many applications, in particular in aerospace engineering. Laminated composites are made of stackings of fiber reinforced layers with different fiber angles embedded within matrix materials. The layered structures are known to be prone to damage at layer interfaces such as delamination. Other failure modes in composites include matrix cracks, fiber pull-out, intralaminar matrix cracking, fiber/matrix debonding and fiber fracture. The prediction and evaluation of damage and failure in composite laminates demands an accurate evaluation of the three-dimensional state of stress in the critical sub-domains of the composites, however, mathematically, thin-walled structures are often considered as two dimensional surfaces. This geometric reduction is based on a condensation of the three dimensional structural response to certain types of membrane and bending actions. Typically, two dimensional shell models are computationally inexpensive compared to full three dimensional models, but they often fail to capture the three dimensional stress state with sufficient accuracy. In the past, various layerwise concepts have been developed which allow a separate modeling of in-plane and through-the-thickness properties to tackle better the numerical complexity of multi-layer composites for which accurate three-dimensional stress components are needed. Other concepts proposed to reduce the computational cost consider a combination of different mathematical models of different effort-to-accuracy ratios to handle an increasing model size with sufficient efficiency, an approach which is also favoured in the thesis at hand.

Isogeometric analysis (IGA) is an emerging analysis concept proposed by Hughes et al.[1] aimed at unifying computer aided design (CAD) and finite element analysis (FEA). The IGA concept is based on the use of non-uniform rational B-spline (NURBS) functions for both the representation of the geometry model and the approximation of the physical field and state variables of the analysis. NURBS are a standard technology for the representation of geometry in CAD which builds the basis for the traditional modeling of structures applied in FEA. The conflation of CAD and FEA simplifies the modeling and analysis pipeline and supports a more efficient engineering workflow. Compared to the traditional Lagrange-based finite element method, IGA excels with the following superior properties:

- the NURBS used in IGA allow an exact representation of geometry and thus provide highest smoothness properties as desired for contact problems or for the analysis of shells and membranes. The geometry of a finite element model is typically approximated linearly, in a few cases quadratically or cubically.
- the geometry does not change during model refinement which is in contrast to the refinement principles of the finite element method.
- the higher order approximation capabilities of NURBS provide control about the discretization error and allow for exponential rates of convergence where the solution field is smooth. This is in contrast to the prevailing h-refinement of the finite element method which is limited with regard to the model size and which results in algebraic rates of convergence.
- the unique k-refinement in IGA ensures higher order continuity among the elements of a patch up to a degree of  $p-1$  which is in contrast to the intrinsic  $C^0$ -continuity of finite elements.

In particular, the surface model character of NURBS, the higher order approximation and higher order continuity properties, make IGA an excellent candidate for the analysis of thin-walled structures where curved geometries are captured exactly. The superiority of IGA has been demonstrated successfully in other fields, e.g. in solids and structural mechanics [2, 3, 4, 5, 6, 7, 8, 9, 10, 11, 12, 13], in fluid mechanics [14, 15, 16, 17, 18, 19, 20, 21], in structural vibration [22, 23, 24], in thermal analysis [25, 26, 27], in contact mechanics [28, 29, 30, 31, 32, 33], in multi-field problems [34, 35, 36], in design and optimization [37, 38, 39, 40].

Thin-walled structures in engineering practice typically exhibit complex geometries and geometry features, such as holes, openings or stringer folds. The modeling of such geometric features in IGA often requires multiple patches which should be coupled such that displacements and tractions are transferred properly. Furthermore, CAD modelers generally use trimmed NURBS geometries which fade out subdomains for visualization purposes but leave the underlying geometry unchanged. As a result, the trimmed geometry, which is in the focus of the analysis, has no parametric description and cannot be utilized directly for the analysis without special treatment. An isogeometric analysis framework addressing these challenges should be able to deal with both, multiple patches and trimming geometries, to ensure a

seamless integration of CAD and FEA in an engineering design environment. Other aspects supporting the idea of a design-through-analysis framework for laminate composite structures include flexible refinement capabilities which allow simple refinement through the laminate thickness. Considering the two-dimensional surface model characteristic of thin-walled structures, the complete three-dimensional stress state should be accessible in critical subdomains, e.g. at layer interfaces or free edges, to allow for an accurate prediction of strength and failure.

The aim of the research presented in this thesis was to develop a flexible analysis framework for engineering shell structures that supports a design-through-analysis workflow according to the isogeometric analysis paradigm [41]. At the heart of this thesis lies the numerically efficient, accurate and reliable modeling and analysis of laminate composite shells as increasingly used in innovative primary aerospace structures. The thesis revisits the most attractive properties of isogeometric analysis for shell structures, reveals critically the major challenges of NURBS-based analysis models and proposes a solution approach which overcomes the currently existing severe limitations of isogeometric analysis and the related workflow for arbitrary structures of engineering relevance.

## 1.2 State of the art

The state-of-the-art discussion that follows covers various fields of research and is presented topic-wise and then merged in the course of the thesis, enhanced by new aspects and developments, to produce an engineering design tool.

### 1.2.1 Design and analysis of laminate composites

Due to their strength and light-weight, laminate composites are becoming increasingly attractive in many engineering fabrication areas, from military to civil applications and from high-cost to low-cost products. The following examples are typical representatives of today's application domains for composites, cf. Figure 1.1: the Boeing 787 Dreamliner, the Airbus A350 commercial aircraft, wind turbine blades, car passenger cabins, tennis rackets, offshore platforms and pipelines. Through careful design of laminated composites, the weight of a structure can often be greatly reduced while maintaining its strength and stability. Today's research activities with respect to laminated composite structures cover a broad range of areas: stress analysis [42, 43, 44, 45, 46] to study possible damages of the structure; dynamic responses [47, 48, 49, 50] to reveal frequency properties and the performance of composites under cyclic loading; thermal analysis [51, 52, 53, 54] to understand high temperature gradient effects such as those commonly seen in engines; damage prediction and propagation [55, 56, 57, 58] investigating damage mechanisms and the influence of the stacking sequences; fatigue [59, 60, 61, 62] to predict the failure properties of composite structures under periodic loading; structural stability [63, 64, 65, 66, 67]



(a) Boeing 787



(b) Boeing 787 noses ahead



(c) Composite wing

Figure 1.1: Commercial aircraft using composites. (a) Boeing 787 (Source: <http://www.boeing.com>), (b) composite fuselage (Source: <http://www.lambolab.org>), (c) composite wing (Source: <http://www.renishaw.com>).

where the buckling behavior and buckling loads are investigated; design and optimization [68, 69, 70, 71] of structures to find the optimal shape or sizes for given constraints.

The industrial importance of laminate composites has been boosted significantly by the further development and application of advanced manufacturing techniques such as automated fiber placement (AFP) machines. In parallel to this development, intensive research, experimental and simulation-based, has driven the development of this technology to a level which provides insight into the physical mechanisms on multiple scales. In particular, computer simulations, classically governed by the finite element method, reveal on one hand physical insight across the scales and provide on the other hand an attractive extension to experiments to accelerate and to economize the design circle of a product.

The finite element method originated in the early 1950s, and in parallel, computer aided design evolved steadily at the end of the same decade. The different fields of application, namely computer aided geometric design and engineering design, gave rise to the independent development of the two technologies resulting in different, and in general incompatible, model descriptions. Although various efforts have been made over the decades to integrate finite element analysis and computer aided design, a large gap still exists in the treatment of geometry in the two worlds. The typical

work flow for the analysis of structures includes several steps which are dominated by a CAD design, by mesh generation and finally by the numerical analysis. It is estimated that almost 80% of the time effort within this workflow is devoted to the analysis-suited model preparation and mesh generation [1]. In 2005, isogeometric analysis was proposed by HUGHES ET AL. [1, 22, 72] to bridge this gap and to eliminate the need for intermediate data transfer and data transformation between a CAD and FEA software environment which would greatly facilitate the entire design-through-analysis work flow in engineering.

Given the early state of development of isogeometric analysis, the practical use in engineering with a focus on laminate composites demands further attention and more effort must be made to provide the envisaged workflow. First attempts in the framework of laminate composites have been made to harness the potential of isogeometric analysis. The implementation of different lamina theories using an isogeometric method are discussed in [73, 74, 75, 76, 77, 78]; free vibration and linear buckling analysis of laminated composites are studied in [79, 80, 81]; geometrically nonlinear analysis and postbuckling analysis of laminated plates are investigated in [82, 83] respectively; special attention is paid to interlaminar stress calculations in [78, 84, 85]; delamination simulation with cohesive elements is reported in [86]; and the modeling of continuum damage in rotation-free composite shells is demonstrated in [12]. The application of isogeometric analysis in design and optimization of composite laminates is reported in [87, 88, 89]. The majority of papers mentioned above deal with simple geometries, which indicates that further investigations are needed with respect to the modeling of complex geometric structures and the simulation of different physical phenomena of laminates.

## 1.2.2 Isogeometric multi-patch modeling

The number of applications using single-patch NURBS models is limited. With increasing geometric complexity the number of patches needed to represent a structure increases accordingly. Furthermore, engineering relevant structures often consist of many different parts with distinct material properties and must be modeled by a larger number of patches. Topological restrictions of patches which result from the tensor product character of multivariate NURBS geometries or patch-spanning mesh refinement properties are other important aspects which call for modeling with multiple patches.

In multi-patch analysis, the different patches involved need to be connected along their patch interfaces. A strong coupling on the basis of degrees of freedom belonging to the control points of adjacent patches is reported in [90]. This type of coupling is typically restricted to the primal unknowns and ensures in general only  $C^0$ -continuity across the coupled domains. It is also reported that higher order continuity can be achieved by applying similar constraints in the normal direction of coupling interface [90]. Alternatively, the coupling constraints can also be satisfied weakly, i.e. they are satisfied in an integral sense as done in various approaches such as e.g. the penalty

method [91, 92, 93] which is a simple approach in terms of implementation and which does not add extra degrees of freedom to the system equations but which destroys inevitably the well-posedness of the problem; the Lagrange multiplier method [94, 95, 96, 97, 98] which models additional flux unknowns with additional equations to satisfy the coupling constraints; the mortar-type weak substitution method [99, 100] and Nitsche-based methods [101, 102, 103, 104, 105, 106, 107, 108, 109, 110, 111]. Nitsche's approach [101] was first proposed to enforce essential boundary conditions for the Poisson problem and has been adapted successfully for structural mechanics problems [112, 102, 103, 105]; biomechanics [106]; thermo-elasticity [107] and fluid mechanics [108, 110, 111]. Nitsche's method is variationally consistent and does not introduce additional degrees of freedom that need to be solved. The coercivity of the governing problem can be ensured with additional stability terms without compromising the conditioning properties of the algebraic equations. The method has been successfully applied to the weak enforcement of essential boundary conditions of trimmed NURBS patches [104] and to the weak enforcement of coupling constraints of non-matching and non-conforming NURBS patches [113, 109] in the framework of isogeometric analysis and the finite cell method [114].

Recently, special attention has been paid to multi-patch coupling of shell structures. The NURBS patches for thin shells according to the Kirchhoff-Love theory [87, 82, 2] are endpoint interpolatory providing only  $C^0$ -continuity at the coupling interface which results in a hinge effect, i.e. bending moments are not transmitted properly and  $G^1$ -continuity [115] can not be preserved. KIENDL ET AL. [116] propose the use of a bending strip which ensures continuity and which prevents the hinge effect between adjacent Kirchhoff-Love shell patches. The strip has zero membrane stiffness and non-zero bending stiffness only in the direction transverse to the strip. BENSON ET AL. [117] propose a blended shell formulation which combines the Kirchhoff-Love theory with the Reissner-Mindlin theory. This approach enables the elimination of rotational degrees of freedom while it provides an effective treatment of shell intersections and a merge of NURBS patches. In [118], a special method is proposed to deal with shell geometries including kinks using Reissner-Mindlin type elements. In addition to the above mentioned coupling of multiple shell patches, a mixed-dimensional coupling which allows the replacement of two-dimensional sub-domains with three-dimensional patches represents a valuable extension with regard to thin shell theories. The analysis of laminate composite shells is one example where the local replacement of a sub-domain, modeled according to the theory of Kirchhoff-Love, with a layerwise-modeled shell domain allows the evaluation of the three-dimensional stress state, at reasonable computational cost. The full three-dimensional stress state can be utilized for further damage analysis, for example initiation and propagation of delamination phenomena.

### 1.2.3 Analysis with trimmed geometries

Recalling the tensor product properties of NURBS, cf 1.2.2, patch geometries are topologically restricted to simple shapes, i.e. quadrangles in 2D and hexahedrals in

3D. Although topologically more complex shapes, in general, can be divided into multiple simple shapes following a NURBS tensor product, additional modeling effort is needed, in particular, where multiple patches should be joined seamlessly together. In cases where geometric complexity refers to a common plane or body that can be modeled with a single patch the trimming concept will greatly ease the modeling effort. The trimming concept employs boolean operations between various CAD objects to introduce arbitrary cut-outs used for the visual geometry representation. For example, a trimmed surface can be defined by a NURBS surface and a set of NURBS curves on the surface which define trimmed areas, cf. Figure 2.13. The trimming area remains visually unseen and the data structures of original geometries remain unchanged. Using trimmed geometries in isogeometric analysis was first proposed in [119] where a NURBS enhanced integration scheme is adopted for trimmed elements. In [120], a local geometric reconstruction technique was developed to deal with trimmed elements of shell structures and applied to multi-patch shell modeling. Another approach introduced in [121, 122], follows the idea of a fictitious domain representation for the trimmed domain. The approach adopts the fictitious domain-based finite cell method (FCM) [123] which was initially introduced for the analysis of complex problem domains on an embedding Cartesian analysis grid using the approximation space of the p-version of the finite element method [124, 106]. In [121, 125] and later in [122, 41, 104, 113] the approach is further developed and applied to B-splines and NURBS, respectively. In the NURBS-version FCM, the mesh of the fictitious domain is no longer specified on Cartesian grids. Instead, it is adapted to the framework of isogeometric analysis where the smoothness, the higher order and higher continuity properties of NURBS are fully exploited for both the geometry and solution fields of the physical and fictitious extension domain. Another approach for the analysis with trimmed geometries is proposed in [126] where the quadrature rule is adapted to the trimmed domain. In [93], a workflow for the analysis of shell structures based on the B-Rep, boundary representation, is proposed which allow consideration of trimmed NURBS surfaces. A major challenge for trimmed NURBS and boundary fitted NURBS analysis domains is the imposition of essential boundary condition along arbitrary boundary segments. An elegant solution strategy to this problem is the use of a Nitsche-based approach [121, 106, 104]. Other strategies include the penalty method [92] and the Lagrange multiplier method [127, 128, 129].

To conclude, efficient techniques for the enforcement of boundary and coupling constraints and a simple approach to handle trimmed geometries in isogeometric analysis will greatly facilitate the modeling and analysis workflow in future engineering design.

### 1.3 Thesis layout

This thesis is organized as follows: in chapter 1 the background and motivation of the current research is presented, followed by the state of the art in the field of

laminated composites, isogeometric analysis and trimming technologies. Chapter 2 introduces the fundamentals of isogeometric analysis including the definition of B-splines and NURBS, the representation of NURBS geometries, the construction of an approximation basis and related refinement techniques. Furthermore, the conceptual aspects of isogeometric analysis are explained in the context of continuum mechanics. Finally, the trimming concept for CAD geometries are discussed in detail.

The application of isogeometric analysis for laminated composites is presented in chapter 3. Special attention is paid to the through-thickness modeling of laminates where a layerwise method is proposed to capture accurately the transverse shear and normal stresses. A multi-model analysis technique using an equivalent-single-layer approach and a layerwise method in different sub-regions of the structure is introduced in chapter 4. The approach allows for an efficient stress analysis of pre-existing delaminations. In addition, the buckling of laminated composite plate-like structures with pre-existing delamination zones is studied. Physically inadmissible buckling states with overlapping plies are repaired with a step-wise contact analysis to reduce the ply overlap. The fundamentals of thin shells according to the Kirchhoff-Love theory are provided in chapter 5. The weak form of the shell formulation is extended variationally consistent to enforce weakly essential boundary conditions and multi-patch coupling constrains for thin isogeometric shells. Furthermore, the trimming of NURBS geometries is taken into account by the conceptual use of the finite cell method. In chapter 6 a Nitsche-based weak coupling formulation is extended for a blended coupling of thin shell patches with solid-like shell patches, including both, isotropic materials and laminated composites. Finally, conclusions and suggestions for future work are given in chapter 7.

## Chapter 2

# Design-through-analysis: the isogeometric analysis framework

In the standard workflow of a finite element analysis (FEA), cf. top branch of Figure 2.1, the geometry of the model is designed and generated in a computer aided geometric design (CAGD) environment and exchanged with other computer aided engineering (CAE) applications in standard file formats, like *iges*<sup>1</sup>. The designed geometry often contains certain ambiguities and small features, such as gaps between different patches or a chamfer at corners, which are undesired features for mesh generation and which should be repaired and defeatured before further used in the modeling pipeline. The modified geometry is called *Analysis Suitable Geometry (ASG)* [90]. On the basis of the ASG, an analysis-suited mesh is generated which approximates the geometry. In general, linear Lagrange polynomials are used to interpolate the mesh geometry which introduces a geometric discretization error. Additionally, the volume of a solid model in CAGD is often represented as a union of water-tight boundary surfaces, called boundary representation (*b-rep*) [131]. Hence, the volumetric mesh of a solid model is generated based on a boundary surface tessellation or meshes and does not provide a parametric description of the solid's interior. It is worth noting that shell structures which can be described solely with surfaces do not suffer from the aforementioned problems.

In [132] it was reported that commonly 57% of the overall analysis time is spent on the generation of an analysis-suited geometry and another 20% is needed for mesh generation. Considering the typical scenario of repeated modifications during the design phase, this modeling effort of almost 80% of the overall analysis time

---

<sup>1</sup>*iges* denotes “initial graphics exchange specification”, and is a neutral data format for the transmission of CAD data between dissimilar CAD/CAE systems [130].

becomes even more dramatic. A more tight connection between geometric modeling and the actual analysis, a connection that omits defeaturing, geometry repair and mesh generation, would significantly ease this enormous, labour intensive modeling step.

Isogeometric analysis (IGA) represents a conceptual renewal of the established modeling and analysis workflow which conflates CAD and FEM by employing the basis used for the geometric representation as an appropriate approximation basis for the numerical analysis. CAD-derived NURBS geometries typically represent the coarsest available mesh instance and need further refinement to ensure a sufficiently high quality of the analysis results. One of the unique features of NURBS-based IGA is that the refinement of a NURBS basis does not change the geometry model, cf. bottom branch of Figure 2.1. Besides the classical  $h$ - and  $p$ -refinement, IGA provides a unique continuity preserving  $k$ -refinement. In [133, 134], it is demonstrated that the higher continuity  $k$ -refinement poses better approximation properties on a per-degree-of-freedom basis compared to its  $h$ - and  $p$ -refinement counterparts. The details of the various types of refinement using NURBS will be explained in the following sections.

In this chapter, the fundamentals of B-splines and NURBS are introduced in 2.1. The introduction of continuum mechanics and the basic concept of isogeometric analysis are presented in 2.2. The strategy used to deal with trimmed geometries in CAGD is discussed and a possible solution to the problem of trimmed geometries using the finite cell method (FCM) is explained in 2.3.

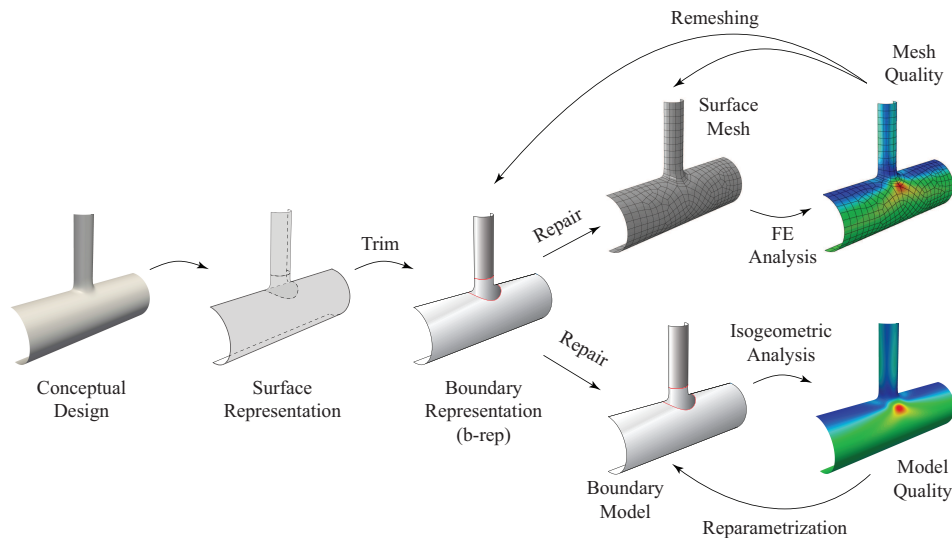


Figure 2.1: Comparison of analysis process of traditional finite element method (top branch) and isogeometric analysis (bottom branch).

## 2.1 Geometric modeling using NURBS

In this section, the fundamentals and basic properties of B-spline and NURBS basis functions are presented and their use for the constructions of line and surface geometries is discussed.

### 2.1.1 B-spline functions

In 1D, a B-spline basis of polynomial order  $p$  is defined by  $n$  basis functions  $N_{i,p}(\xi)$  ( $i = 1, \dots, n$ ) in the parameter space  $\xi$ . The functions  $N_{i,p}(\xi)$  are specified by a knot vector

$$\Xi = \xi_1, \dots, \xi_{n+p+1}, \quad \xi_1 \leq \xi_2 \leq \dots \leq \xi_{n+p+1} \quad (2.1)$$

consisting of a non-decreasing sequence of coordinates  $\xi_i$ , denoted as knots. The construction of the B-spline basis follows the *Cox-de-Boor* recursion formula [135, 72], and starts from degree  $p = 0$ :

$$N_{i,0}(\xi) = \begin{cases} 1 & \text{if } \xi_i \leq \xi < \xi_{i+1} \\ 0 & \text{otherwise} \end{cases} \quad (2.2)$$

$$N_{i,p}(\xi) = \frac{\xi - \xi_i}{\xi_{i+p} - \xi_i} N_{i,p-1}(\xi) + \frac{\xi_{i+p+1} - \xi}{\xi_{i+p+1} - \xi_{i+1}} N_{i+1,p-1}(\xi) \quad (2.3)$$

The functions  $N_{i,p}(\xi)$  are piecewise defined over  $p + 1$  knot-spans forming a  $C^{p-1}$  continuously differentiable basis. Repeated knots lower the continuity of the basis functions. A knot multiplicity of  $p + 1$  for the first and last knot makes the basis interpolatory resulting in a B-spline patch with *open* knot vector, cf. Figure 2.2. B-spline functions satisfy the partition of unity property and ensure linear inde-

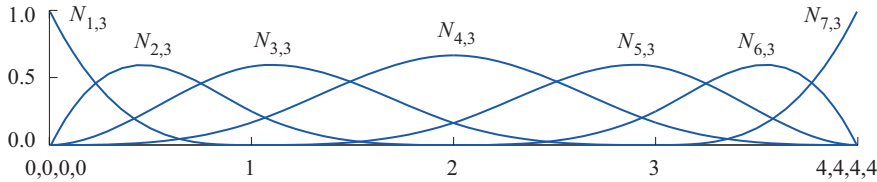


Figure 2.2: 1D cubic B-spline shape functions  $N_{i,3}$  ( $i = 1, \dots, 7$ ) across an *open* knot vector of four knot-span-elements.

pendence. Compared to Lagrange polynomials, B-spline functions are non-negative  $N_{i,p}(\xi) \geq 0$  and  $C^{p-1}$  continuous at the element boundaries.

A multi-variate B-spline basis, for example of dimension three, is constructed by the tensor product  $\Xi \times \mathcal{H} \times \mathcal{Z}$  of univariate B-spline basis functions, defined by

the knot vectors  $\Xi = \{\xi_1, \xi_2, \dots, \xi_{n+p+1}\}$ ,  $\mathcal{H} = \{\eta_1, \eta_2, \dots, \eta_{m+p+1}\}$  and  $\mathcal{Z} = \{\zeta_1, \zeta_2, \dots, \zeta_{l+p+1}\}$  [72, 136]. Each shape function is specified as:

$$Q_{ijk,p}(\xi, \eta, \zeta) = N_{i,p_1}(\xi) M_{j,p_2}(\eta) L_{k,p_3}(\zeta) \quad (2.4)$$

where  $N_{i,p_1}(\xi)$ ,  $M_{j,p_2}(\eta)$  and  $L_{k,p_3}(\zeta)$  are 1D basis functions of polynomial degree  $p_s$  in each parametric direction  $s \in \{1, 2, 3\}$ , respectively, and where  $i$ ,  $j$  and  $k$  indicate the position of basis functions within the product space.

### 2.1.2 B-spline geometries

B-spline geometries follow from a linear combination of control points  $\mathbf{P} \in \mathbb{R}^d$ , where  $d$  denotes the geometric dimension, with the corresponding set of B-spline basis functions. A B-spline curve is defined as:

$$\mathbf{c}(\xi) = \sum_{i=1}^n N_{i,p}(\xi) \mathbf{P}_n \quad (2.5)$$

where  $n$  is the number of basis functions,  $\mathbf{P}_n$  is the position vector of the  $n$ -th control point. An example of a cubic B-spline curve is shown in Figure 2.3 where the red

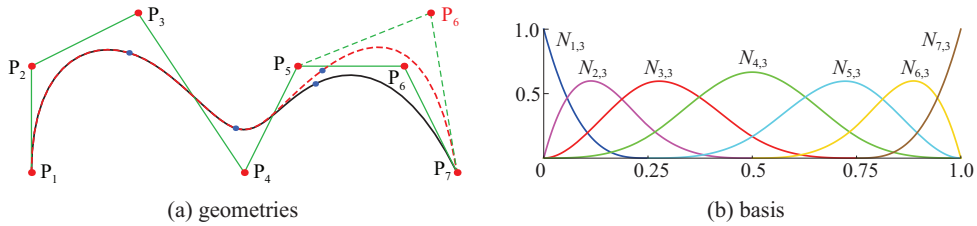


Figure 2.3: An example of cubic B-spline curve where the dashed identities represent the curve and control polygon due to the movement of control point  $\mathbf{P}_6$  (a), corresponding basis functions with knot vector  $\Xi = \{0, 0, 0, 0, 0.25, 0.5, 0.75, 1, 1, 1, 1\}$  (b).

points are the control points and where the blue points are physical points on the curve corresponding to the internal knots of the knot vector. At the two ends of the curve, the control points are interpolatory due to a  $p$ -fold knot repetition. A control polygon, shown in green, is obtained from linear interpolation between the control points with tangential orientation at the end points of the polygon. The corresponding B-spline curve conforms to the strong convex hull property for which the curve is self-contained in the convex hull of its local control polygon. It is this property which leads the local support phenomenon [72]. The local support property of B-splines is shown in Figure 2.3 where the position of control point  $\mathbf{P}_6$  is changed resulting in a locally confined modification of the geometry, see the dashed red curve. The influential segments of the  $i^{th}$  control point  $\mathbf{P}_i$  spread across the knot span  $[\xi_i, \xi_{i+p+1}]$ .

Following the tensor product property of a multi-variate B-spline basis, the definition of a B-spline surface reads:

$$\mathbf{r}(\xi, \eta) = \sum_m Q_{m,p}(\xi, \eta) \mathbf{P}_m \quad (2.6)$$

where  $m = m(i, j)$  and  $\mathbf{P}_m \in \mathbb{R}^3$  and  $\mathbf{r}$  the surface coordinates referred to the global coordinate system. An example of a B-spline surface is shown in Figure 2.4. The

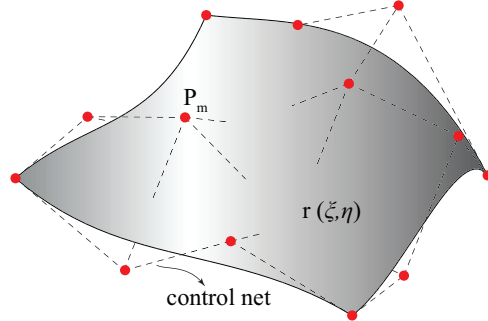


Figure 2.4: Example of B-spline surface with control net and control points.

construction of a B-spline solid follows in analogy to the B-spline surface and hence is not discussed further here.

### 2.1.3 NURBS and NURBS geometries

Non-uniform rational B-splines (NURBS) are a generalization of B-splines that allow the exact geometric representation of entities which cannot be represented by B-splines, such as circles, spheres or tori. Such conic sections can be constructed from B-splines by a piecewise projective transformation of the B-spline curve leading to rational functions. The definition of the NURBS basis function reads:

$$R_{i,p}(\xi) = \frac{w_i N_{i,p}(\xi)}{\sum_{\hat{i}=1}^n w_{\hat{i}} N_{\hat{i},p}(\xi)} \quad (2.7)$$

where  $w_i$  is the weight assigned to the  $i^{th}$  basis function. Multi-variate NURBS basis functions are constructed in analogy to (2.4) by a  $d$ -dimensional tensor product. As an example, the definition of 3D NURBS basis function reads:

$$R_{m,p}(\xi, \eta, \zeta) = \frac{w_{ijk} N_{i,p_1}(\xi) M_{j,p_2}(\eta) L_{k,p_3}(\zeta)}{\sum_{\hat{i}=1}^{n_1} \sum_{\hat{j}=1}^{n_2} \sum_{\hat{k}=1}^{n_3} w_{\hat{i}\hat{j}\hat{k}} N_{\hat{i},p_1}(\xi) M_{\hat{j},p_2}(\eta) L_{\hat{k},p_3}(\zeta)} \quad (2.8)$$

The NURBS basis has all the properties of B-spline basis functions, for example, partition of unity, continuity and non-negative etc.

The definition of a NURBS-based curve follows in analogy to (2.5) and reads:

$$\mathbf{c}(\xi) = \sum_{i=1}^n R_{i,p}(\xi) \mathbf{P}_i \quad (2.9)$$

with  $R_{i,p}(\xi)$  defined in (2.7).

From a geometric point of view, the definition of NURBS geometries in  $\mathbb{R}^d$  follow from a projective transformation of B-spline entities in  $\mathbb{R}^{(d+1)}$  [137, 135, 138], see Figure 2.5. The geometry of the B-spline curve is obtained through interpolation of homogeneous control points with B-spline basis functions:

$$\mathbf{c}^w(\xi) = \sum_{i=1}^n N_{i,p}(\xi) \mathbf{P}_i^w \quad (2.10)$$

where

$$\mathbf{P}_i^w = \begin{pmatrix} \mathbf{P}_i w_i \\ w_i \end{pmatrix} \quad (2.11)$$

and where finally the projected NURBS curve reads:

$$\mathbf{c}(\xi) = \frac{[\mathbf{c}^w(\xi)]_j}{w(\xi)} \quad (2.12)$$

where  $j = 1, \dots, d$ , represents the first  $d$  components of the position vector  $\mathbf{c}^w(\xi)$ , and where  $w(\xi) = \sum_{k=1}^n w_k N_{k,p}(\xi)$  represents a weighting function. The projected function becomes rational when considering the projection height of the B-spline geometry, thus introducing weights  $w_i$  at each control point  $\mathbf{P}_i$  as form parameters to control the NURBS shape. It can be seen that (2.9) and (2.12) come to the same representation of the NURBS curve.

The influence of the weight on the geometry of a NURBS curve is shown in Figure 2.6(a), where the weight of control point  $\mathbf{P}_3$  is increased from  $w_3 = 0.2$  to  $w_3 = 1.0$  and further to  $w_3 = 5.0$ . The increasing weight has the potential to pull the curve towards the corresponding control point. The influence of the weight on the NURBS basis are shown in Figure 2.6(b) and (c).

### 2.1.4 Refinement of B-splines and NURBS

An interesting property of B-spline objects is that the refinement of the basis does not change the corresponding B-spline geometry and its parametrization. The three typical refinement methods of B-spline include: knot insertion, order elevation and the higher order and higher continuity preserving  $k$ -refinement. The refinement of a NURBS basis involves the refinement of the B-spline functions in the  $\mathbb{R}^{(d+1)}$  homogeneous space followed by projection to the  $\mathbb{R}^{(d)}$  rational space. In the following, the above mentioned three types of refinement techniques are introduced briefly and basic properties are discussed.

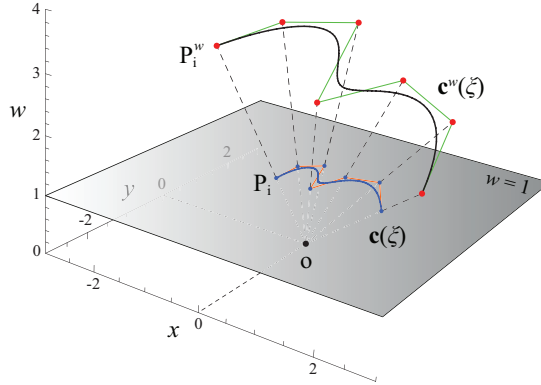


Figure 2.5: Projective transformation of homogeneous B-spline curve  $\mathbf{c}^w(\xi)$  in  $\mathbb{R}^{(d+1)}$  to the NURBS curve  $\mathbf{c}(\xi)$  in  $\mathbb{R}^d$ .

### Knot insertion

Knot insertion, as the name suggests, is a procedure adding one or more knots into the original knot vector  $\Xi$  (2.1) to generate a refined knot vector  $\bar{\Xi}$ . The refined B-spline basis is generated based on the new knot vector  $\bar{\Xi}$ . The new set of control points is a linear combination of the original set of control points, a detailed algorithm can be found in [135, 72].

An example of knot insertion of a B-spline curve is illustrated in Figure 2.7. Firstly, two knots  $\xi_i = 0.25, 0.75$  are inserted into the original knot vector  $\Xi = \{0, 0, 0, 0, 0.5, 1, 1, 1, 1\}$ , cf. Figure 2.7(b) and (e). In this case, the continuity of the basis at the inserted knots remains  $C^{p-1}$ , where  $p = 3$  is the order of the basis functions. Secondly, we repeat the previous step twice till the multiplicity of inserted knots is  $p$ , which reduces the continuity of the basis at the inserted positions to  $C^0$ -continuity. With the increase of multiplicity of inserted knots, the continuity of the basis at that knot drops. If the multiplicity of the knot is  $q$ , then the continuity is  $C^{p-q}$ . There are some similarities between knot insertion and  $h$ -refinement of the finite element method, however,  $h$ -refinement produces  $C^0$ -continuity across element boundaries, which is a special case of knot insertion.

### Order elevation

In contrast to knot insertion, another possibility to enrich the basis functions is to increase the order of the basis. The basic procedures of order elevation consist of three steps. One, the multiplicity of each interior knot is raised to the order of basis  $p$  which separates the original B-spline curve into segments of Bézier curves. Two, the order of each Bézier curve is elevated. Three, the multiplicity of the repeated interior knots is removed or reduced to keep the continuity across element boundaries

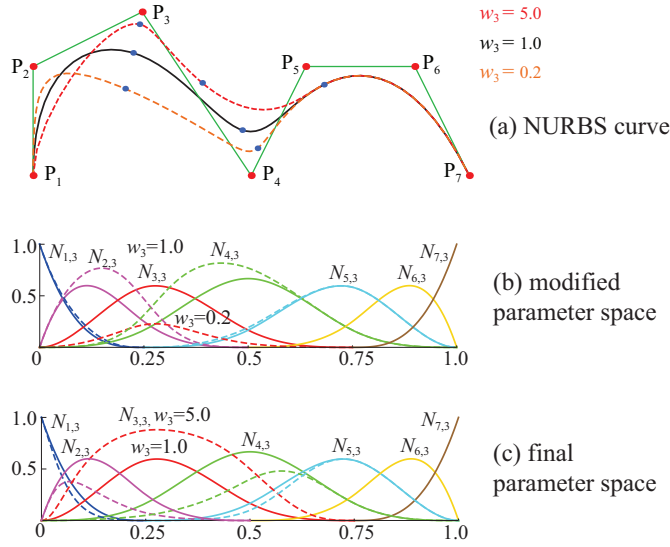


Figure 2.6: The influence of weight  $w_i$  on the geometry of a NURBS curve (a) and the corresponding NURBS basis functions  $w_3 = 0.2$  (b),  $w_3 = 5$  (c), where the original and new basis with weight  $w_3 \neq 1$  are shown with solid and dashed curves, respectively.

unchanged so that the final geometry is a unified and order-elevated single curve. The detailed algorithm of order elevation can be found in [135].

An example of order elevation is shown in Figure 2.8, where the original quadratic basis is elevated to cubic and the internal knot is repeated once to maintain the continuity of the basis. Order elevation is to some extent similar to  $p$ -refinement in the finite element method. The difference between the two schemes is the inter-element continuity of the initial state prior to refinement which is  $C^0$ -continuity for  $p$ -refinement and which is any continuity level smaller than  $p - 1$  for order elevation.

### **$k$ -refinement**

The combination of knot insertion and order elevation results in a unique higher order and higher continuity refinement technique, namely  $k$ -refinement. Usually, the order of the original coarse mesh is elevated to a higher degree, followed by knot insertion to create multiple knot elements. Here the multiplicity of each knot is set to one to keep the highest continuity, that is  $C^{p-1}$ , across element boundaries. One may also duplicate the inserted knots to lower the continuity of the basis at element interfaces where needed. Notice that each inserted knot will generate one more basis function. A simple example of  $k$ -refinement of the B-spline basis is shown in Figure 2.9.

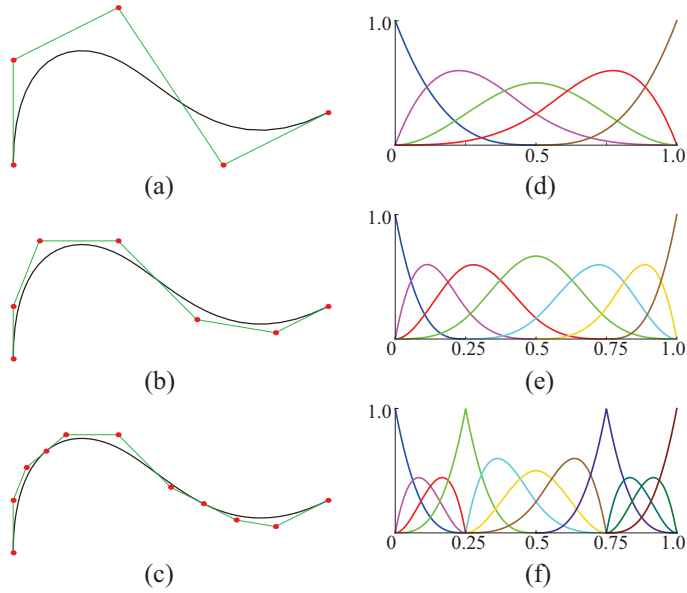


Figure 2.7: Knot insertion: (a) original geometry and its control polygon, (b)-(c) refined geometries and control polygons, (d) original basis with knot vector  $\Xi = \{0, 0, 0, 0, 0.5, 1, 1, 1, 1\}$ , (e)-(f) refined basis functions with knot vector  $\Xi = \{0, 0, 0, 0, 0.25, 0.5, 0.75, 1, 1, 1, 1\}$  and  $\Xi = \{0, 0, 0, 0, 0.25, 0.25, 0.25, 0.5, 0.75, 0.75, 0.75, 1, 1, 1, 1\}$ .

## 2.2 Isogeometric analysis - basic concept

In this section, a brief summary of fundamentals of continuum mechanics used in the following chapters is introduced, and the derived variational principles of elastostatics and isogeometric discretizations are discussed.

### 2.2.1 Fundamental aspects of continuum mechanics

A concise description of the essential ingredients of continuum mechanics is presented to provide the basic notations and formulations for the contents afterwards. Detailed descriptions of continuum mechanics can be found in [139, 140, 141, 142]. Following tradition, we use an upper case notation for quantities which refer to the undeformed reference configuration, and a lower case notation for quantities which refer to the current configuration of a body. The discussed content is restricted to the quasi-static state, therefore, the time variable  $t$  is used only to distinguish different states of configurations, corresponding inertia effects are neglected.

A *body* is identified as a set  $\mathcal{B}$  of connected material points  $\mathcal{M}$ , its boundary is

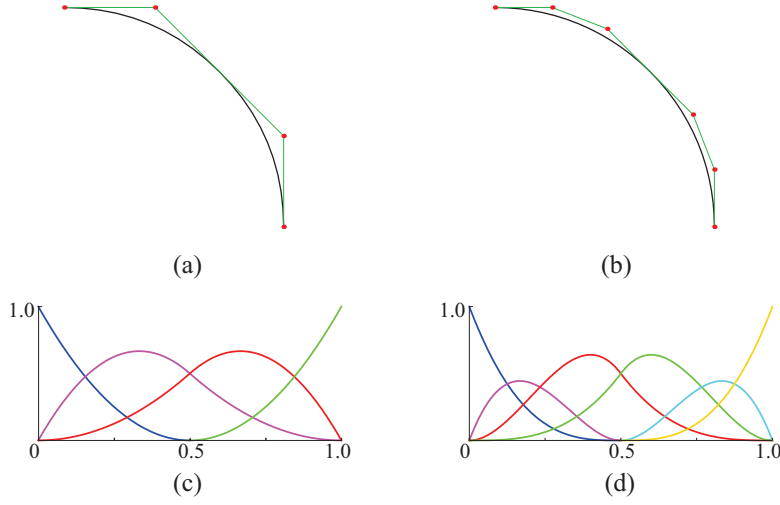


Figure 2.8: Order elevation: (a) original geometry and its control polygon, (b) the geometry and its control polygon after order elevation, (c) original basis with knot vector  $\Xi = \{0, 0, 0, 0.5, 1, 1, 1\}$ , (d) basis after order elevation with knot vector  $\Xi = \{0, 0, 0, 0, 0.5, 0.5, 1, 1, 1, 1\}$ .

denoted by  $\partial\mathcal{B}$ . Each material point  $\mathcal{M}$  occupies a position in the three-dimensional space  $\Omega \in \mathbb{R}^3$  at a given time  $t (t \in [t_0, \infty])$ , and can be identified by a location vector  $\mathbf{x} = x^i \mathbf{e}_i$  in the Cartesian coordinate with basis vectors  $\mathbf{e}_i, (i = 1, 2, 3)$  and corresponding coordinates  $x^i$ . The term *configuration* is used to denote the mapping of the body to the three-dimensional space:  $\chi : (\mathcal{B}, t) \rightarrow \Omega$ , cf. Figure 2.10. The current configuration of the body at time  $t \neq t_0$  follows the mapping  $\Phi : (\mathbf{X}, t) \rightarrow \mathbb{R}^3$  from its reference configuration for which the position vector  $\mathbf{x}$  is a function of  $\mathbf{X}$  and  $t$ :  $\mathbf{x} = \mathbf{x}(\mathbf{X}, t) = \Phi(\mathbf{X}, t)$ . The displacement of the body follows as:

$$\mathbf{u}(\mathbf{X}, t) = \mathbf{x} - \mathbf{X}. \quad (2.13)$$

For curved shell structures it is common to represent the material points of the body in a curvilinear coordinate system, cf. Figure 2.11. The following definitions refer to the deformed state of the body in the current configuration. Equivalently, the notation can be used to specify the undeformed state of the reference configuration. The covariant basis vectors are defined as the partial derivatives of the position vector  $\mathbf{x}$  with respect to the curvilinear coordinates  $\theta^i$ :

$$\mathbf{g}_i = \mathbf{x}_{,i} = \frac{\partial \mathbf{x}}{\partial \theta^i} \quad (2.14)$$

From the scalar product of the basis vectors follows the metric tensor coefficients:

$$g_{ij} = \mathbf{g}_i \cdot \mathbf{g}_j \quad (2.15)$$

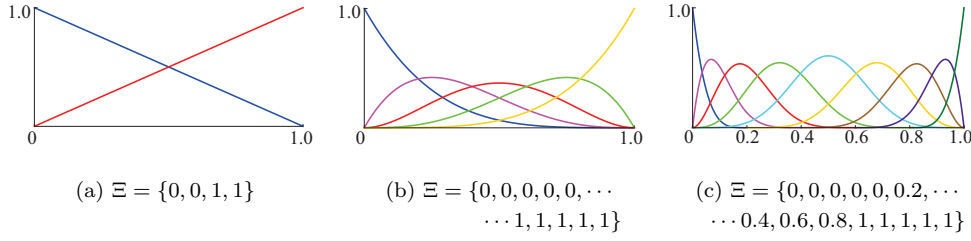


Figure 2.9: Illustration of  $k$ -refinement: (a) original linear basis, (b) B-spline basis of order  $p = 4$ , (c) knot insertion at  $\xi = 0.2, 0.4, 0.6, 0.8$ .

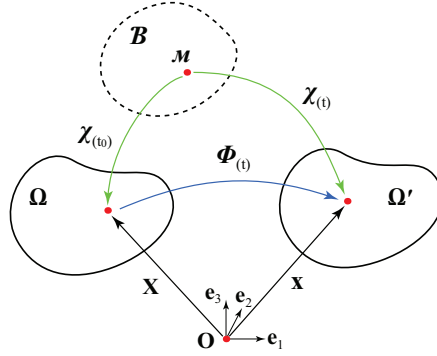


Figure 2.10: Mapping of material point  $\mathcal{B}$  to physical space  $\Omega$  and mapping  $\Phi$  from reference configuration  $\Omega$  to the current configuration  $\Omega'$ .

which include the information of the tangent space such as length of base vectors and angles between them. Correspondingly, the contravariant basis vectors  $\mathbf{g}^i$  span the dual space of the covariant space and can be calculated according to:

$$\mathbf{g}^i = \frac{\partial \theta^i}{\partial \mathbf{x}} \quad (2.16)$$

hence  $\mathbf{g}_i$  and  $\mathbf{g}^j$  are orthogonal base vectors with the relation  $\mathbf{g}_i \cdot \mathbf{g}^j = \delta_i^j$ , where  $\delta_i^j$  is the Kronecker delta. The construction of the contravariant metric tensor  $g^{ij}$  follows in analogy to  $g_{ij}$  with the relations:

$$[g^{ij}] = [g_{ij}]^{-1} \quad (2.17)$$

and

$$\mathbf{g}^i = g^{ij} \cdot \mathbf{g}_j \quad (2.18)$$

The deformation of the body can be represented as the change of the geometrical tangent spaces at each point, where the tangent space is specified in the covariant

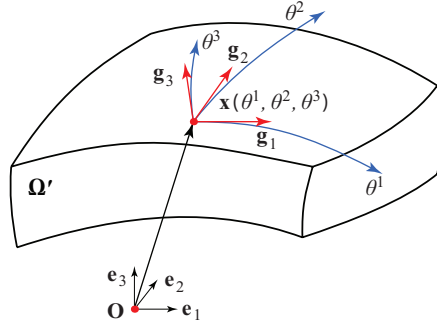


Figure 2.11: Curvilinear coordinate description of a three dimensional body.

basis. The deformation gradient  $\mathbf{F}$  defines the relation between the base vectors in the reference and current configurations:

$$\mathbf{F} = \mathbf{g}_i \otimes \mathbf{G}^j \quad (2.19)$$

The Green-Lagrange strain tensor is defined as:

$$\mathbf{E} = \frac{1}{2}(\mathbf{F}^T \cdot \mathbf{F} - \mathbf{I}) = E_{ij} \mathbf{G}^i \otimes \mathbf{G}^j \quad (2.20)$$

which includes rigid body motions, and where the tensor  $\mathbf{I}$  is the identity tensor, and where the components of strain tensor  $E_{ij}$  read:

$$\begin{aligned} E_{ij} &= \frac{1}{2}(\mathbf{u}_{,i} \cdot \mathbf{G}_j + \mathbf{u}_{,j} \cdot \mathbf{G}_i + \mathbf{u}_{,i} \cdot \mathbf{u}_{,j}) \\ &= \frac{1}{2}(\mathbf{g}_{ij} - \mathbf{G}_{ij}) \end{aligned} \quad (2.21)$$

which includes large strains in the definition. For small strains, the linearized expression of the strain tensor is furnished as [142]:

$$\begin{aligned} E_{ij} &= \frac{1}{2}(\mathbf{u}_{,i} \cdot \mathbf{G}_j + \mathbf{u}_{,j} \cdot \mathbf{G}_i) \\ &= \frac{1}{2}(\mathbf{g}_i \cdot \mathbf{G}_j + \mathbf{g}_j \cdot \mathbf{G}_i - \mathbf{G}_{ij}) \end{aligned} \quad (2.22)$$

The second Piola-Kirchhoff stress tensor  $\mathbf{S}$ , referring to the reference configuration, is the energy conjugate stress state to the Green-Lagrange state of strain:

$$\mathbf{S} = \frac{\partial \mathcal{W}_I}{\partial \mathbf{E}} = S^{ij} \mathbf{G}_i \otimes \mathbf{G}_j \quad (2.23)$$

where  $\mathcal{W}_I$  is the strain energy density of the body. The energetic conjugate pair relates each other linearly via the material tensor  $\mathbf{C}$  as:

$$\mathbf{S} = \mathbf{C} : \mathbf{E} \quad (2.24)$$

where  $\mathbf{C}$  is a fourth order tensor  $C^{ijkl}$ . The true physical stresses of the current configuration are obtained with the Cauchy stress tensor  $\boldsymbol{\sigma}$  which follows from the second Piola-Kirchhoff stress tensor as:

$$\boldsymbol{\sigma} = (\det \mathbf{F})^{-1} \cdot \mathbf{F} \cdot \mathbf{S} \cdot \mathbf{F}^T \quad (2.25)$$

## 2.2.2 NURBS-based isoparametric finite elements

The the balance equations governing linear elastostatics are expressed using (2.20) and (2.24):

$$\mathbf{0} = \operatorname{div}(\mathbf{F} \cdot \mathbf{S}) + \rho \mathbf{b} \quad (2.26)$$

The static equilibrium (2.26) neglects inertia effects and can be derived from the balance of linear momentum. The parameter  $\rho$  is the material density and the term  $(\rho \mathbf{b})$  represents the body force per unit volume. The formulation of the boundary value problem for linear elasticity is completed by including Dirichlet and Neumann boundary conditions:

$$\mathbf{u} = \mathbf{u}_0, \quad \mathbf{x} \in \Gamma_u \quad (2.27)$$

$$\mathbf{S} \cdot \mathbf{d} = \mathbf{t}_0, \quad \mathbf{x} \in \Gamma_t \quad (2.28)$$

where  $\Gamma = \Gamma_u \cup \Gamma_t$  and  $\Gamma_u \cap \Gamma_t = \emptyset$ , and where  $\mathbf{d}$  is the outward pointing unit normal vector along the force boundary  $\Gamma_t$  and where  $\mathbf{u}_0$  and  $\mathbf{t}_0$  are the prescribed displacement and traction, respectively.

Only in a few very simple cases it is possible to find an exact solution for the strong form of the boundary value problem ((2.26) - (2.28)). All other problems are commonly approximated numerically on the basis of a weak form following the principle of virtual work.

The principle of virtual work states that the work done by external and internal forces due to the arbitrary small virtual displacements  $\delta \mathbf{u}$  is zero if the system is in equilibrium [142]:

$$\mathcal{W}(\mathbf{u}, \delta \mathbf{u}) = \mathcal{W}_I(\mathbf{u}, \delta \mathbf{u}) + \mathcal{W}_E(\mathbf{u}, \delta \mathbf{u}) = \mathbf{0} \quad (2.29)$$

with the internal and external work integrals:

$$\mathcal{W}_I(\mathbf{u}, \delta \mathbf{u}) = - \int_{\Omega} \mathbf{S} : \delta \mathbf{E} \, d\Omega \quad (2.30)$$

$$\mathcal{W}_E(\mathbf{u}, \delta \mathbf{u}) = \int_{\Omega} \rho \mathbf{b} \cdot \delta \mathbf{u} \, d\Omega + \int_{\Gamma_t} \mathbf{t}_0 \cdot \delta \mathbf{u} \, d\Gamma \quad (2.31)$$

where  $\Omega$  denotes the analysis domain, where  $\delta \mathbf{u}$  and  $\delta \mathbf{E}$  denote the variation of displacements and strains, respectively. The vector  $\mathbf{t}_0$  denotes prescribed traction per unit area along the Neumann boundary  $\Gamma_t$ . Equation (2.29) is subjected to

the kinematic equation (2.20), the constitutive equations (2.24) and the Dirichlet boundary conditions (2.27).

Following the isoparametric concept of isogeometric analysis, the displacement field  $\mathbf{u}$  is interpolated using NURBS basis functions:

$$\mathbf{u} = \sum_i^n R_i \mathbf{U}_i \quad (2.32)$$

where  $\mathbf{U}_i$  denotes the unknowns in terms of control point displacements. Substitution of (2.32) into (2.29) and using (2.21) and (2.24), the discrete form of the principle of virtual work results in a set of algebraic equations representing the force equilibrium:

$$\mathbf{f}_I + \mathbf{f}_E = \mathbf{0} \quad (2.33)$$

where  $\mathbf{f}_I$  and  $\mathbf{f}_E$  are the internal and external force vector, respectively, which read:

$$\mathbf{f}_I = \frac{\partial \mathcal{W}_I}{\partial \mathbf{U}_r} \quad (2.34)$$

$$\mathbf{f}_E = \frac{\partial \mathcal{W}_E}{\partial \mathbf{U}_r} \quad (2.35)$$

Linearizing Eq. (2.34) at the reference configuration yields the governing algebraic equilibrium equations:

$$\mathbf{K} \mathbf{u} = \mathbf{f}_E \quad (2.36)$$

where  $\mathbf{K}$  is the linear stiffness matrix of the reference configuration:

$$\mathbf{K} = \int_{\Omega} \mathbf{B}^T \mathbf{C} \mathbf{B} \det(\mathbf{J}) d\xi \quad (2.37)$$

where  $\mathbf{B}$  is the strain-displacement interpolation matrix, and where  $\mathbf{J}$  denotes  $\mathbf{J} = dx_i/d\xi_j$  is the Jacobian representing two geometry mappings: one, a mapping between the physical space and the NURBS parameter space and two, a mapping between the parameter space and the normalized element space used for an element-wise numerical integration. The detailed integration scheme is illustrated in Figure 2.12, where the integration is performed on the normalized parent element. The local stiffness matrix and external load vector are computed within each knot span, i.e. element, using Gaussian quadrature and then are assembled into the global system.

## 2.3 The concept of trimming and finite cell method

Single-patch NURBS surfaces and solids are defined by a tensor product of one dimensional NURBS entities, cf. section 2.1, which limit their capability to represent

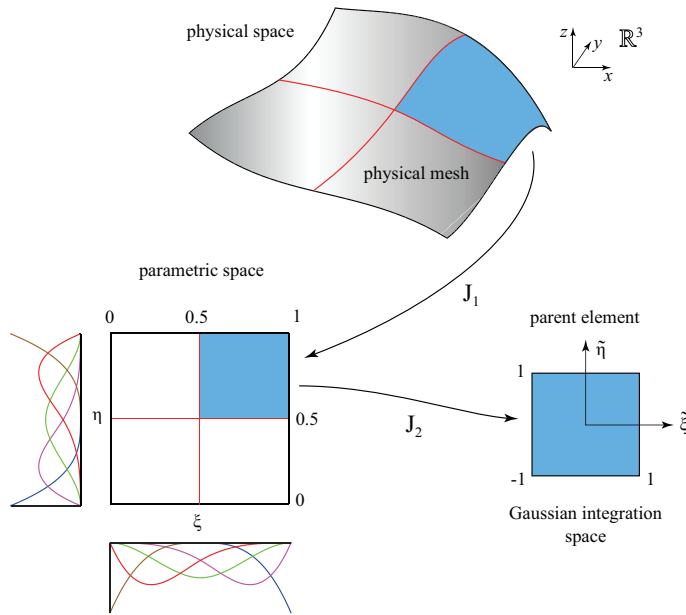


Figure 2.12: Schematic illustration of integration in isogeometric analysis.

topologically more complex geometries. Although certain shapes can be resolved by an assembly of multiple NURBS patches the additional modeling effort introduced to create seamless interfaces remains a limiting factor for an efficient modeling and analysis. In CAD-derived models the concept of trimming is usually applied to overcome these limitations. Trimming provides a simple mechanism to introduce arbitrary complexity to a single patch. The idea of trimming is to fade out subdomains in the visualization that are defined, in general, by a parametric trimming object, cf. Figure 2.13. For surface models as used for shell structures, NURBS curves which are defined on the NURBS-surface are suitable trimming objects commonly applied in CAD applications [143, 144]. It is apparent from Figure 2.13(b) that the parameter space of the shell defined by the NURBS tensor product remains untouched by the trimming object. For the visual representation of the trimmed geometry appropriate rendering techniques are applied to handle both, the shell patch and the trimming object [145] whereas for the physical approximation of the field variables in an isogeometric sense the knowledge about the trimmed subdomain is lost. A detailed review of various techniques developed to overcome the trimming problem can be found in chapter 1. In the following, a brief summary of the basic principles of the finite cell method used for the trimmed geometries is given. Very detailed reviews of the method can be found in [146, 147].

The basic principle of the finite cell method is depicted in Figure 2.14. The trimmed sub-domains typically are specified by a spline curve which is specified on the underlying NURBS patch, cf. Figure 2.14(a). In the context of the finite cell method the

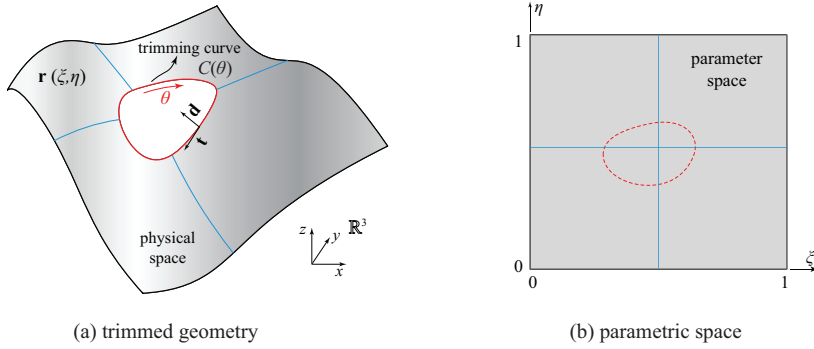


Figure 2.13: NURBS surface patch with trimming curve (a), corresponding parametric space (b).

trimmed area can be understood as a fictitious domain extending the true physical domain to an analysis suited NURBS structure, cf. Figure 2.14(b)-(c).

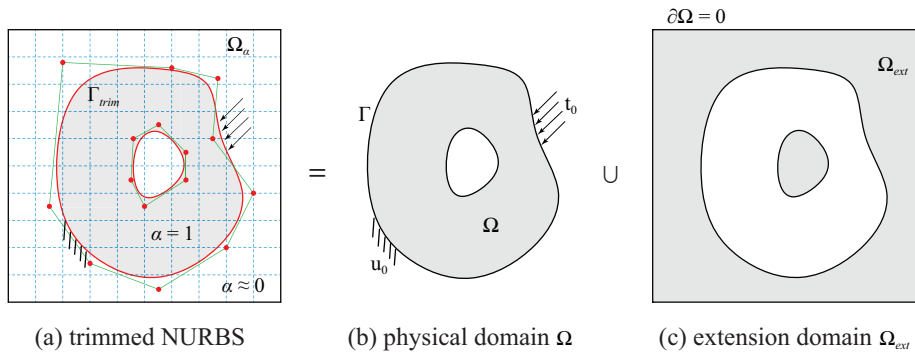


Figure 2.14: Principle of the finite cell method for trimmed domains: (a) trimmed, discretized NURBS structure, (b) true physical analysis domain with boundary conditions along the domain boundary  $\Gamma$ , (c) fictitious extension domain with zero Neumann boundary conditions  $\partial\Omega = 0$ .

The simulation domain  $\Omega_\alpha$  is discretized with high-order elements. The NURBS elements used in the context of isogeometric analysis provide the necessary high order approximation properties which ensure a sufficient quality of the analysis result. The influence of the fictitious domain on the total potential energy of the analysis model is mitigated by penalization of the stresses and forces in that area. The penalization of the stresses and forces in the fictitious domain is realized at the level of numerical integration by introducing a penalty function  $\alpha(\mathbf{x})$  which indicates where the integration points are located within  $\Omega_\alpha$ . The value of penalty factor  $\alpha$

varies at different locations:

$$\alpha(\mathbf{x}) = \begin{cases} 1.0 & \forall \mathbf{x} \in \Omega \\ 10^{-q} & \forall \mathbf{x} \in \Omega_{ext} \end{cases} \quad (2.38)$$

where  $\alpha$  should be as small as possible outside the true physical domain. Typically,  $\alpha$  can be chosen as exactly zero when the basis function is quadratic or cubic, for higher order basis, the value of  $\alpha$  is between  $10^{-8}$  to  $10^{-14}$  to ensure the conditioning of the stiffness matrix. Elements which are completely outside the physical domain  $\Omega$  are discarded from the model to account for sufficient numerical stability of the solution step.

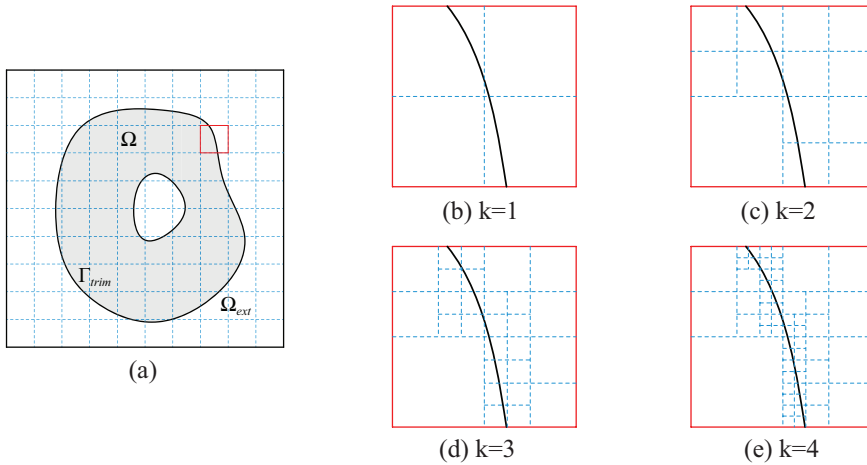


Figure 2.15: Adaptive quadrature based on recursive bisection: (a) original embedded domain, (b)-(e) generation of quadtree from level  $k = 1$  to  $k = 4$ .

In order to regain control over the true domain  $\Omega$ , adaptive Gaussian integration is used in elements which are cut by the boundary of the physical domain  $\Gamma$  or  $\Gamma_{trim}$ , respectively. The basic principle of the composed Gauss quadrature is illustrated in Figure 2.15 where the original finite cell mesh, shown in red and being cut by the domain boundary is sub-divided into sub-cells by recursive bisection, Figure 2.15 (b)-(c), up to a predefined granularity level  $k$ . The sub-cell approach corresponds to a cell-wise tree-based decomposition and results in a quadtree representation for plane problems. It is important to note that the approach does not change the original problem but remains restricted to the numerical integration and can be replaced cell-wise by any other quadrature method. A major advantage of the sub-cell approach is the uniqueness of the cell decomposition and its high qualification for shared memory parallelization [148, 149]. The integration of each sub-cell uses full Gaussian quadrature and includes  $(p+1) \times (q+1)$  integration points for a 2D problem. With increasing quadtree depth the integration effort also increases. Nevertheless, for plane problems the total effort remains reasonable for  $k = 4$  which has proven

sufficient accuracy for a large number of test examples. Other integration strategies include: a pre-computation scheme for voxel-based models which drastically reduces computational efforts [150], a tessellation-based integration for trimmed elements [151].

## Chapter 3

# Isogeometric methods for laminate composites<sup>1,2</sup>

Laminate composite plates and shells are widely used in aerospace and mechanical engineering due to their high strength-to-weight ratio. Traditional laminate composites are made of a stacking of fiber reinforced plies with different fiber angles stacked on top of each other. The discontinuity introduced with the jump in the material properties at the orthotropic ply level along with geometrical discontinuities are typical failure domains near laminate edges where singular stress fields may arise and initiate matrix cracks [152].

To date, various methods have been proposed for the analysis of composite laminates, see e.g. the classical references by CARRERA [153] or REDDY [154]. Depending on the displacement and/or stress expansions through the laminate thickness, two main categories of theories can be distinguished: the *equivalent-single-layer (ESL)* and the *layerwise (LW)* theories. The ESL models are computationally less demanding but often fail to capture the three-dimensional state of stress accurately at ply level, while LW models provide a 3D theory equivalent state of stress at higher computational costs.

In this chapter, we focus on through-the-thickness modeling of laminated composites in the framework of higher order and higher continuity NURBS. The superiority of the isogeometric paradigm with regard to the modeling of laminate composites is demonstrated with several numerical examples including beams and shells. In particular, we exploit the unique  $k$ -refinement capabilities of isogeometric analysis to reveal the method's potential for models based on the proposed layerwise theory.

---

<sup>1</sup>This chapter is based on the paper “Y. Guo, A.P. Nagy, Z. Gürdal, A layerwise theory for laminated composites in the framework of isogeometric analysis, *Composite Structures*, 107, 447-457, 2014”

<sup>2</sup>This chapter is based on the paper “Y. Guo, M. Ruess, A layerwise isogeometric approach for NURBS-derived laminate composite shells, *Composite Structures*, 124, 300-309, 2015”

We use a reduced geometric shell description based on a mid-surface NURBS and a thickness function and combine our approach with the fictitious domain idea followed in [122] to overcome the challenge of trimmed NURBS domains.

This chapter is built up as follows. The details of isogeometric equivalent-single-layer methods are given in section 3.1, the layerwise methods for beams and shells are presented in section 3.2 and corresponding examples are shown in section 3.3. The stresses along trimmed free edges using the finite cell approach are studied and discussed in section 3.4. Finally, conclusions are given in section 3.5.

### 3.1 Equivalent-single-layer methods

Equivalent-single-layer methods can be classified into classical shell formulations and homogenization-based approaches. Classical shell formulations reduce a three-dimensional continuum problem to a two-dimensional one by expanding the displacement field as a linear combination of predefined or known functions of the thickness coordinate and integrating the constitutive law through the thickness either analytically or numerically [142]. Such methods include among others the classical lamination theory (CLT), first order shear deformation theory (FSDT)[155, 156] and higher order shear deformation theory (HSDT)[157, 158]. Alternatively, stiffness properties may be homogenized through the thickness of the laminate without reducing the geometric dimension of the problem. Although ESL theories may be adequate for describing the behavior of thin composite shells, they typically fail to capture accurately the complete three-dimensional stress state at the ply level in moderately thick, and thick laminates. This deficiency is primarily associated with the fact that transverse strain components are incorrectly assumed to be continuous across the interface of dissimilar materials, which entails non-physical local discontinuity of the transverse stresses. In this chapter, the used equivalent-single-layer

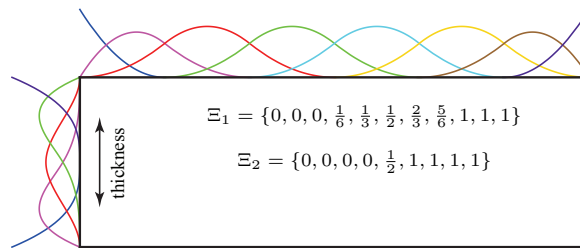


Figure 3.1: ESL discretisation using  $k$ -refinement along the width and through the thickness direction.

model is constructed by invoking standard material homogenization methods. The stiffness of the laminate is computed as the weighted average of the individual ply

stiffnesses. Hence, the homogenized stiffness tensor is calculated as:

$$\mathbf{C} = \frac{1}{t} \sum_{k=1}^n \mathbf{C}_k t_k \quad (3.1)$$

where  $t$ ,  $t_k$ , and  $n$  denote the thickness of the laminate, the thickness of the  $k$ th layer, and the number of layers in the laminate. The isogeometric discretisation of all ESL models are constructed using  $k$ -refinement in both parametric directions. An example is depicted in Figure 3.1 where quadratic and cubic basis functions, i.e.  $p_1 = 2$  and  $p_2 = 3$ , are used along the width and in the through the thickness direction, respectively. Note that  $k$ -refinement preserves inter-element continuity of the initial basis functions.

## 3.2 Layerwise methods

In contrast to ESL theories, displacement-based layerwise techniques assume separate displacement field expansions within each layer. Following equilibrium considerations, the transverse displacement component is defined to be  $C^0$ -continuous at ply interfaces and thereby yield a more accurate description of the complete stress state. For layerwise methods based on mixed formulations, which include both in the variational formulation, displacements and stresses, the  $C^0$ -continuity of transverse stresses at layer interfaces should also be enforced [159, 160, 161]. In most displacement-based layerwise models [162, 163, 164, 165, 166, 167, 168, 169],  $C^0$ -continuity of the displacement field across layer interfaces is imposed through constructing elaborate displacement functions or through adding constraint equations at layer interfaces. For instance, in reference [166] each layer is modeled as an independent plate, then the compatibility of displacement components at layer interfaces are imposed through the use of Legendre polynomials. Alternatively, one-dimensional through the thickness Lagrangian finite elements are used to approximate the three displacement components which automatically enforces  $C^0$ -continuity conditions at layer interfaces, see e.g. [170, 171, 172]. The latter approach results in a continuous in-plane and discontinuous transverse strain field, allowing for the possibility of continuous transverse stresses at the layer interfaces. Furthermore, compared to conventional 3-D finite element models, the layerwise model is computationally more efficient while retaining the same modeling capabilities [171].

The key idea of layerwise methods is to split and separately expand the displacement field within each layer. The general formulation in two dimensions can be written as:

$$\mathbf{u}_k(x_1, x_2) = \sum_i \mathbf{f}_{ki}(x_1) \mathbf{g}_{ki}(x_2) \quad (3.2)$$

where  $\mathbf{u}_k$  is the displacement field in the  $k$ th layer,  $x_i$ , with  $i = 1, 2$ , the spatial coordinates, and the symbols  $\mathbf{f}_{ki}$  and  $\mathbf{g}_{ki}$  refer to the  $i$ th part of the in-plane and out-of-plane displacement field expansions, respectively. Note, depending on the kinematic

assumption, if any, and the number and type of the individual functions per ply, equation (3.2) includes a myriad of theories [173]. The rationale behind separating the displacement field and distinguishing the functions aimed at representing the in-plane and out-of-plane components is physically motivated. That is, due to the balance of linear momentum and continuity of the traction field in multilayered composite materials, the function describing the transverse displacement field should be  $C^0$ -continuous at the interface between plies of different fibre angle orientation. The tensor product formulation of bivariate rational functions provides us with a natural way to formulate an isogeometric layerwise theory, cf. Figure 3.2. Put simply, one may easily construct an appropriate basis for the analysis of multilayered composite parts by adjusting the continuity properties along knots which represent ply interfaces in the physical space. The construction of an adequate basis can be described as follows. Considering the in-plane direction, the use of (univariate) basis functions with higher-order inter-element continuity, i.e.  $C^k$  with  $k \geq 1$ , is desirable as it yields smooth gradient operators and hence stresses. In contrast, invoking (univariate) basis functions with  $C^0$ -continuity at the interface of adjacent plies in the out-of-plane direction is required to ensure continuity of transverse, i.e. through the thickness stresses, which can be enforced via knot repetition at ply interfaces, cf. chapter 2. To improve the quality of the physical approximation, however, one may further wish to enrich the basis using an arbitrary refinement technique ply-wise. In Figure 3.2 the basis functions within  $(m + 1)$ th layer are enriched with one more knot insertion compared to the  $(m)$ th layer.

The refinement of the in-plane basis is typically performed through  $k$ -refinement to preserve the continuity properties of the initial basis used to encapsulate the geometry at the coarsest level. Depending on the geometry of the structure, higher-order continuity of the in-plane basis may not be fulfilled across the entire domain. Finally,

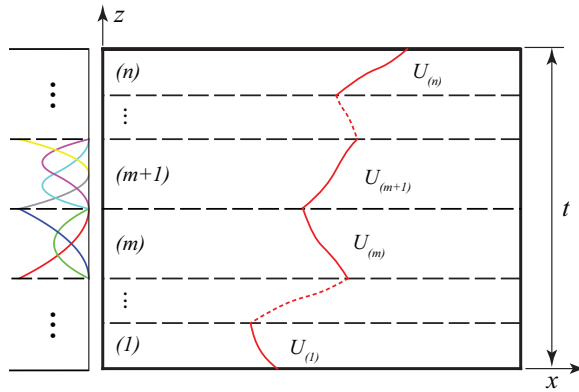


Figure 3.2: Isogeometric layerwise kinematics.

a few things are worth highlighting. First, the proposed model is in the absence of any kinematical assumptions on the layer interfaces. Second, the  $C^0$ -continuity con-

dition can be naturally facilitated by applying the  $h$ - and  $p$ -refinement schemes in the correct sequence. Third, strictly speaking in the proposed isogeometric layerwise model the displacement field is *not* formally split as shown in equation (3.2), rather the local continuity properties of employed bivariate basis are adjusted.

### 3.2.1 Layerwise shell model

In the following we provide a shell formulation based on the layerwise concept. We will repeatedly refer to shells considering plates as a flat special case of the presented shell theory. The layerwise shell model exploits the capabilities of NURBS to represent smooth curvature and further profits from a geometric model description which refers to a NURBS mid-surface plane and a thickness information thus the model supports a simple model transfer from NURBS-based CAD modelers [143, 144] into the isogeometric analysis framework. The CAD models are typically boundary representations which do not provide parametric descriptions of the interior of volumetric geometries [131]. We therefore use the geometry reduced description for layerwise shells. The number of degrees of freedom and the computational effort for the solution of the equilibrium equations does not differ from standard solid continuum formulations. We adopt the lower case and upper case notation of chapter 2 to distinguish between the deformed and undeformed configuration of the shell body, respectively.

The position vector  $\mathbf{x}$  of each material point in the three-dimensional shell body, cf. Figure 3.3, is described uniquely by the position vector of the corresponding point  $\mathbf{r}$  and of the normal vector  $\mathbf{a}_3$  on the mid-surface:

$$\mathbf{x}(\xi_1, \xi_2, \xi_3) = \mathbf{r}(\xi_1, \xi_2) + \xi_3 t \cdot \mathbf{a}_3(\xi_1, \xi_2) \quad (3.3)$$

where  $\xi_1, \xi_2, \xi_3$  are the curvilinear parameter coordinates and where  $t$  denotes the thickness of the laminate shell which is considered to be constant throughout the body. It is convenient to introduce locally a covariant basis to describe the kinematics of the shell body. The corresponding base vectors are defined as the partial derivatives of the position vector  $\mathbf{x}$  with respect to the curvilinear coordinates  $\xi_1, \xi_2, \xi_3$ :

$$\mathbf{g}_\alpha = \mathbf{x}_{,\alpha} = \mathbf{a}_\alpha + \xi_3 t \cdot \mathbf{a}_{3,\alpha} \quad \alpha = 1, 2 \quad (3.4)$$

$$\mathbf{g}_3 = t \cdot \mathbf{a}_3 \quad (3.5)$$

where  $(\cdot)_{,\alpha}$  represents the partial derivatives with respect to the curvilinear coordinate  $\xi_\alpha$  and where  $\mathbf{a}_\alpha$  are the covariant base vectors defined on the mid-surface:

$$\mathbf{a}_\alpha = \frac{\partial \mathbf{r}}{\partial \xi_\alpha} = \mathbf{r}_{,\alpha} \quad (3.6)$$

The normal vector of the mid-surface is defined as:

$$\mathbf{a}_3 = \frac{\mathbf{a}_1 \times \mathbf{a}_2}{|\mathbf{a}_1 \times \mathbf{a}_2|} \quad (3.7)$$

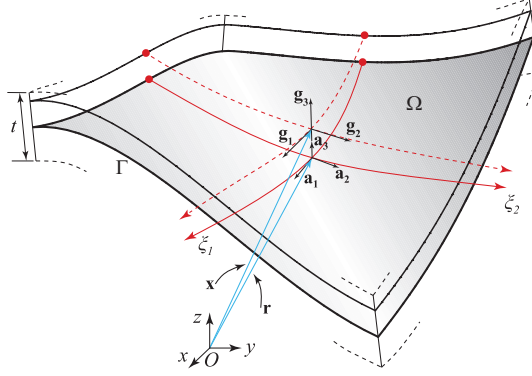


Figure 3.3: Shell geometry description.

The derivatives of normal vector  $\mathbf{a}_3$  with respect to  $\xi_\alpha$  follows:

$$\mathbf{a}_{3,\alpha} = \frac{\hat{\mathbf{a}}_{3,\alpha} \cdot \bar{a}_3 - \hat{\mathbf{a}}_3 \cdot \bar{a}_{3,\alpha}}{\bar{a}_3^2} \quad (3.8)$$

where  $\hat{\mathbf{a}}_3 = \mathbf{a}_1 \times \mathbf{a}_2$ ,  $\hat{\mathbf{a}}_{3,\alpha} = \mathbf{a}_{1,\alpha} \times \mathbf{a}_2 + \mathbf{a}_1 \times \mathbf{a}_{2,\alpha}$ ,  $\bar{a}_3 = |\mathbf{a}_1 \times \mathbf{a}_2|$  and

$$\bar{a}_{3,\alpha} = \frac{\hat{\mathbf{a}}_3 \cdot \hat{\mathbf{a}}_{3,\alpha}}{\bar{a}_3} \quad (3.9)$$

The description of the differential geometry is further facilitated by the introduction of a contravariant basis. The relations between covariant and contravariant basis can be found in chapter 2.

The three-dimensional strain tensor of the solid-like layerwise shell is expressed as:

$$\mathbf{E} = E_{ij} \mathbf{G}^i \otimes \mathbf{G}^j \quad (3.10)$$

Assuming small strains, the strain tensor coefficients  $E_{ij}$  are:

$$E_{ij} = \frac{1}{2}(\mathbf{u}_{,i} \cdot \mathbf{G}_j + \mathbf{u}_{,j} \cdot \mathbf{G}_i) \quad (3.11)$$

Stresses and strains are related by the constitutive relation

$$\mathbf{S} = \mathbf{C} : \mathbf{E} \quad (3.12)$$

with the fourth order elasticity tensor  $\mathbf{C}$ . The orthotropic material properties of the fiber reinforced layers are defined in a local Cartesian coordinate system which is specified by the basis vectors  $\bar{\mathbf{e}}_i (i = 1, 2, 3)$ , where one coordinate axis is aligned with the fiber direction. The corresponding elasticity tensor is denoted by  $\bar{\mathbf{C}}$ . The layerwise changing fiber angles between  $-90^\circ$  to  $90^\circ$  require a transformation of  $\bar{\mathbf{C}}$  into the local Cartesian reference coordinate system defined by the basis vectors  $\mathbf{e}_i (i = 1, 2, 3)$  in which the material properties of all layers are defined. The strain

tensor coefficients  $E_{ij}$  (3.11) are then transformed into the local coordinate system with:

$$E_{kl} = E_{ij}(\mathbf{e}_k \cdot \mathbf{G}^i)(\mathbf{G}^j \cdot \mathbf{e}_l) \quad (3.13)$$

followed by substitution into the stress strain relation, see e.g. [154].

### 3.2.2 Layerwise shell discretization

Confining our discussion to linear elasticity and neglecting the influence of body forces, the principle of virtual work can be stated as:

$$\mathbf{0} = \int_{\Omega} \mathbf{S} : \delta \mathbf{E} d\Omega - \int_{\Gamma_t} \mathbf{t}_0 \cdot \delta \mathbf{u} d\Gamma \quad (3.14)$$

$$u_i = u_{i0} \quad \forall \mathbf{x} \in \Gamma_u \quad \text{and } \Gamma = \Gamma_u \cup \Gamma_t$$

where  $\mathbf{t}_0$  is the vector of prescribed tractions on the part  $\Gamma_t$  of the boundary  $\Gamma$ , where  $u_{i0}$  denotes prescribed displacement coordinates on  $\Gamma_u$  and where  $\delta$  denotes the variation of the corresponding quantities. Following the basic concept of the layerwise theory the displacement field  $\mathbf{u}$  is discretized through the thickness with a layerwise  $C^{p-1}$ -continuous function depending on  $\xi_3$ :

$$\mathbf{u}(\xi_1, \xi_2, \xi_3) = \sum_{i=1}^m \mathbf{U}_i(\xi_1, \xi_2) N_i(\xi_3) \quad (3.15)$$

where  $\mathbf{U}_i(\xi_1, \xi_2)$  represents the displacement field at discrete points through the thickness, and where  $N_i(\xi_3)$  is a corresponding B-spline function. The in-plane displacement field at the  $i^{th}$  plane is approximated according to:

$$\mathbf{U}_i(\xi_1, \xi_2) = \sum_{j=1}^n \mathbf{U}_{ij} R_j(\xi_1, \xi_2) \quad (3.16)$$

in which,  $R_j(\xi_1, \xi_2)$  is the two dimensional NURBS basis functions, and where  $\mathbf{U}_{ij}$  denotes the introduced degrees of freedom at each control point. Similar approach was found in [174].

Using (3.11) and (3.15)-(3.16) a discrete form of the strain tensor is found with separate interpolation rules for the in-plane strain components  $E_{\alpha\beta}$ , the out-of-plane shear strain component  $E_{\alpha 3}$  and the out-of-plane normal strain component  $E_{33}$ :

$$E_{\alpha\beta} = \sum_{i=1}^m \frac{1}{2} \left( \mathbf{g}_\beta \cdot \mathbf{U}_{i,\alpha}(\xi_1, \xi_2) N_i(\xi_3) + \mathbf{g}_\alpha \cdot \mathbf{U}_{i,\beta}(\xi_1, \xi_2) N_i(\xi_3) \right) \quad (3.17a)$$

$$E_{\alpha 3} = \sum_{i=1}^m \frac{1}{2} \left( \mathbf{g}_3 \cdot \mathbf{U}_{i,\alpha}(\xi_1, \xi_2) N_i(\xi_3) + \mathbf{g}_\alpha \cdot \mathbf{U}_i(\xi_1, \xi_2) N_{i,3}(\xi_3) \right) \quad (3.17b)$$

$$E_{33} = \sum_{i=1}^m \mathbf{g}_3 \cdot \mathbf{U}_i(\xi_1, \xi_2) N_{i,3}(\xi_3) \quad (3.17c)$$

The above strain tensor coordinates are defined in the local contravariant basis and should be transformed to the local Cartesian reference basis using equation (3.13).

### 3.3 Through-the-thickness modeling

In the following we demonstrate the performance of the proposed layerwise approach for through-the-thickness modeling with regard to accuracy and convergence properties. To this end we consider benchmark problems from literature which provide an analytical reference solution. The selected examples include a laminate composite plate and laminate composite shell structures. In the numerical examples given in this chapter, we use  $\sigma_{ij}$  to represent the stresses of laminates considering that Cauchy stress is equal to the second Piola-Kirchhoff stress in Cartesian coordinates.

#### 3.3.1 Cylindrical bending of laminates

In this example, cylindrical bending of two simply supported cross-ply laminates with  $[0^\circ/90^\circ]$  and  $[0^\circ/90^\circ/0^\circ]$  stacking sequence is considered. The plates are subjected to a transverse sinusoidal load  $q(x) = q_0 \sin(\pi x/w)$  as shown in Figure 3.4. Each layer in the laminate is of equal thickness.

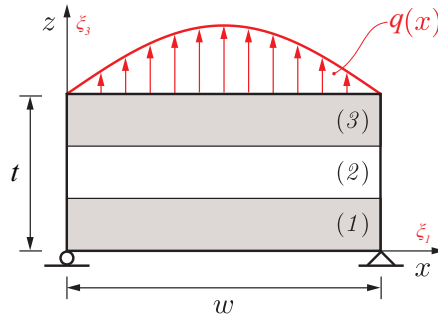


Figure 3.4: Geometry, boundary conditions, and loading of the  $[0^\circ/90^\circ/0^\circ]$  benchmark laminate ( $s = 2$ ).

The plies are orthotropic with the following material properties:

$$\begin{aligned} E_1 &= 2.5 \times 10^7 \text{ psi}, & G_{13} &= 5.0 \times 10^5 \text{ psi}, \\ E_3 &= 1.0 \times 10^6 \text{ psi}, & G_{23} &= 2.0 \times 10^5 \text{ psi}, \\ \nu_{13} &= \nu_{23} = 0.25. \end{aligned}$$

The elasticity solution of the problem is given in PAGANO [42]. In this example the exact solution is compared to the layerwise finite element model of ROBBINS

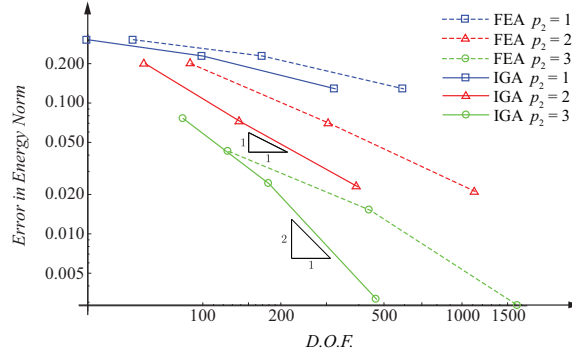


Figure 3.5: Convergence of the error in the energy norm with respect to the 3-D exact solution for the  $[0^\circ/90^\circ]$  laminate.

AND REDDY [170] and compared to the isogeometric layerwise approach proposed in this work. The aim is to verify the current model and to assess the accuracy and efficiency of the competing numerical methods. The comparison is based on normalized quantities. According to the adhered notation these normalized quantities are distinguished with an over-bar notation, i.e:

$$\bar{\sigma}_{11}(z) = \frac{\sigma_{11}(w/2, z)}{q_0}, \quad \bar{\sigma}_{33}(z) = \frac{\sigma_{33}(w/2, z)}{q_0}, \quad (3.18)$$

$$\bar{\sigma}_{13}(z) = \frac{\sigma_{13}(0, z)}{q_0}, \quad \bar{u}_3(t/2) = \frac{100E_3 t^3 u_3(w/2, t/2)}{q_0 w^4}, \quad (3.19)$$

$$\bar{z} = z/t, \quad (3.20)$$

where  $\sigma_{11}$ ,  $\sigma_{33}$ ,  $\sigma_{13}$ , and  $u_3$  are the in-plane normal, inter-laminar normal and shear stress components, and the transverse displacement, respectively. The symbols  $w$  and  $t$  denote the width and thickness of the laminate as shown in Figure 3.4, which defines the aspect ratio of the plate, i.e.  $S = w/t$ . Since the primary focus of this sub-section is on thick laminates, the aspect ratio was set to  $S = 2$  in the example. In all the presented cases, quadratic basis functions were used along the width of the plate, i.e.  $p_1 = 2$ . Considering Lagrange polynomials and spline-based models, different mesh densities and degree of the basis functions were employed to analyse the response. To this end, the degree of the basis function in the thickness direction was set to  $p_2 = 1, 2, 3$ . Preserving the unit element aspect ratio, different mesh densities were obtained by setting the number of elements through the thickness of a single layer as  $n_l = 1, 2, 4$ . As a result, nine distinct cases were considered for each stacking sequence.

In comparison to traditional FEA-based layerwise models, the proposed isogeometric layerwise model proved to be more efficient when considering the number of basis functions. It was found that the isogeometric model outperformed its Lagrange

polynomial-based counterpart on a per-degree-of-freedom basis. This is clearly demonstrated in the error plots presented in Figures 3.5 and 3.6 which showed the convergence of the energy and the stress infinity norms, respectively. The normalized through-the-thickness stress distributions of the different laminates was illustrated in Figures 3.7 and 3.8. The solutions of isogeometric and Lagrange polynomial-based layerwise models showed excellent agreements with the exact solution. One may observe that, unlike the Lagrange polynomial-based layerwise model, the isogeometric model resulted in continuous stress distributions within each layer, however, stress discontinuities were recorded at the physical layer boundaries using both approaches. This defect can be explained by the fact that no explicit constraints were set on the interlaminar stress distribution. We emphasize that this is merely an approximation error and its severity will be gradually reduced when refining the mesh in the thickness direction.

### 3.3.2 Laminate composite square plate

Using the example of a simply supported cross-ply laminate plate we tested the performance of the isogeometric layerwise model in terms of accuracy of the complete three-dimensional stress state. The square plate has a stacking sequence of  $[0^\circ/90^\circ/0^\circ]$  and is subjected to an sinusoidal pressure on the top surface. A 3D elasticity solution provided by PAGANO [43] was used as a reference solution. The geometric properties of the plate are depicted in Figure 3.9, in which,  $S = L/t = W/t = 4$ .

The sinusoidal surface load was computed as:

$$q = q_0 \sin\left(\frac{\pi x}{L}\right) \sin\left(\frac{\pi y}{W}\right) \quad (3.21)$$

Each ply is of equal thickness ( $t/3$ ) and the material properties of the laminate plate are:

$$\begin{aligned} E_1 &= 2.5 \times 10^7 \text{psi}, & G_{12} &= G_{13} = 5.0 \times 10^5 \text{psi}, \\ E_2 &= E_3 = 1.0 \times 10^6 \text{psi}, & G_{23} &= 2.0 \times 10^5 \text{psi}, \\ \nu_{12} &= \nu_{13} = \nu_{23} = 0.25. \end{aligned}$$

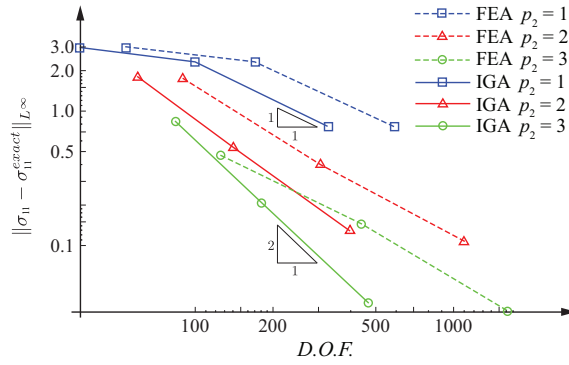
The following normalized reference values were taken from [170]:

$$\bar{\sigma}_{11} = \frac{\sigma_{11}(a, a, z)}{q_0 S^2}, \quad \bar{\sigma}_{33} = \frac{\sigma_{33}(a, a, z)}{q_0}, \quad (3.22)$$

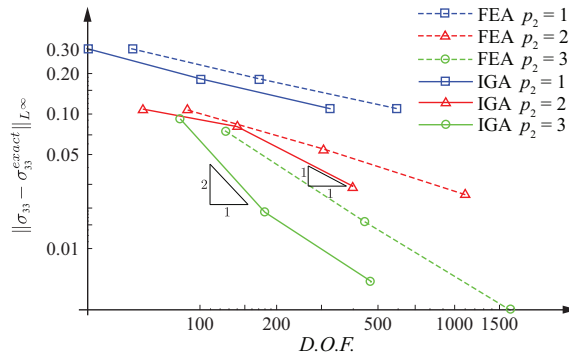
$$\bar{\sigma}_{13} = \frac{\sigma_{13}(b, a, z)}{q_0 S}, \quad \bar{\sigma}_{23} = \frac{\sigma_{23}(a, b, z)}{q_0 S}, \quad (3.23)$$

$$a = 1.105662(L/2), \quad b = 1.894338(L/2). \quad (3.24)$$

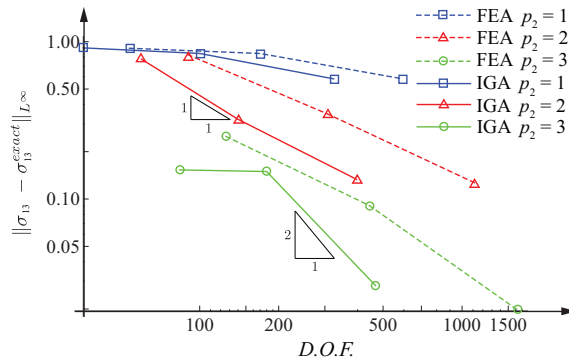
Unlike the quarter model used in ROBBINS' paper [170], we modeled the complete



(a)



(b)



(c)

Figure 3.6: Maximum error in the in-plane normal stress  $\bar{\sigma}_{11}$ , transverse normal stress  $\bar{\sigma}_{33}$  and transverse shear stress  $\bar{\sigma}_{13}$  with respect to the 3-D exact solution in the  $[0^\circ/90^\circ]$  laminate.

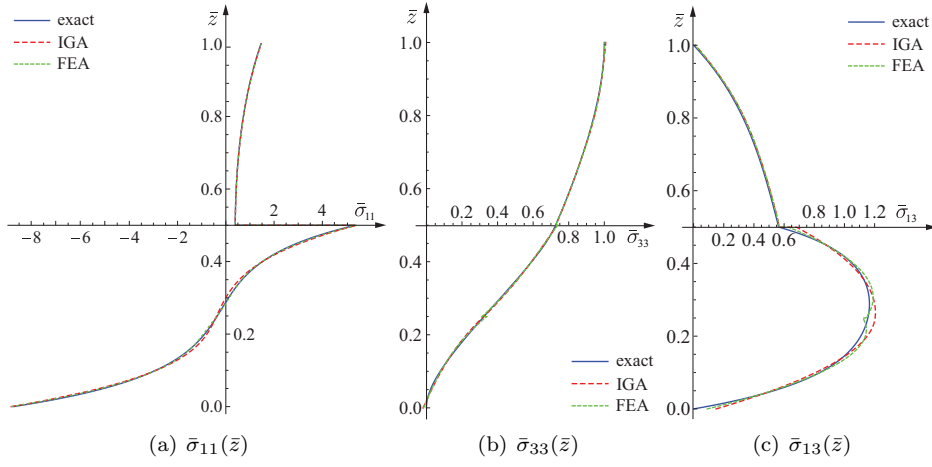


Figure 3.7: Normalized stress distributions through the thickness of the  $[0^\circ/90^\circ]$  laminate ( $n_l = 2, p_2 = 3$ ).

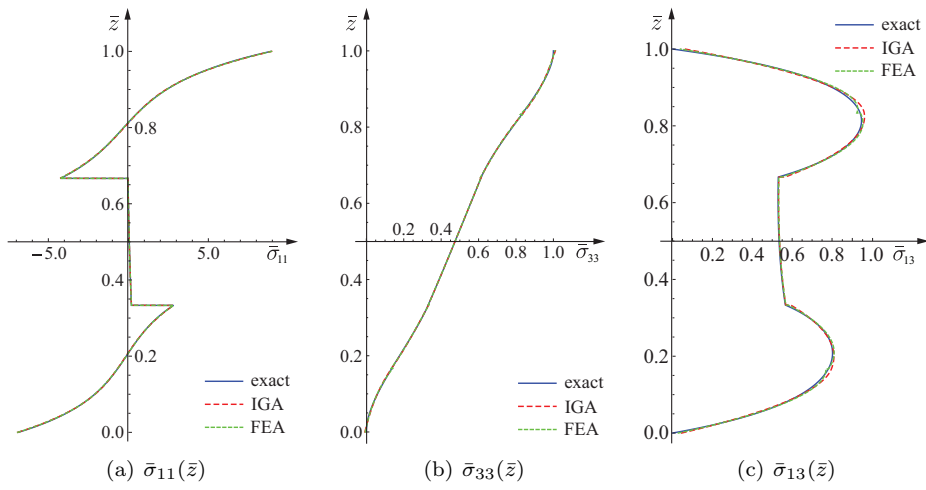


Figure 3.8: Normalized stress distributions through the thickness of the  $[0^\circ/90^\circ/0^\circ]$  laminate ( $n_l = 2, p_2 = 3$ ).

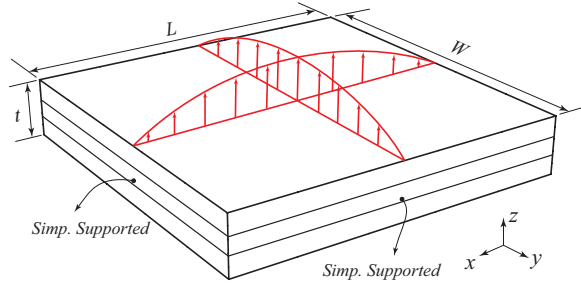


Figure 3.9: Layerwise square plate model.

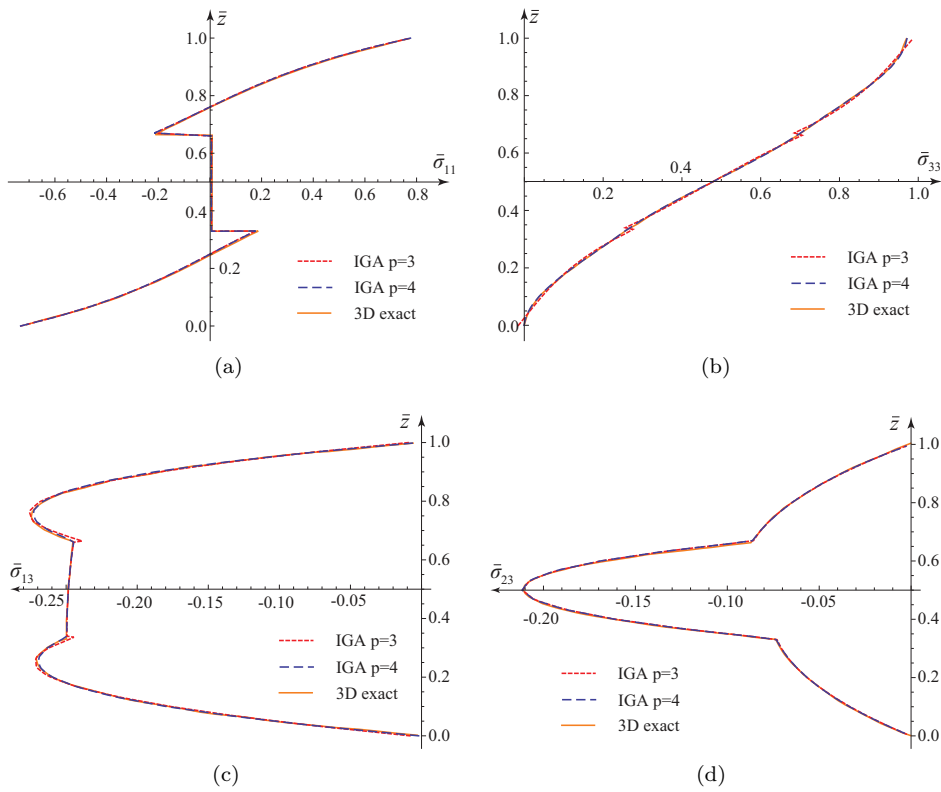

 Figure 3.10: Through thickness stresses comparison,  $[0^\circ/90^\circ/0^\circ]$  square plate: (a) in-plane normal stress  $\bar{\sigma}_{11}$ , (b) transverse normal stress  $\bar{\sigma}_{33}$ , (c) transverse shear stress  $\bar{\sigma}_{13}$ , (d) transverse shear stress  $\bar{\sigma}_{23}$ .

plate with a coarse mesh of  $4 \times 4 \times 3$  elements which resulted in a through-the-thickness discretization with one element per layer. In Figure 3.10 we show the normalized stresses for polynomial degrees  $p = 3$  and  $p = 4$  in comparison with

the solution of PAGANO [43] based on (3.18)-(3.23). Already for  $p = 3$  the results virtually coincided with the exact solution and showed only an insignificant deviation for the transverse normal stresses  $\sigma_{33}$  at the free boundary and the ply interfaces and for the transverse shear stresses  $\sigma_{13}$  at the ply interface and the position of the maximum stress value. For a polynomial degree  $p = 4$  any non-physical jumps were completely removed showing a highest level of smoothness. In the previous example, it was shown that a similar accuracy can be obtained by discretization with more elements through the thickness of the plate at the price of a higher numerical effort.

### 3.3.3 Laminate cylindrical shell

Using the example of an isogeometric layerwise shell model with varying thickness we demonstrated the range of validity and accuracy of our approach for curved NURBS structures. We compared our results with existing analytical reference solutions found in VARADAN AND BHASKAR [175].

A simply supported cross-ply laminate cylindrical shell subjected to an internal sinusoidal pressure loading was considered. The geometry properties of the shell and the applied boundary conditions are depicted in Figure 3.11, in which,  $L/R = 4$ ,  $R/t = S$ ,  $\theta = \pi/2$ . Here  $R$  is the mid-surface radius of the cylindrical shell. Due to symmetry properties, only a quarter of the cylindrical shell was modeled. Two

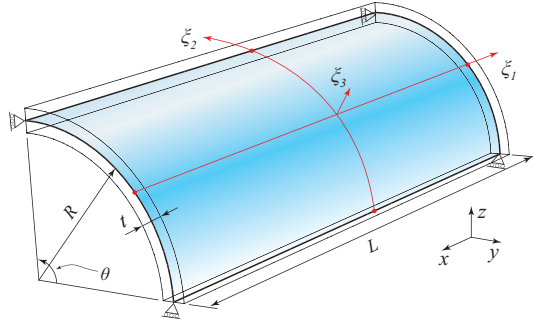


Figure 3.11: Cylindrical shell model.

different stacking sequences for the laminate shell were taken into consideration, a  $[0^\circ/90^\circ]$  and a  $[0^\circ/90^\circ/0^\circ]$  ply stacking. Each laminate layer is of equal thickness and has the same material properties as 3D plate in section 3.3.2.

The sinusoidal internal pressure load is described as:

$$q = -q_0 \sin\left(\frac{\pi x}{L}\right) \cos(4\theta) \quad (3.25)$$

where  $q_0$  is a positive constant load per unit area.

The exact three-dimensional solution of VARADAN AND BHASKAR [175] was used to verify the method's potential in terms of accuracy and efficiency for shell models with the following normalized quantities:

$$(\bar{\sigma}_{\alpha\alpha}) = \frac{10 \times (\sigma_{\alpha\alpha})(L/2, \pi/4, \bar{z})}{q_0 S^2}, \quad \bar{\sigma}_{12} = \frac{10 \times \sigma_{12}(0, \pi/8, \bar{z})}{q_0 S^2}, \quad (3.26)$$

$$\bar{\sigma}_{\alpha 3} = \frac{10 \times \sigma_{\alpha 3}(0, \pi/4, \bar{z})}{q_0 S}, \quad \bar{\sigma}_{33} = \frac{\sigma_{33}(L/2, \pi/4, \bar{z})}{q_0}, \quad (3.27)$$

$$\bar{u}_3 = \frac{10 \times E_1 u_3(L/2, \pi/4, 0)}{q_0 R S^3}, \quad \bar{z} = \frac{z}{t}, \quad (3.28)$$

where  $\sigma_{ij}(x, \theta, z)$  denotes the corresponding unscaled stress tensor coordinates of the computation.

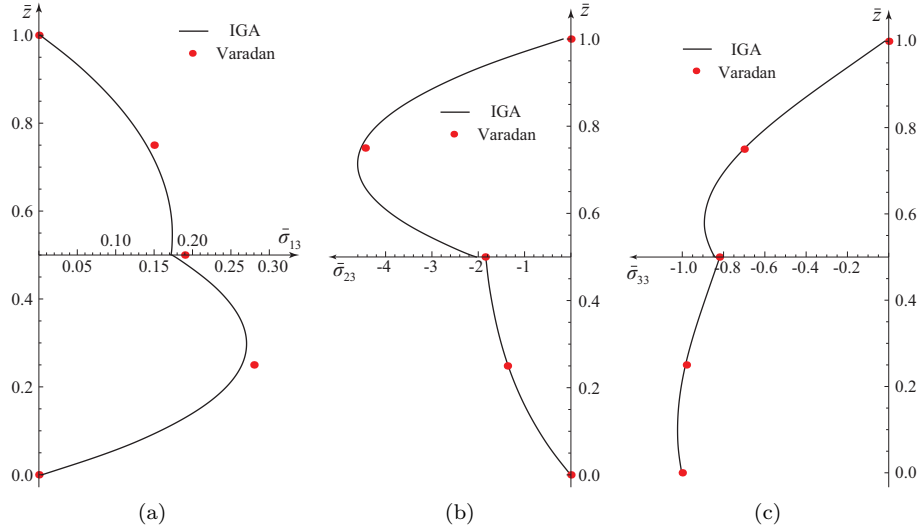


Figure 3.12: Through thickness transverse stresses comparison of  $[0^\circ/90^\circ]$  cylindrical shell: (a) transverse shear stress  $\bar{\sigma}_{13}$ , (b) transverse shear stress  $\bar{\sigma}_{23}$ , (c) transverse normal stress  $\bar{\sigma}_{33}$ .

We show the analysis results through the shell thickness for  $[0^\circ/90^\circ]$  and  $[90^\circ/0^\circ/90^\circ]$  ply stacking sequences, respectively, in Figures 3.12 and 3.13. With a radius-to-thickness ratio of  $S = 4$  we considered a relatively thick shell model. A discretization of  $16 \times 16 \times 2$  elements for the two layer model and  $16 \times 16 \times 3$  elements for the three layers model, respectively, was chosen at a polynomial degree  $p = 4$ , isotropic. Both models, the  $[0^\circ/90^\circ]$  and the  $[90^\circ/0^\circ/90^\circ]$  configuration, were in good agreement with the reference solutions for the transverse shear and normal stresses. The  $\sigma_{13}$  component behaved slightly weaker for the  $[0^\circ/90^\circ]$  model than the reference solution

while still reproducing reliably the characteristic stress distribution through the layer thickness.

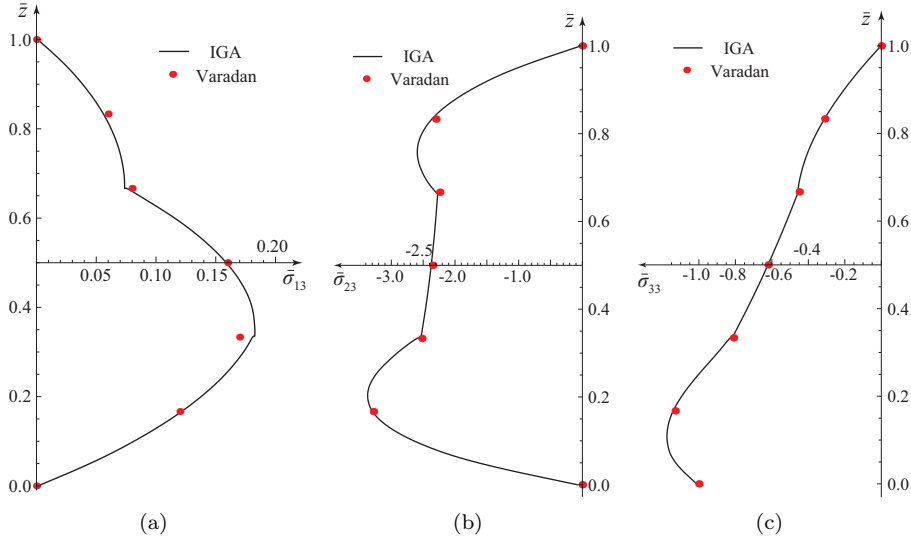


Figure 3.13: Through thickness transverse stresses comparison of  $[90^\circ/0^\circ/90^\circ]$  cylindrical shell: (a) transverse shear stress  $\bar{\sigma}_{13}$ , (b) transverse shear stress  $\bar{\sigma}_{23}$ , (c) transverse normal stress  $\bar{\sigma}_{33}$ .

Next, we studied the effect of a varying radius-to-thickness ratio  $S$  on the transverse normal stresses for both, the  $[0^\circ/90^\circ]$  and the  $[90^\circ/0^\circ/90^\circ]$  models. The ratio  $S$  was increased from  $S = 4$  (thick shell) to  $S = 50$  (moderately thick shell). The stress plots are shown in Figure 3.14. For the configurations  $S = 4, 10$  the numerically predicted stresses fully coincided with the available analytical solutions. With increasing radius-to-thickness ratio  $S$ , both transverse normal stress components increased at the layer interfaces with an influence on the location of the maximum transverse normal stress component.

A baseline study of the deflection and stress components for the  $[0^\circ/90^\circ]$  model, the  $[90^\circ/0^\circ/90^\circ]$  model and a ten layer  $[90^\circ/0^\circ/90^\circ/0^\circ/90^\circ]_s$  laminate model for various radius-to-thickness ratios is provided in tables 3.1 - 3.3. The ten-layer shell was discretized with  $16 \times 8 \times 10$  elements with a polynomial degree  $p = 3$  in all three directions. We collated the results with the 3D analytical solution from [175] and found an overall good agreement. An equally distributed average relative deviation of 2 – 4% from the reference solution was observed for all radius-to-thickness ratios  $S$  of the three laminate composite models.

For thick and moderately thick laminate composite models the presented isogeometric layerwise approach clearly outperformed equivalent-single-layer methods as expected, at the price of a larger model size. In [156] high-order Lagrange elements

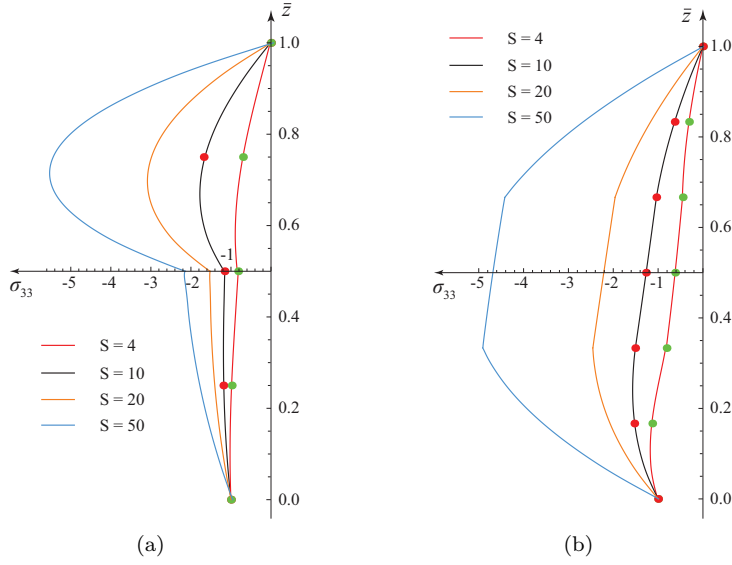


Figure 3.14: Cylindrical shell - influence of a varying radius-to-thickness ratio  $S$  on the transverse normal stresses: (a)  $[0^\circ/90^\circ]$  model, (b)  $[90^\circ/0^\circ/90^\circ]$  model.

based on a first and third order shear deformation theory were tested against the reference solution and were used here with a relative deviation of 10 – 30% and higher for small radius-to-thickness values  $S < 20$ .

Despite the higher number of degrees of freedom for the layerwise approach the isogeometric framework provided a much better trade off compared to a classical finite element-based layerwise approach due to the many shared basis functions among the patch elements and the continuity preserving high-order approximation capabilities. In particular, the overlapping support of the spline functions in combination with the continuity properties allowed a significant reduction of the numerical integration effort at patch level as reported in [176].

Table 3.1: Displacement and stress comparison for a  $[0^\circ/90^\circ]$  cylindrical shell model

S		$\bar{u}_3$	$\bar{\sigma}_{11}$ ( $z = \frac{t}{2}$ )	$\bar{\sigma}_{22}$ ( $z = \frac{t}{2}$ )	$\bar{\sigma}_{12}$ ( $z = -\frac{t}{2}$ )	$\bar{\sigma}_{13}$ ( $z = -\frac{t}{4}$ )	$\bar{\sigma}_{23}$ ( $z = \frac{t}{4}$ )	$\bar{\sigma}_{33}$ ( $z = \frac{t}{4}$ )
2	IGA	14.346	0.2650	9.925	-0.5231	0.4734	-3.146	-0.32
	Ref.[175]	14.034	0.2511	9.775	-0.5016	0.4786	-2.931	-0.31
4	IGA	6.085	0.2150	10.29	-0.3021	0.2642	-4.531	-0.70
	Ref.[175]	6.100	0.2120	10.31	-0.2812	0.2758	-4.440	-0.70
10	IGA	3.238	0.2004	10.46	-0.2517	0.1468	-5.363	-1.65
	Ref.[175]	3.330	0.1930	10.59	-0.2325	0.1591	-5.457	-1.68

In a second example we changed the length of the shell from  $L/R = 4$  to  $L/R = 2$  as proposed in a reference analysis provided in [156]. We use this example to

Table 3.2: Displacement and stress comparison for a  $[90^\circ/0^\circ/90^\circ]$  shell model.

S		$\bar{u}_3$	$\bar{\sigma}_{11}$ ( $z = -\frac{t}{2}$ )	$\bar{\sigma}_{22}$ ( $z = -\frac{t}{2}$ )	$\bar{\sigma}_{12}$ ( $z = -\frac{t}{2}$ )	$\bar{\sigma}_{13}$ ( $z = -\frac{t}{6}$ )	$\bar{\sigma}_{23}$ ( $z = 0$ )	$\bar{\sigma}_{33}$ ( $z = 0$ )
2	IGA	10.48	-0.8590	-18.81	-0.2968	0.3144	-1.443	-0.36
	Ref.[175]	10.11	-0.8428	-18.19	-0.2922	0.3006	-1.379	-0.34
4	IGA	4.046	-0.2700	-9.391	-0.1694	0.1816	-2.373	-0.62
	Ref.[175]	4.009	-0.2701	-9.323	-0.1609	0.1736	-2.349	-0.62
10	IGA	1.221	-0.0771	-5.204	-0.0799	0.0866	-3.257	-1.27
	Ref.[175]	1.223	-0.0791	-5.224	-0.0729	0.0826	-3.264	-1.27

Table 3.3: Displacement and stress comparison for a  $[90^\circ/0^\circ/90^\circ/0^\circ/90^\circ]_s$  shell model

S		$\bar{u}_3$	$\bar{\sigma}_{11}$ ( $z = \frac{t}{2}$ )	$\bar{\sigma}_{22}$ ( $z = \frac{t}{2}$ )	$\bar{\sigma}_{12}$ ( $z = -\frac{t}{2}$ )	$\bar{\sigma}_{13}$ ( $z = 0$ )	$\bar{\sigma}_{23}$ ( $z = 0$ )	$\bar{\sigma}_{33}$ ( $z = 0$ )
2	IGA	11.84	0.1767	7.243	-0.3415	0.3109	-2.715	-0.43
	Ref.[175]	11.44	0.1691	7.202	-0.3363	0.3019	-2.608	-0.42
4	IGA	4.246	0.1258	6.529	-0.1708	0.2120	-3.173	-0.72
	Ref.[175]	4.206	0.1243	6.635	-0.1652	0.2117	-3.154	-0.71
10	IGA	1.374	0.0873	5.714	-0.0917	0.1047	-3.434	-1.32
	Ref.[175]	1.380	0.0877	5.875	-0.0869	0.1084	-3.479	-1.32

demonstrate that the proposed layerwise approach retains the aforementioned error level for higher radius-to-thickness ratios. The reference solution is based on a third-order shear deformation theory (TSDT) [156] which has been proven to have a very high correlation with analytical results for high radius-to-thickness values  $S$ . A  $[0^\circ/90^\circ]$  stacking sequence was used, the shell boundaries were simply supported and the shell was subjected to the following two types of loads: a uniform and a sinusoidal inner pressure load:

$$q = q_0 \quad (3.29)$$

$$q = q_0 \sin\left(\frac{\pi x}{L}\right) \sin(2\theta) \quad (3.30)$$

Following [156] we report the results as dimensionless quantities:

$$\bar{\sigma}_{ij} = \frac{10 \times \sigma_{ij}(0, 0, z)}{q_0 S^2} \quad (3.31)$$

The layerwise results and REDDY'S TSDT results [156] are compared in table 3.4, in which UP and SP abbreviate the uniform pressure load and the sinusoidal pressure load, respectively. The comparison confirms the results shown in tables 3.1 to 3.3 for thick and moderately thick shell models with an overall average relative error of 2%.

Table 3.4: Displacement and stresses comparison for simply supported  $[0^\circ/90^\circ]$  shell under uniform and sinusoidal pressure load

S	load	$\bar{u}_3$	$\bar{u}_3[156]$	$\bar{\sigma}_{11}$	$\bar{\sigma}_{11}[156]$
20	UP	3.02684797	3.09815750	0.423040	0.421970
	SP	2.07509133	2.12361760	0.056647	0.050227
50	UP	0.33677661	0.33826747	0.499850	0.500950
	SP	0.34820978	0.35165462	0.378360	0.381070
100	UP	-0.02637450	-0.02976034	0.099092	0.099164
	SP	0.08762443	0.08812624	0.249930	0.250990

S	load	$\bar{\sigma}_{22}$	$\bar{\sigma}_{22}[156]$	$\bar{\sigma}_{12}$	$\bar{\sigma}_{12}[156]$
20	UP	1.79370	1.86990	1.50200	1.53390
	SP	2.46630	2.54050	0.70477	0.72257
50	UP	-0.96642	-0.97074	0.71776	0.72642
	SP	0.65139	0.66125	0.27005	0.27258
100	UP	-1.20170	-1.22470	0.44982	0.45458
	SP	0.25976	0.26264	0.13156	0.13212

### 3.4 Trimmed geometries - free edge stress analysis

The existence of free edge effects is mainly due to the presence of geometrical or material discontinuities at layer interfaces near laminate edges where three dimensional and singular stress fields may arise [152]. These stresses, especially interlaminar shear and normal stresses may produce material failures such as matrix cracks near free edges. The straight free edge problems have been studied by a number of researchers using various methods [177, 178, 179, 180, 181, 170, 53], while fewer studies have been done on curved free edges due to their complexities. The variations of stresses and displacements in straight free edge problems can sometimes be viewed as a two-dimensional problem, while for curved free edges, it is a full three-dimensional problem and more difficult to deal with [182]. An analytical method has been developed by KO ET AL. [183] to calculate the interlaminar stresses around a circular hole of a thin laminate. HU AND SOUTIS [184] use a three-dimensional finite element model to evaluate the accuracy of KO's analytical model. It was found that the analytical model predicts poor transverse stresses around the hole while the FE models are more accurate and could be applied to thicker laminates. Particularly, IARVE [185] proposes a method for the analysis of laminates with open holes, in which, spline functions are used to approximate the displacement and interlaminar tractions, independently. Following that, a method of superposition of a hybrid and displacement approximation has been developed by IARVE AND PAGANO [186] in which the displacement is approximated with B-spline functions. The results show that the proposed method predicts accurate stress fields in the vicinity of hole edge and ply interfaces of laminated composites.

In this section, an example is used to study the free edge effect of a laminate composite structure with a hole under in-plane tension and to test the proposed iso-

geometric layerwise approach for trimmed structures. The fictitious domain extension described in chapter 2 was used to handle the trimmed domain. The geometry of the plate and the applied boundary conditions are shown in Figure 3.15. Symmetry properties were used to reduce the model size. The stacking sequence

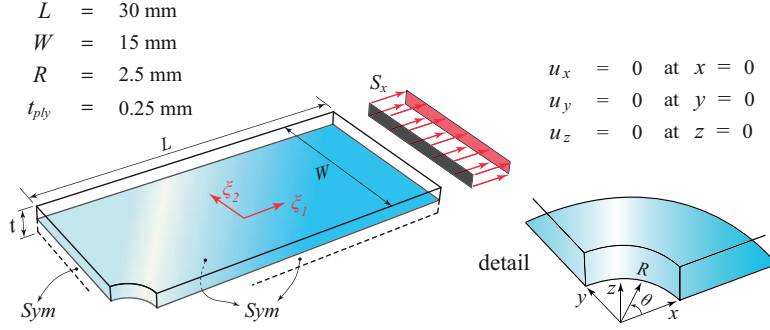


Figure 3.15: Geometry and boundary conditions of the plate with hole under in-plane tension.

of the plate is  $[90^\circ/0^\circ]_s$  with the following material properties:  $E_1 = 138 \text{ GPa}$ ,  $E_2 = E_3 = 14.5 \text{ GPa}$ ,  $G_{12} = G_{23} = G_{13} = 5.86 \text{ GPa}$ ,  $\nu_{12} = \nu_{23} = \nu_{13} = 0.21$ . All stress quantities were normalized with respect to the applied traction load  $S_x$ :

$$\bar{\sigma}_x = \frac{\sigma_x}{S_x}, \quad \bar{\sigma}_z = \frac{\sigma_z}{S_x}, \quad \bar{\sigma}_{xz} = \frac{\sigma_{xz}}{S_x}. \quad (3.32)$$

We compared the proposed layerwise model with a fully three-dimensional ABAQUS [187] finite element solution. For the layerwise IGA model we used  $42 \times 38$  elements in the plane and discretized each layer with one and two elements, respectively. The ABAQUS reference model was discretized with 20-node quadratic brick elements ( $C3D20R$ ). The complete applied model data is provided in table 3.5.

Table 3.5: Model data: ABAQUS reference model and IGA-layerwise model.

model	no elements	$(p_x, p_y, p_z)$ -degree	no degrees of freedom
ABAQUS	42240	2, 2, 2	544611
IGA-LW-2	3192	3, 3, 3	38745
IGA-LW-4	6384	3, 3, 3	49815

We show a comparison of the in-plane normal stress  $\sigma_x$  at the  $0^\circ$  and  $90^\circ$  layer interfaces of the two models around the circular hole in Figure 3.16. For both layers, the  $0^\circ$  layer and the  $90^\circ$  layer, we observed excellent agreement of the two models' results at significantly reduced computational effort for the IGA-LW-2 model due to a smaller model size which was more than one order of magnitude smaller in terms of degrees of freedom.

We show a comparison of the transverse normal stress  $\sigma_z$  along the circular hole for a varying thickness of the two analysis models in Figure 3.17(left). Due to the used composed integration for the fictitious domain approach we tapped the stresses at a distance of  $(r - R)/R = 0.001$  around the circular hole to prevent any influence of the piecewise linear approximated hole boundary. The comparison revealed the range of validity of the used model theory and corresponding discretization. The applied model configurations showed a reliable response for thick and moderately thick layers, while for a decreasing layer thickness the solution oscillates for both models. Higher oscillations were observed for the IGA model which can be attributed to the significantly smaller model size and the higher polynomial degree. For sufficiently thick layers both model results were in overall good agreement showing a smooth stress curve.

The transverse shear stress  $\sigma_{xz}$  for a layer thickness  $t_{ply} = 0.25$  is shown to the right of Figure 3.17, this is virtually identical with the highly refined reference FE solution. For the transverse shear stresses we used the IGA-LW-4 model with four cubic elements through the thickness. Even for the more refined IGA-LW-4 model the total number of degrees of freedom was almost one order of magnitude less than for the FE reference model. It is also worth noting that the model refinement, in particular the doubling of elements through the thickness, resulted only in a moderate increase ( $< 30\%$ ) of degrees of freedom which is attributed to the inherent overlapping support of NURBS basis functions.

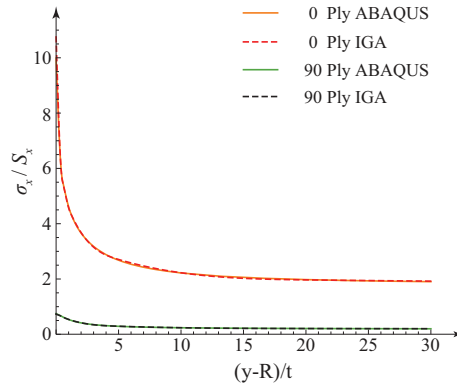


Figure 3.16: In-plane stress distribution around the circular hole.

### 3.5 Summary

A displacement-based isogeometric equivalent single layer method and layerwise method were introduced. The introduced approaches followed closely the isogeometric paradigm which uses the CAD-derived NURBS model as a mathematical

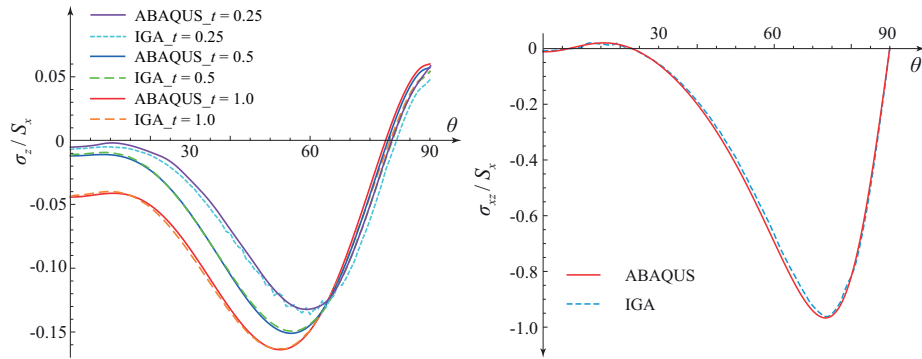


Figure 3.17: Out-of-plane normal stress  $\sigma_z$  (left) and transverse shear stress  $\sigma_{xz}$  (right) at the  $0^\circ/90^\circ$  layer interface along the circular hole at  $(r - R)/R = 0.001$ .

basis for the approximation of the physical model in an isoparametric sense. Our approach was completely based on the mid-surface NURBS description of the shell body thus supporting the direct application of the surface-defined CAD representation of shells. We used  $k$ -refined B-splines to interpolate the displacement field through the ply thickness of the laminate composite which exhibits  $C^0$ -continuity at the ply interface to account for a jump in the material properties and to ensure the balance of linear momentum and continuity of the traction field. Trimmed NURBS geometries which are common in CAD-derived models were tackled using the finite cell method, a fictitious domain extension of the analysis model that fades out the influence of the strain energy in the trimmed region and that ensures the numerical performance known for untrimmed structures.

We demonstrated the reliability, accuracy and numerical efficiency of the proposed method with various examples: for a cross-ply laminates under cylindrical bending and a thick laminate plate example we demonstrated the high-order capabilities of our layerwise isogeometric approach which showed superior agreement with the analytical reference solution. It was found that the introduced isogeometric layerwise approach outperformed the traditional Lagrange polynomial-based counterparts on a per degree of freedom basis. Similar results were found for the prediction of the through-the-thickness stress components of a cylindrical shell with varying stacking and thickness properties. We provided a baseline study for varying radius-to-thickness ratios using the isogeometric layerwise approach and collated the analysis results with a 3D analytical solution showing good agreement. Finally, we compared our fictitious domain extended layerwise IGA method with a classical finite element model to reveal the efficiency of the method in terms of solution quality and numerical effort. A similar solution quality was observed for an IGA model size of almost one order of magnitude less degrees of freedom.

The examples discussed in this chapter showed that the proposed method is very well suited to predict accurately the three-dimensional stress state in NURBS-based shell models. Furthermore, using the proposed fictitious domain extension, higher

geometric complexity can be easily tackled without the need for sub-structuring or re-parametrization, while still providing the highest level of numerical solution quality.



## Chapter 4

# Multi-lamina-model analysis with delaminations: strong coupling and linear buckling<sup>1,2</sup>

The equivalent-single-layer method and layerwise method in the framework of isogeometric analysis were introduced in the previous chapter. It is interesting to note that equivalent-single-layer and layerwise theories may be successfully cast into a unified framework making them more practical to use, see e.g. [173, 188]. The non-evident choice between various ESL and LW models is primarily driven by the geometry of the structure, the material properties, or even the stacking sequence of the laminate. Equivalent-single-layer models tend to require less modeling effort from the designer and in most cases offer reduced computational times. These benefits come at the expense of incomplete or even inaccurate results. In contrast, layerwise models provide more accuracy and are computationally more intense. Consequently, combining these two types of models should allow us to solve structural problems using a reasonable amount of computational resources at a reduced cost. This method is often denoted *multiple model* or *multi-model analysis* [154], and it is a general case of the commonly used *simultaneous global-local strategy* [189]. Here *global* refers to the entire structure modeled using an ESL theory except for a set of critical subdomains described by a layerwise model.

---

<sup>1</sup>This chapter is based on the paper “Y. Guo, A.P. Nagy, Z. Gürdal, A layerwise theory for laminated composites in the framework of isogeometric analysis, *Composite Structures*, 107, 447-457, 2014”

<sup>2</sup>This chapter is based on the paper “Y. Guo, M. Ruess, Z. Gürdal, A contact extended isogeometric layerwise approach for the buckling analysis of delaminated composites, *Composite Structures*, 116, 55-66, 2014”

In multi-model analysis, the main difficulty often lies in the coupling of incompatible meshes and/or different mathematical models, i.e. to maintain the kinematic compatibility and continuity of traction at the boundaries of adjacent regions. In order to address this difficulty, WHITCOMB and WOO [190, 191] have developed an iterative method to establish the force equilibrium conditions at global-local boundaries. In some other works, multipoint constraints [192] or transition elements [193] are used to connect different mathematical models. REDDY ET AL. [194, 189] proposed a more robust global-local analysis method which allows to invoke locally the desired displacement components in specified sub-domains. Their *variable displacement field method* enforces only continuity of the displacements among the different regions.

Delamination in composite laminates is a common defect either pre-existing or generated during service by impact, fatigue etc. The presence of delamination may cause an obvious reduction of the load carrying capacity of a laminate. For example, due to the local instability in the vicinity of a delamination, the laminate may buckle at a level of compressive loads well below the design value for the undelaminated composite structure.

Depending on the design phase of a structure and related design rules, linear and nonlinear buckling analyses are distinguished and applied. Linear analyses, as discussed in the course of this chapter, are based on the solution of a partial generalized eigenvalue problem to reveal the critical buckling mode and associated buckling load [195]. In general, the analysis results in a conservative yet often sufficiently accurate estimate of the true buckling state for a pre-design at reasonable computational cost. Nonlinear analyses allow us to trace the complete load-displacement history of stability problems [196, 65, 66, 67, 197]. Sophisticated algorithms and modeling strategies allow a much more refined analysis of the buckling phenomena at the price of a full nonlinear analysis. A one-dimensional analytical model was first proposed by CHAI ET AL. [63] to investigate the buckling behavior of a delaminated composite structure. Following SIMITSES ET AL. [198, 199], proposing a one-dimensional beam-plate theory to predict the buckling loads and growth of delamination, the influences of delamination geometries and positions of the buckling loads are studied. KARDOMATEAS [200] and CHEN [201] include the shear deformation effect in the one-dimensional model which reduces the overestimation of the buckling load for a delaminated composite structure. Apart from the above one-dimensional models, BARBERO [202] proposes a layerwise plate theory to model the delamination in composite laminates, in which, the displacement field is enriched with a unit step function to allow for separation and slipping at delamination surfaces. LEE ET AL. [172] follows this layerwise approach to study the buckling problem of axially loaded composite beam plates based on the solution of an eigenvalue problem. The proposed layerwise approach yields accurate results at a reduced computing time. Most of the references above which address the buckling of single or multiple delaminations of laminated composites, e.g. [172], do not consider buckling modes where contact between delaminated plies occurs. In general, physically inadmissible mode shapes with overlapping plies may appear, hence, it is necessary to include a contact treatment in the buckling analysis of delaminated laminates. PECK AND

SPRINGER [203] include a contact model in the eigenvalue buckling analysis with reasonable results. Their contact model considers a delaminated ply resting on an elastic foundation. Regarding the contact problem, SUEMASU [204] adds imaginary springs between two delaminated layers to provide the resistance forces and moments eliminating the inadmissible mode shapes. The same idea is adopted in SEKINE's [205] and KOUCHAKZADEH's [195] work. A similar artificial spring approach based on contact forces is presented in HU [206] for Reissner-Mindlin plates. The contact forces of this approach are found from a sensitivity-based update iteration scheme.

In this chapter, a strong coupled multi-model approach including delaminations is presented and tested using several linear elastic benchmark problems in section 4.1. In section 4.2, the set of equations governing the linear buckling analysis is provided. We introduce the contact kinematics used in our method and a surface-to-surface contact element formulation. Various examples addressing accuracy, reliability and convergence behavior of the proposed contact extended linear buckling formulation are presented in section 4.3.

## 4.1 Strong coupled multi-model approach

The use of variationally coupled multiple patches [1, 90] in isogeometric analysis makes the joining of incompatible meshes and even different mechanical models possible. In the present work, through-the-thickness patch boundaries of LW and ESL models are connected, and thereby an attempt is made to limit computational time and costs while maintaining sufficient solution accuracy. The two patches shown in Figure 4.1 were chosen to illustrate the basic principles of the coupling concept applying different basis functions through the thickness of a laminate. The proposed concept even allows the coupling of incompatible patches. To the left of Figure 4.1 a layerwise model of cubic order is shown. Each of the two layers is modeled with a single knot-span element with a  $C^0$ -continuous interface in between, resulting in seven control points across the thickness direction of the composite laminate, to the right an equivalent single layer (ESL) model consisting of a single element of same polynomial order is given. The sets of control points  $\mathbf{P}^{(i)} (i = 1, 2)$  were split into subsets  $\mathbf{P}_f^{(i)}$  and  $\mathbf{P}_n^{(i)}$  for further considerations. The subscripts  $f$  and  $n$  denote the interface domain  $\Omega_f$  and the non-interface domain  $\Omega_n$ , respectively, whereas the superscripts identify the different models. The knot vector  $\Xi_1$  was obtained from  $\Xi_2$  by knot insertion. The relationship between the subsets of control points  $\mathbf{P}_f^{(1)}$  and  $\mathbf{P}_f^{(2)}$  along the coupling interface of the two patches was established by the extension operator  $\mathbf{T}_f$  which interpolates the additional control points of  $\mathbf{P}_f^{(1)}$  from the basic set of control points  $\mathbf{P}_f^{(2)}$ :

$$\mathbf{P}_f^{(1)} = \mathbf{T}_f \mathbf{P}_f^{(2)} \quad (4.1)$$

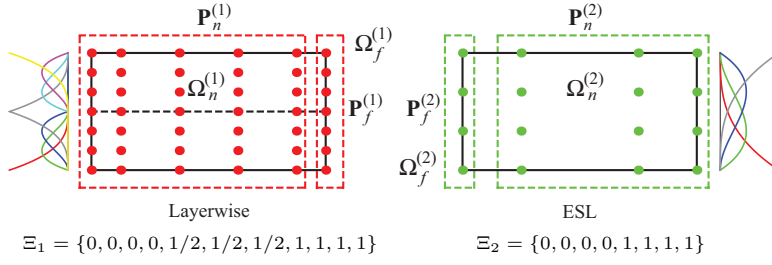


Figure 4.1: Multi-patch connection: distribution of the control points and applied basis functions over the laminate thickness, defined by the knot spans  $\Xi_1, \Xi_2$ .

Equation (4.1) maintains the  $C^0$ -continuity of the geometry across the interface between the two patches. The relation of the displacements introduced at the control points of each domain was established analogously:

$$\mathbf{U}_f^{(1)} = \mathbf{T}_f \mathbf{U}_f^{(2)} \quad (4.2)$$

The governing linear system of equations of each patch was split according to the degrees of freedom introduced at the corresponding control points of the subdomain  $\Omega_f$  and  $\Omega_n$ ,

$$\begin{pmatrix} \mathbf{K}_{nn}^{(i)} & \mathbf{K}_{nf}^{(i)} \\ \mathbf{K}_{fn}^{(i)} & \mathbf{K}_{ff}^{(i)} \end{pmatrix} \begin{pmatrix} \mathbf{U}_n^{(i)} \\ \mathbf{U}_f^{(i)} \end{pmatrix} = \begin{pmatrix} \mathbf{f}_n^{(i)} \\ \mathbf{f}_f^{(i)} \end{pmatrix}, \quad i = 1, 2 \quad (4.3)$$

Using (4.2) in (4.3), the coupled system of equations could be written in the form

$$\begin{pmatrix} \mathbf{K}_{nn}^{(1)} & \mathbf{K}_{nf}^{(1)} \mathbf{T}_f & \mathbf{0} \\ \mathbf{T}_f^T \mathbf{K}_{fn}^{(1)} & \mathbf{T}_f^T \mathbf{K}_{ff}^{(1)} \mathbf{T}_f + \mathbf{K}_{ff}^{(2)} & \mathbf{K}_{fn}^{(2)} \\ \mathbf{0} & \mathbf{K}_{nf}^{(2)} & \mathbf{K}_{nn}^{(2)} \end{pmatrix} \begin{pmatrix} \mathbf{U}_n^{(1)} \\ \mathbf{U}_f^{(2)} \\ \mathbf{U}_n^{(2)} \end{pmatrix} = \begin{pmatrix} \mathbf{f}_n^{(1)} \\ \mathbf{T}_f^T \mathbf{f}_f^{(1)} + \mathbf{f}_f^{(2)} \\ \mathbf{f}_n^{(2)} \end{pmatrix} \quad (4.4)$$

The unknown variables  $\mathbf{U}_f^{(1)}$  were condensed out and can be recovered using equation (4.2) [90].

#### 4.1.1 Multi-model stress analysis

In the following example, cylindrical bending of a simply supported cross-ply laminates with stacking sequence  $[0^\circ/90^\circ]$  is considered, cf. Figure 4.2. The plate is subjected to a spline shaped concentrated transverse load  $q(x) = q_0 N_2(x)$  at the top surface of the plate, where  $q_0$  is a constant and  $N_2(x)$  is quadratic spline function.

The material properties of the laminate are:

$$\begin{aligned} E_1 &= 2.5 \times 10^7 \text{psi}, & G_{13} &= 5.0 \times 10^5 \text{psi}, \\ E_3 &= 1.0 \times 10^6 \text{psi}, & G_{23} &= 2.0 \times 10^5 \text{psi}, \\ \nu_{13} &= \nu_{23} = 0.25. \end{aligned}$$

In this case, the critical areas may be located in the middle and at both ends of the structure, hence, two different multi-patch models were constructed to investigate the transverse normal stress, cf. Figure 4.2(a), in the middle of the laminate, and shear stress, cf. Figure 4.2(b), in the end areas of the laminate, where  $\alpha$  and  $\beta$  are the fraction of the length of the beam section modeled by layerwise model, and the span of a B-spline shape load with respect to the length of the plate  $w$ , respectively. The

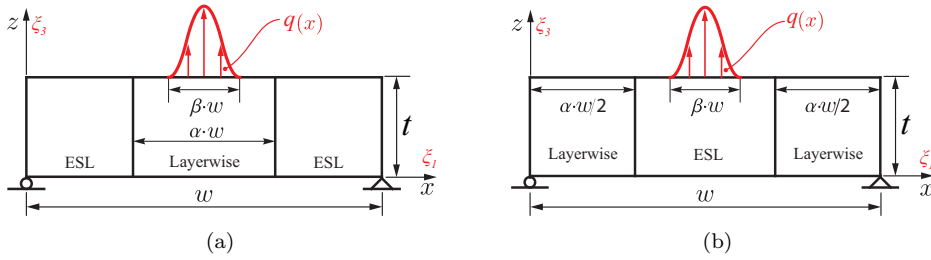


Figure 4.2: Model description. (a) Multi-patch model 1 with one layerwise model in the middle, two ESL models at the ends. (b) Multi-patch model 2 with one ESL model in the middle, two layerwise models at the ends.

influence of aspect ratios  $\alpha$  and  $\beta$  on the accuracy of transverse normal and shear stresses were evaluated for the work presented here, and all the resulting quantities presented were normalized according to equation (3.18).

The three dimensional exact solution was obtained from PAGANO'S work [42]. It is convenient to approximate the spline shape load using a Fourier series:

$$q(x) = q_0 N_2(x) \approx q_0 \sum_{n=1}^k f_n \sin\left(\frac{n\pi x}{w}\right) \quad (4.5)$$

where  $k$  depends on the required accuracy, and  $f_n$  can be calculated as:

$$f_n \approx \frac{2}{w} \int_0^w q(x) \sin\left(\frac{n\pi x}{w}\right) dx \quad (4.6)$$

Consequently, PAGANO'S exact solution could be found for each term in the summation of equation (4.5), and superimposed to obtain the total load  $q(x)$ .

The plots of normalized transverse normal and shear stresses,  $\bar{\sigma}_{33}$  and  $\bar{\sigma}_{13}$ , with different values of aspect ratio  $\alpha$  are shown in Figure 4.3. In this case, the number

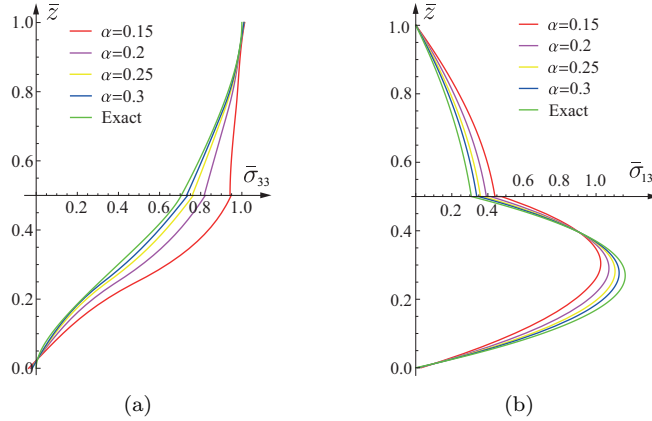


Figure 4.3: Plots of  $\bar{\sigma}_{33}$  and  $\bar{\sigma}_{13}$  with respect to  $\alpha$ , in which,  $\beta$  is set to be  $\beta = 0.1$ .

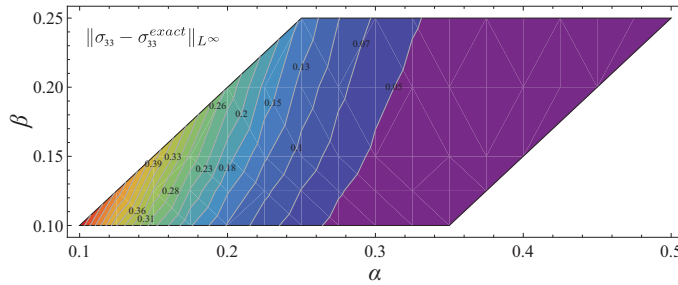


Figure 4.4: Error in the normal stress  $L_\infty$ -norm with respect to the  $\alpha$  and  $\beta$  parameters.

of through-the-thickness elements used in the ESL model and within each layer of the layerwise model were set to be  $n_l^{ESL} = 2$  and  $n_l^{LW} = 2$ , with the aspect ratio of each element being one. Looking at Figure 4.3, it can be seen that the stresses of  $\bar{\sigma}_{33}$  and  $\bar{\sigma}_{13}$  approach the three dimensional exact solutions along with the increase of aspect ratio  $\alpha$ , and very close results for both stresses to the exact solutions can be obtained rapidly using  $\alpha = 0.3$ .

Error studies with respect to PAGANO'S exact solutions were carried out for the stress components  $\bar{\sigma}_{33}$  and  $\bar{\sigma}_{13}$  and the results are shown in Figures 4.4 and 4.5. The parameter  $\beta$  represents the extent of load concentration. The values of  $\alpha$  and  $\beta$  change from  $\alpha = 0.1 \sim 0.5$  and  $\beta = 0.1 \sim 0.25$ , respectively, and  $\beta \leq \alpha$ , to assess the error of  $\bar{\sigma}_{33}$ . The influence of  $\alpha$  on the relative error of  $\bar{\sigma}_{13}$  is presented in Figure 4.5, the value  $\beta$  was kept constant at  $\beta = 0.1$ . The number of elements used through the thickness of the ESL and layerwise model was the same as adopted in Figure 4.3. In addition, the total load was kept constant when changing the value of  $\beta$ .

From Figure 4.4 we can see that the maximum error of  $\bar{\sigma}_{33}$  with respect to the exact solution decreased with an increase of either the value of  $\alpha$  or the value of  $\beta$ . Moreover, according to the contour plot, the maximum error was more sensitive to  $\alpha$  than to  $\beta$ . Once the load is determined, the designer can easily choose an  $\alpha$  according to the accuracy requirements of the analysis. The relationship between the maximum error of  $\bar{\sigma}_{13}$  and the value of  $\alpha$  is illustrated in Figure 4.5, as can be seen when  $\alpha$  was increased from 0.1  $\sim$  0.5, the maximum error decreased from 11%  $\sim$  0.54%, and the gradient of maximum error decreased gradually.

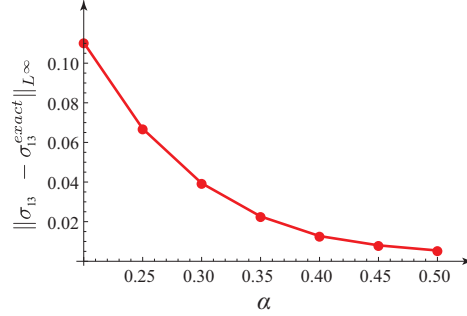


Figure 4.5: Error plot for  $\bar{\sigma}_{13}$  with respect to a varying value of  $\alpha$  at  $\beta = 0.1$ .

#### 4.1.2 Initial delaminations

The isogeometric layerwise model can be further generalized to model delaminations. The classical modeling approach of delamination enriches the displacement field with a *Heaviside* function to allow discontinuities at the ply interface [202, 172, 207]. In the isogeometric framework, the discontinuity condition can be simply ensured by knot repetition, cf. Figure 4.6, as discussed in section 2.1.4.

A schematic representation of a two layer laminate of cubic order with pre-existing delamination is shown in Figure 4.6. The laminated and delaminated regions were modeled as separate patches and connected according to the previous section. This technique is useful to assess stress intensity factors at the crack-tip and consequently to perform a preliminary laminate design.

We tested the multi-model approach for laminates with pre-existing delamination in a stress analysis. Thus, a two layered  $[0^\circ/90^\circ]$  laminate with a centrally located pre-existing delamination was considered as shown in Figure 4.7. The body was in a state of plane strain with respect to the  $xz$  plane. The material properties of the laminate are the same as those for the previous examples. The simply supported plate was subjected to a transverse sinusoidal load  $q(x) = q_0 \sin(\pi x/w)$  at the top surface of the plate, where  $q_0$  is a constant. Each layer is of equal thickness, and  $\alpha$  is the fraction of the length of delamination patch with respect to the length of the

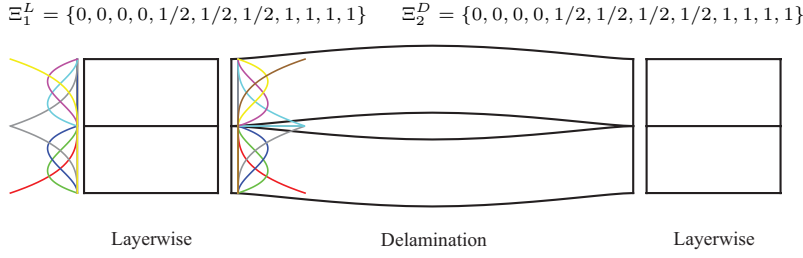


Figure 4.6: Strong coupled four patch delamination model

plate  $w$ . The presented quantities were normalized according to (3.18) except for  $\sigma_{13}$  which was normalized as:

$$\bar{\sigma}_{13} = \frac{\sigma_{13}(x, z_0)}{q_0} \quad (4.7)$$

where  $z_0$  designates the location of Gauss points nearest to the interface. The length-

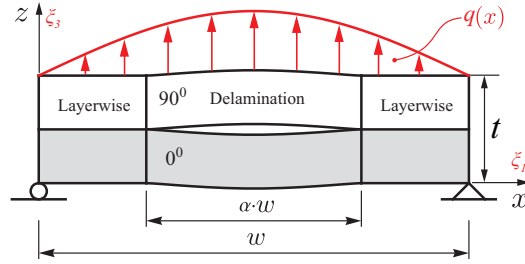


Figure 4.7: Layerwise model with delaminations.

to-thickness ratio was set to  $s = w/t = 5$ , and the aspect ratio of delamination patch with respect to the length of plate  $w$  was chosen to be  $\alpha = 0.4$ . The number of elements used through the thickness of each lamina was  $n_l = 2$  and the element aspect ratio was set to be one. In addition, the delamination model shown in [207] with linear displacement-strain relations was implemented for comparison. The results of the normalized transverse displacement  $\bar{u}_3$ , the shear stress  $\bar{\sigma}_{13}$  and the in-plane normal stress  $\bar{\sigma}_{11}$  obtained from the isogeometric model were in very good agreement with those given in reference [207], and are shown in Figures 4.8-4.10, respectively. From Figure 4.8 we can see that the transverse displacement exhibits an obvious jump at the delamination interface and amount of displacement jump is captured very well by the isogeometric delamination model. The same accuracy is obtained for the in-plane normal stress  $\bar{\sigma}_{11}$ . The location of the Gaussian quadrature points used to calculate the transverse shear stresses for both models is  $z_0 = 0.5281754 \cdot h$ . It is no surprise that the shear stress is symmetric about the beam center, as shown in Figure 4.10. The jumps in the stress at the interlaminar crack front indicate the

existence of a stress singularity.

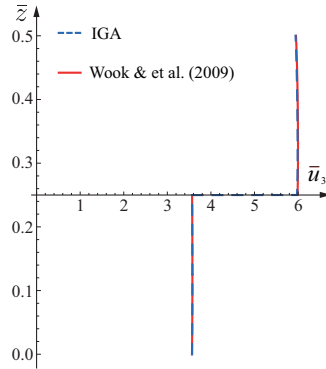


Figure 4.8: Distribution of transverse displacement  $\bar{u}_3$  through the thickness of a delaminated laminate.

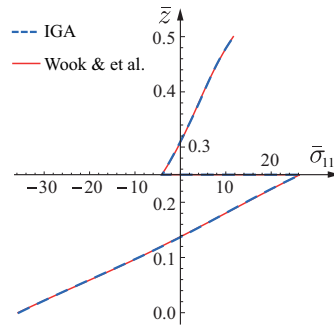


Figure 4.9: Distribution of in-plane normal stress  $\bar{\sigma}_{11}$  through the thickness of a delaminated laminate.

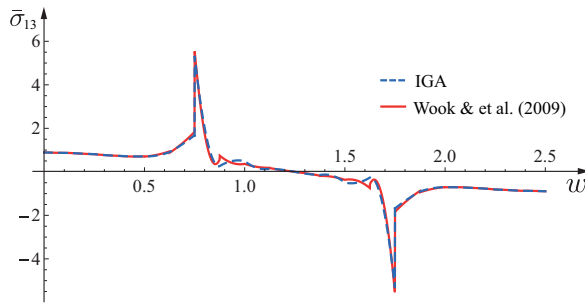


Figure 4.10: Distribution of transverse shear stress  $\bar{\sigma}_{13}$  along the length of a delaminated laminate.

## 4.2 Linear buckling analysis

Starting from the total potential energy of the 2D laminate model under transverse loading the equation governing the buckling analysis can be formulated as:

$$\Pi = \Pi_I + \Pi_E \quad (4.8)$$

with

$$\Pi_I = \frac{1}{2} \int_{\Omega} \mathbf{E} : \mathbf{S} \, d\Omega \quad (4.9)$$

representing the strain energy of the deformed system domain  $\Omega$  where  $\mathbf{E}(\mathbf{u}) (= \frac{1}{2}(\nabla \mathbf{u}^T + \nabla \mathbf{u}))$  denotes the linear strain tensor, and  $\mathbf{S}$  is the stress tensor introduced in (3.12). The potential of the external forces, restricted to a 1D in-plane loading across and along the boundary domain  $\Gamma$  as considered in this chapter is:

$$\Pi_E = \frac{1}{2} \int_{\Gamma_t} t_{x_0} \left( \frac{du_3}{dx} \right)^2 \, d\Gamma \quad (4.10)$$

The variable  $t_{x_0}$  denotes the prescribed membrane force and  $u_3$  represents the transverse displacement.

The quantities of (4.9) are discretized according to the interpolation rules introduced in chapter 2 with the displacement vector  $\mathbf{U} = [\mathbf{U}_1, \mathbf{U}_3]$  tailored to the state of plane strain. The change of  $u_3$  with respect to the global coordinate  $x_1$  follows by applying the chain rule with respect to the coordinate  $\xi$  of the NURBS parameter space:

$$\frac{du_3}{dx} = \sum_{k=1}^N \frac{dR_{k,p}(\xi, \eta)}{d\xi} \frac{d\xi}{dx_1} U_{k(3)} = \mathbf{N}_{,x_1}^T \mathbf{U}_3 \quad (4.11)$$

### Governing algebraic equations

Using the NURBS interpolation of the displacements and the strains of chapter 2 and using (4.11), the potential (4.8) can be discretized. The governing algebraic equations follow from element-wise integration and assembly of the element contributions to system level:

$$\Pi = \frac{1}{2} \mathbf{U}_s^T (\mathbf{K} - \mathbf{K}_G) \mathbf{U}_s \quad (4.12)$$

with  $\mathbf{U}_s = [\mathbf{U}_1, \mathbf{U}_3]$ ,  $\mathbf{K}$  the linear-elastic stiffness matrix of the system and

$$\mathbf{K}_G = A_e^{n_e} \left\{ \int_{x_3} t_{x_0} \mathbf{N}_{,x_1}^T \mathbf{N}_{,x_1} \, dx_3 \right\}_e \quad (4.13)$$

representing the assembly of the geometric element stiffness matrices due to the applied membrane forces. From the stationary condition  $\delta\Pi = 0$  follows the eigenvalue problem:

$$(\mathbf{K} - \lambda \mathbf{K}_G) \mathbf{U}_s = \mathbf{0} \quad (4.14)$$

with the critical load factor  $\lambda$  determined as the eigenvalue of smallest magnitude [208, 154].

#### 4.2.1 Contact model enriched buckling analysis

The buckling eigenvalue problem (4.14) is unconstrained in the sense that the upper and lower delaminated layers can move in the lateral direction independently. As a consequence, physically inadmissible buckling modes may appear that include penetration between the upper and lower delaminated layers. This phenomenon is illustrated in Figure 4.11 where it can be seen that local buckling has induced a partial penetration of the upper ply into the lower region. In the following we propose

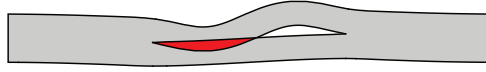


Figure 4.11: Inadmissible buckling mode of penetrating plies.

a contact model to “repair” stepwise inadmissible buckling modes. In general, a contact search algorithm is required to determine which parts of the delaminated regions are in contact. In the following, we model all delaminated regions with a single patch which makes an expensive global contact search superfluous and restricts any contact search locally to the patch level.

#### Contact kinematics

Let  $\mathbf{x}^{(a)}$  ( $a = 1, 2$ ) denote the position of a material point in  $\Omega^{(a)}$  and let  $\Gamma^{(a)}$  denote the boundary of  $\Omega^{(a)}$ , specifically, the opposite boundaries of the delaminated regions as illustrated in Figure 4.12. We assume the lower and upper delamination domains to be convex regions or at least locally convex regions, such that for any given point  $\mathbf{x}^{(2)} \in \Gamma^{(2)}$ , there exists a unique point  $\mathbf{x}^{(1)} \in \Gamma^{(1)}$  that satisfies the minimum distance condition

$$d(\xi) = \min_{\mathbf{x}^{(1)} \in \Gamma^{(1)}} \left\| \mathbf{x}^{(2)} - \mathbf{x}^{(1)}(\xi) \right\| \quad (4.15)$$

where  $\xi$  is the coordinate of the corresponding NURBS parameter space  $\Xi$  that is, for convenience, chosen in the interval  $[0, 1]$ . The point  $\hat{\mathbf{x}}$  indicates the closest projection point, thus satisfying (4.15). The determination of  $\hat{\mathbf{x}}$  requires the inverse mapping  $\xi(\mathbf{x})$  of the geometry interpolation rule satisfying the condition for a minimum of the distance function [209]

$$\frac{\mathbf{x}^{(2)} - \hat{\mathbf{x}}^{(1)}(\xi)}{\|\mathbf{x}^{(2)} - \hat{\mathbf{x}}^{(1)}(\xi)\|} \cdot \hat{\mathbf{x}}^{(1)}(\xi) = \mathbf{n}^{(1)} \cdot \hat{\mathbf{x}}^{(1)}(\xi) = 0 \quad (4.16)$$

A Newton iteration is applied to determine the parametric coordinate  $\xi$  such that equation (4.16) is satisfied, with  $i$  indicating the current iteration step. Starting

from the  $i^{th}$  iteration step we determine the new value of  $\xi$  using:

$$\xi_{i+1} = \xi_i - \frac{\mathbf{x}_{,\xi}^{(1)}(\xi_i) \cdot [\mathbf{x}^{(1)}(\xi_i) - \mathbf{x}^{(2)}]}{\mathbf{x}_{,\xi\xi}^{(1)}(\xi_i) \cdot [\mathbf{x}^{(1)}(\xi_i) - \mathbf{x}^{(2)}] + |\mathbf{x}_{,\xi}^{(1)}(\xi_i)|^2} \quad (4.17)$$

where  $\mathbf{x}_{,\xi}^{(1)}(\xi)$  and  $\mathbf{x}_{,\xi\xi}^{(1)}(\xi)$  signify the first and second derivative of  $\mathbf{x}^{(1)}$  with respect to the parametric coordinate  $\xi$ . With knowledge of  $\hat{\mathbf{x}}(\xi)$  the relative position of the lower and upper boundaries can be characterized by the gap function:

$$g_n = [\mathbf{x}^{(2)} - \hat{\mathbf{x}}^{(1)}(\xi)] \cdot \mathbf{n}^{(1)} \quad (4.18)$$

in which  $\mathbf{n}^{(1)}$  is the outward pointing unit normal at  $\hat{\mathbf{x}}^{(1)}$  on  $\Gamma^{(1)}$ .

Using the value of  $g_n$  the contact situation can be uniquely characterized [210]. For  $g_n > 0$  the boundaries are separated, whereas  $g_n < 0$  indicates penetration of the domains. For  $g_n = 0$  perfect contact exists between  $\Gamma^{(1)}$  and  $\Gamma^{(2)}$ .

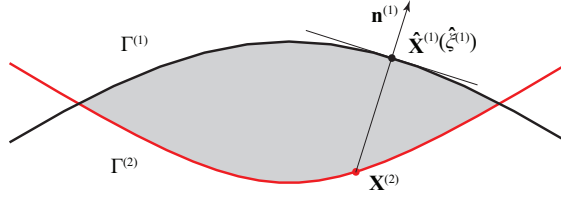


Figure 4.12: The closest point projection.

The contact formulation is significantly simplified by the fact that tangential contact is not considered for the presented buckling analysis thus omitting any complex friction model. All constituents of the following formulation therefore refer to the normal contact of the delaminated plies.

### Surface-to-surface contact element formulation

We follow a master-slave concept to account for the non-symmetry of the gap function, where  $\Gamma^{(1)}$  is chosen as the master and  $\Gamma^{(2)}$  the slave surface of a surface-to-surface contact element comprising contact conditions at a set of Gaussian quadrature points and corresponding projection points along the contact boundary. The Gaussian quadrature points are denoted  $\mathcal{G}^{(2)}$ , as they are located on the boundary  $\Gamma^{(2)}$ . Based on a penalty formulation, the potential (4.8) is extended by a *penalty energy* term. The variation of this contact potential energy term is written as:

$$\delta \Pi_c = \int_{\Gamma_c} \epsilon g_n \delta g_n ds \quad (4.19)$$

where  $\epsilon$  denotes the penalty factor,  $\Gamma_c = \Gamma^{(1)} \cap \Gamma^{(2)}$  denotes the contact boundary, and  $ds$  denotes the length of the delamination boundary  $\Gamma^{(2)}$ . The variation of the gap function includes the variation of (4.16) and simplifies due to the orthogonality properties of  $g_n$  to the variation of its constituents. Substitution of (4.18) into (4.19) gives:

$$\delta \Pi_c = \int_{\Gamma_c} \epsilon \left[ \mathbf{x}^{(2)} - \hat{\mathbf{x}}^{(1)}(\xi) \right] \cdot \left[ \delta \mathbf{x}^{(2)} - \delta \mathbf{x}^{(1)} \right] ds \quad (4.20)$$

The geometry and the variation of equation (4.20) is discretized with NURBS. The integral in equation (4.20) is evaluated at a set of Gaussian quadrature points which are also used for the calculation of closest projection points. Through linearization, the contact stiffness can be written as:

$$\mathbf{K}_c = \begin{bmatrix} \mathbf{K}_c^{(11)} & -\mathbf{K}_c^{(12)} \\ -\mathbf{K}_c^{(21)} & \mathbf{K}_c^{(22)} \end{bmatrix} \quad (4.21)$$

where  $\mathbf{K}_c^{(ab)}$ , ( $a, b = 1, 2$ ), are the simplified components from the reference [211], and its formulation in element level is written as:

$$\mathbf{K}_{c(mn)}^{(ab)} = \sum_{i \in \mathcal{G}^{(2)}} \epsilon w_i J^{(2)}(\xi_{gi}) R_m^{(a)}(\xi_{ai}) R_n^{(b)}(\xi_{bi}) [\mathbf{I}] \quad (4.22)$$

where  $a, b$  and  $m, n$  denote the indices of the contact surfaces and the basis functions, respectively,  $w_i$  are the weights of the Gaussian quadrature,  $J^{(2)}(\xi_{gi})$  is the Jacobian of the boundary  $\Gamma^{(2)}$  and can be calculated as  $J^{(2)} = ds^{(2)}/d\xi = \|d\mathbf{x}^{(2)}/d\xi\|$ , and  $R_m^{(a)}$  and  $R_n^{(b)}$  are the NURBS basis functions corresponding to the contact surfaces  $\Gamma^{(a)}$  and  $\Gamma^{(b)}$ . The parameter  $\xi_{gi}$  corresponds to the  $i$ th Gaussian quadrature points in the set  $\mathcal{G}^{(2)}$ , and the parameters  $\xi_{ai}$  and  $\xi_{bi}$  correspond to either the set of closest projection points  $\xi_{pi}$ , when  $a, b = 1$ , or Gaussian quadrature points  $\xi_{gi}$ , when  $a, b = 2$ . In addition,  $\mathbf{I}$  is the  $2 \times 2$  identity matrix.

Notice that, it is shown in [205, 195] how the penetration of the inadmissible buckling states can be eliminated by adding fictitious springs between the overlapping nodes. This approach works well but is limited to the case of matching nodes along the two delaminated layers. Correspondingly, the control points of the NURBS modeled contact domains can be employed in the isogeometric analysis approach presented here, if a matching set of control points can be found for both domains. In general, this is not the case and thus requires a more sophisticated approach. An example of non-matching control points between the delaminated laminas is shown in Figure 4.13.

### Analysis concept

We propose a stepwise procedure, illustrated in Figure 4.14, to remove iteratively the domain overlap of inadmissible buckling states. The input data of the shown

flowchart is a buckling shape with overlapping plies, an inadmissible state that is found from a segment-to-segment contact search. The iteration loop comprised the following steps:

1. In a first step we determined the maximum overlap of the plies for the given buckling mode and check against a given threshold  $\mu$  which controls the desired accuracy of the enforced contact constraint.
2. For an overlap larger than  $\mu$  we introduced a penalty constraint for each Gauss point along the delaminated boundary of the slave domain  $\Gamma^{(2)}$  that does not satisfy the relation  $g_n > 0$  to close the gap function at  $\mathbf{x}^{(2)}(\xi_{gi})$ . The stiffness matrix was updated with the penalty contribution.
3. The general eigenvalue problem (4.14) was solved for the eigenstates with eigenvalue of smallest magnitude using a subspace eigenvalue solver.
4. We check the updated eigenstate for a change in the sign and flip over if necessary by scaling with  $(-1)$ .
5. We continue the loop until the stopping criteria, formulated in 1, is satisfied.

The iterative procedure of the proposed analysis concept for inadmissible states is necessary for two reasons. One, direct constraining of the original buckling eigenvalue analysis is not possible since a possible overlap and the corresponding overlap location are a priori unknown. Two, a single step solution does not prevent more inadmissible overlap configurations.

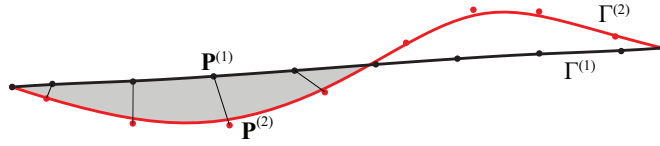


Figure 4.13: Overlapping NURBS-domain edges with non-matching control points.

### 4.3 Buckling of delaminated composites

The performance of the proposed isogeometric analysis contact approach with regard to reliability, accuracy and numerical effort is analyzed in the following for variable model parameters. We show the effects of stacking sequences of the laminates and the influence of different values of slenderness. We further dissect the influence of the position and length of the delamination zone.

Throughout the following numerical analyses we demonstrate our tests using a two layer laminate plate structure with pre-existing delamination at the ply interface and clamped essential boundary conditions. The geometry of the structure and its

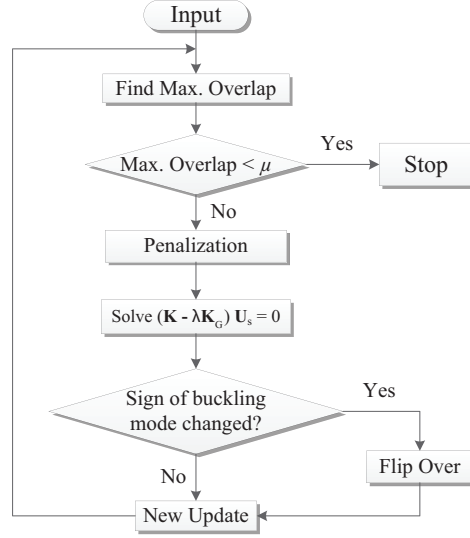


Figure 4.14: Iterative contact extended analysis concept for inadmissible buckling states.

delamination zone, the material parameters and the applied loading is depicted in Figure 4.15. A state of plane strain with respect to the  $x - z$  plane is assumed for all the derived model configurations.

We introduce two geometric parameters, normalized to the total plate length  $L$ . A form parameter  $\alpha$  is defined as the ratio of the delamination length with respect to the plate length  $L$ . A location factor  $\beta$  is used to denote the location of the delamination factor with respect to the length  $L$ . A fixed thickness is chosen for all layers of the laminated composite structure.

### 4.3.1 Convergence study and contact demonstration

The convergence study of a  $[0^\circ/0^\circ]$  lay-up laminate was carried out with different discretization levels. The orthotropic material properties are:

$$\begin{aligned}
 E_1 &= 1.81 \times 10^2 \text{ GPa}, & G_{13} &= G_{23} = G_{12} = 7.17 \text{ GPa}, \\
 E_3 &= 1.03 \times 10^1 \text{ GPa}, & \nu_{13} &= \nu_{23} = 0.28.
 \end{aligned}$$

The geometric model has a slenderness  $S = L/t = 10$  and delamination zone parameters  $\alpha = 0.4$  and  $\beta = 0.5$ . A  $h$ -refinement study followed by a  $p$ -refinement study is used to reveal the basic convergence properties of the proposed analysis approach. For the  $h$ -refinement study, each layer of the laminated composite was modeled with cubic NURBS in both the in-plane and through-thickness directions. The number of elements through the thickness of each single ply varied from 1 to 8 such that a

unit aspect ratio for each element was preserved. Monotonic convergence behavior is shown in Figure 4.16. An approximation for the exact reference solution was found from an extrapolation based on the results of the three most refined models [212].

For the  $p$  study, we kept the number of elements through the thickness of each

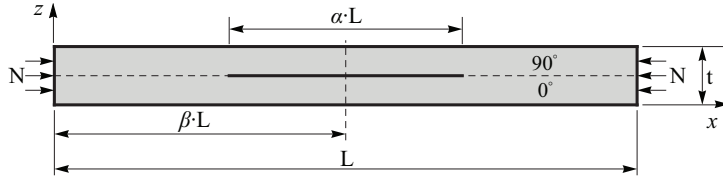


Figure 4.15: Delamination model of a two layer composite plate.

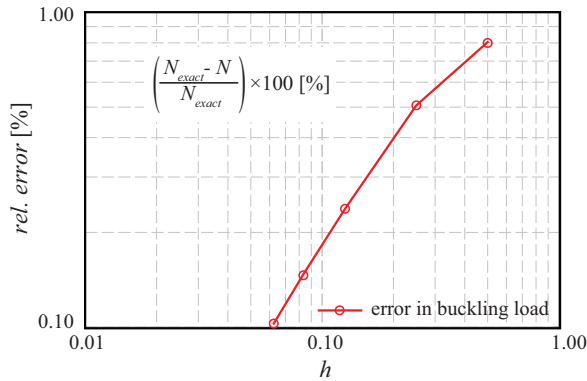


Figure 4.16: Convergence of the critical buckling load for a  $[0^\circ/0^\circ]$  laminate.

layer at 4, and uniformly increased the degrees of basis from  $p, q = 2$  to  $p, q = 6$  in both directions. The results are listed in the table 4.1, where  $N$  is the critical buckling load and  $\Delta$  is the relative error in percent with respect to the reference solution extrapolated from the  $h$ -refinements study. Again monotonic behavior was observed. The effectiveness of the proposed contact treatment is illustrated in the

Table 4.1: Convergence of the buckling load for  $p$ -refinement of a  $[0^\circ/0^\circ]$  laminate, providing buckling loads  $N$  and relative error  $\Delta$ .

	$p, q = 2$	$p, q = 3$	$p, q = 4$	$p, q = 5$	$p, q = 6$	exact
$N[\times 10^2]$	12.414	12.389	12.378	12.373	12.369	12.359
$\Delta[\%]$	0.445	0.243	0.154	0.113	0.081	-

following. The stacking sequence of the laminate was changed to  $[0^\circ/90^\circ]$ . The geometric parameters and the delamination zone parameters of the model were kept the same as in the previous example.

The buckling analysis revealed the first buckling mode to be admissible and the second buckling mode to be inadmissible with penetrating plies for which a contact analysis was performed. The history of the stepwise contact analysis starting from the initial inadmissible state to the final accepted buckling state is illustrated in Figure 4.17. A penalty value of ( $\epsilon = 10^{10}$ ) was found to be sufficient for convergence

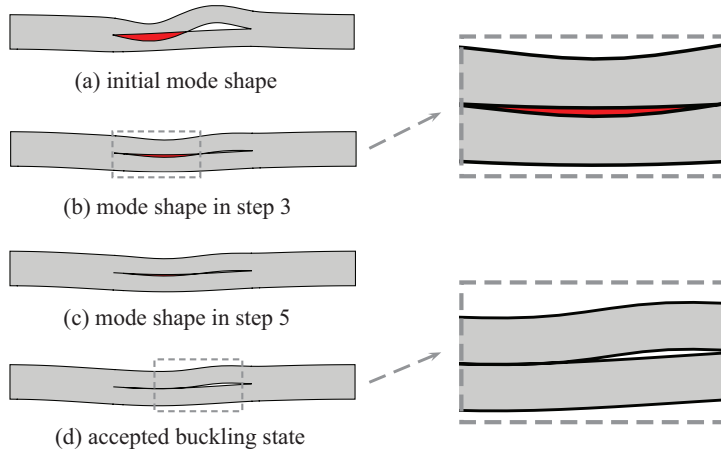


Figure 4.17: History of the contact extended buckling analysis of the second buckling mode.

and was kept constant throughout the iteration procedure. The final mode shape with contact constraints is presented in Figure 4.17(d). The overlap region at the various iteration steps, shown in red in Figure 4.17, decreases with an increasing number of iterations until the final admissible buckling state has converged with a buckling load of  $7.733 \times 10^2$  N.

The free scalability of the eigenvectors allowed us to consider both eigenmodes,  $\mathbf{u}$  and  $-\mathbf{u}$  as valid solutions. Nevertheless, for local buckling modes scaling with  $-1$  may result in another, or even new, overlap situation as depicted in Figure 4.18, in which the stacking sequence of the laminate is  $[0^\circ/90^\circ]$  and the geometric and delamination zone parameters of the model are:  $S = L/t = 10$ ,  $\alpha = 0.5$  and  $\beta = 0.5$ . As a consequence the flip-over scaled mode shape must be considered in the buckling analysis as a separate solution that possibly requires a contact enriched analysis as proposed in this chapter. The third buckling mode shown in Figure 4.18 has already been identified as an inadmissible mode without negative scaling. A small overlap at the middle of the delamination zone was noticed, and the negative counterpart strongly illustrates the overlap problem for a flip-over situation. The buckling mode shapes after the contact analysis are shown in Figure 4.19. The corresponding buckling loads were  $6.497 \times 10^2$  N and  $16.062 \times 10^2$  N, respectively. The lower of the two buckling load and corresponding mode shape was considered to be the relevant solution.

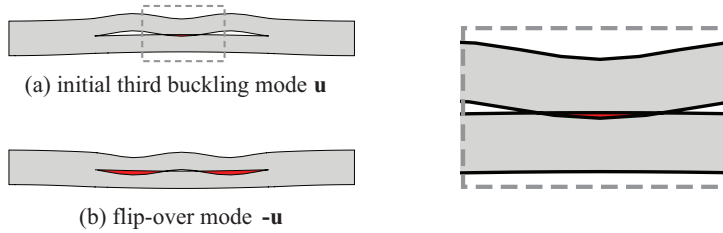


Figure 4.18: Overlap situation from a flip over of a local buckling mode by scaling with  $-1$ .

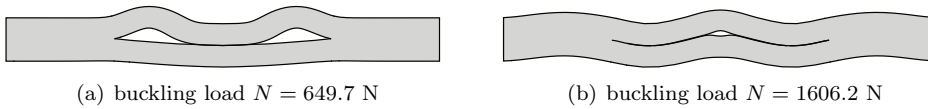


Figure 4.19: Final result for the third buckling mode after necessary overlap correction from flip over.

### 4.3.2 Midplane delamination of a $[0^\circ/0^\circ]$ laminate

The following benchmark model has been used in several publications as a test case for the buckling analysis of laminate composites providing reference solutions of similar quality [198, 201, 172, 206]. We chose the same example to demonstrate the accuracy of the proposed contact extended buckling analysis and to compare our solution to the results reported in the literature. The geometry, the material properties and loading conditions of the current example correspond to the model depicted in Figure 4.15. The stacking sequence of the laminate was chosen as  $[0^\circ/0^\circ]$ .

In a first test we analysed the influence of the delamination length, expressed by the form parameter  $\alpha$ , on the buckling load of the first buckling mode. The model had a length-to-thickness ratio of  $S = L/t = 400$  and a location factor of  $\beta = 0.5$ . The presented normalized buckling loads were obtained by dividing the critical buckling loads of the delaminated plate with  $N_{cr}$ , the buckling load of the laminated composite structure without delamination.

Our solution compared to the reference solutions found in [198, 201, 172, 206] is shown in table 4.2. A very good overall agreement of the buckling loads was observed for an increasing value of  $\alpha$ . Most of the buckling modes were global symmetric with a relative deviation from our solution of below  $\sim 0.3\%$ . Except for  $\alpha = 0.4$  where we obtained an anti-symmetric buckling mode. For this case the solution obtained in CHEN [201] is a global symmetric one and seems to be an outlier result with a relative deviation of above  $1.1\%$ . This is attributed to the fact that symmetry assumptions in the axial direction were made in [201], thus excluding anti-symmetric modes. In a second test we varied the values of  $\alpha$  and computed the buckling loads for global symmetric, anti-symmetric and local symmetric buckling modes. The length-to-

Table 4.2: Comparison of normalized buckling loads for an increasing form parameter  $\alpha$ : present solution, reference values and relative deviation  $\Delta$ [%].

$\alpha$	Simitses[199]	$\Delta$ [%]	Chen[201]	$\Delta$ [%]	Lee[172]	$\Delta$ [%]	Hu[206]	$\Delta$ [%]	<b>Present</b>
0.1	0.9999	0.00	0.9999	0.00	0.9999	0.00	-	-	0.9999
0.2	0.9956	0.02	0.9956	0.02	0.9956	0.02	-	-	0.9954
0.3	0.9638	0.07	0.9638	0.07	0.9639	0.08	0.9606	0.26	0.9631
0.4	0.8481	0.15	0.8561	1.10	0.8482	0.17	0.8445	0.27	0.8468
0.5	0.6896	0.29	0.6896	0.29	0.6898	0.32	0.6860	0.23	0.6876
0.6	0.5411	0.26	0.5411	0.26	0.5413	0.30	0.5384	0.24	0.5397
0.7	0.4310	0.23	0.4310	0.23	0.4311	0.26	0.4288	0.28	0.4300

thickness ratio for this test was set to  $S = L/t = 10$ . Our results were compared to a reference solution provided by JAEHONG [172] and are shown in Figure 4.20, in which a displacement-based one-dimensional finite element model based on Reddy's layerwise plate theory is used. The results of the proposed isogeometric buckling analysis agreed very well with the reference solution. No difference can be observed for the global symmetric and anti-symmetric modes virtually. The IGA solution of the local symmetric case deviated only insignificantly from the reference curve showing a slightly smoother curve. The slight deviation can be explained by the different kinematic models been used for this example. In JAEHONG [172], the out-of-plane displacement  $u_3$  is assumed to correspond to the mid-surface displacement, which means no relative displacement exists through the thickness of a laminate. In contrast, in our isogeometric layerwise model, both the in-plane and out-of-plane displacement components are interpolated using NURBS basis functions, hence allowing for the change of the displacements through the thickness direction.

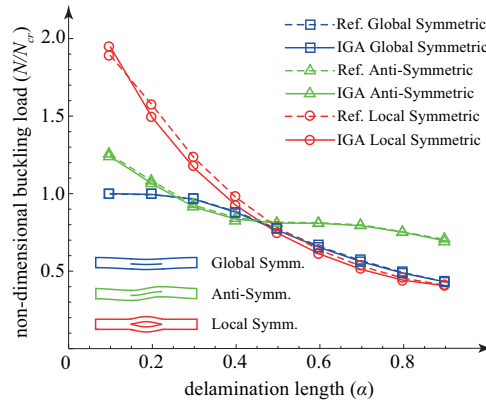


Figure 4.20: Buckling loads for an increasing delamination length.

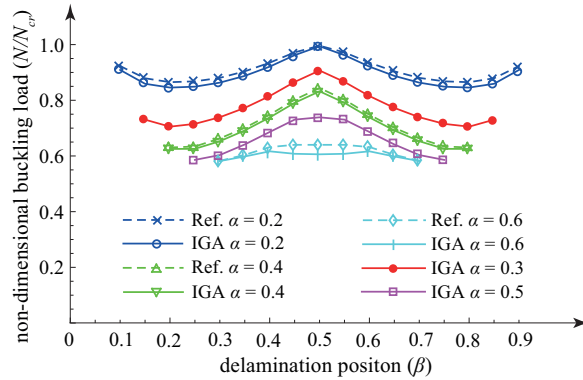


Figure 4.21: Influence of the delamination zone position on the buckling load for a  $[0^\circ/0^\circ]$  laminate.

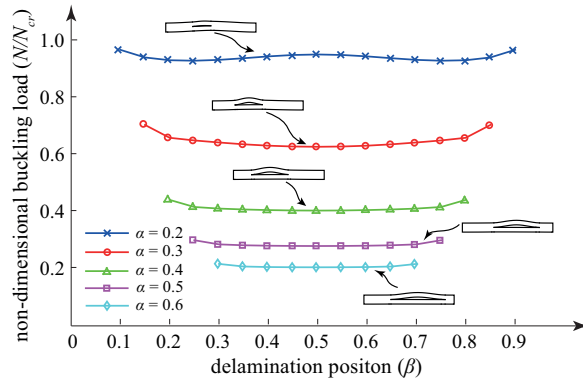


Figure 4.22: Influence of the delamination zone position on the buckling load for a  $[0^\circ/90^\circ]$  laminate.

### 4.3.3 Influence of the axial location of delamination

The following reveals the influence of the axial location of the delamination, expressed by the location factor  $\beta$ , on the first buckling mode and corresponding buckling load. In Figures 4.21 and 4.22, respectively, we show results for both stacking configurations, the  $[0^\circ/0^\circ]$  and  $[0^\circ/90^\circ]$  laminates. In addition, the reference results from JAEHONG [172] are also shown in Figure 4.21. The depicted curves represent different dimensions of the delamination zone, expressed by the form factor  $\alpha$ . The length-to-thickness ratio  $S = L/t$  for this analysis was set to  $S = 10$ .

With a value  $\beta = 0.5$ , indicating the delamination zone in the center of the plate, the symmetry of the model and location of the delamination zone clearly dominated the results with a maximum value of the buckling load, cf Figure 4.21. With increasing

delamination length  $\alpha$  the peak value smoothed out and even dropped down for the IGA solution at  $\alpha = 0.6$  indicating severe loss of stiffness as consequence of the large delamination zone.

For the short delamination length models,  $\alpha = 0.2$  and  $\alpha = 0.3$ , respectively, we observed an increased stiffening in the case where the delamination center moves towards the ends of the plate. This behavior is reducible to the clamped boundary conditions applied at the ends of the plate and becomes more obvious for the smaller delamination zones. For longer delamination zones, e.g.  $\alpha = 0.5$  and  $\alpha = 0.6$ , the buckling loads were less sensitive to the delamination locations, and stayed almost unchanged for  $\beta$  between 0.45 and 0.55.

The variation of  $\alpha$  and  $\beta$  for the  $[0^\circ/90^\circ]$  laminate composite are depicted in Figure 4.22. The buckling load showed significant less sensitivity to the location of the delamination and the size of the delamination zone, compared to the  $[0^\circ/0^\circ]$  stacking results shown in Figure 4.21. Analogously, increasing stiffness of the delaminated plate towards the ends was observed.

### 4.3.4 Influence of the contact constraints

We use the following example to show the influence of the introduced contact constraints on the results of the buckling analysis. We considered the first three buckling modes and corresponding loads of the  $[0^\circ/90^\circ]$  laminated composite model introduced earlier. The results for  $\alpha = 0.4$  and  $\alpha = 0.6$ , respectively, with varying location factor  $\beta$  are shown in Figures 4.23 and 4.24. The first buckling mode was

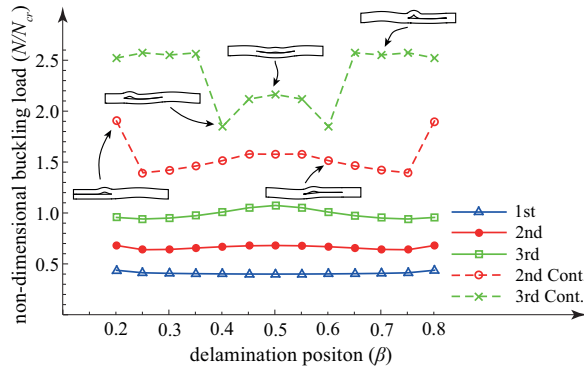


Figure 4.23: Influence of the contact constraints on the buckling load of a  $[0^\circ/90^\circ]$  laminate composite with  $\alpha = 0.4$ .

found to be uncritical for both cases,  $\alpha = 0.4$  and  $0.6$ , since no overlap appeared. We concentrated on the second and third buckling mode which were both inadmissible due to an overlap in the initial analysis step. As demonstrated before, the stepwise

introduced constraints significantly influenced the final mode shape and corresponding buckling load. For the second and third buckling mode of both cases ( $\alpha = 0.4$

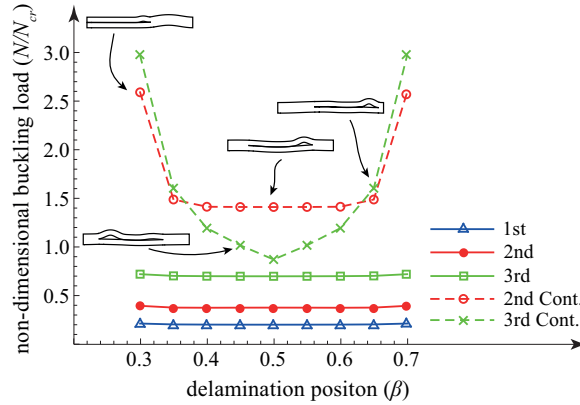


Figure 4.24: Influence of the contact constraints on the buckling load of a  $[0^\circ/90^\circ]$  laminate composite with  $\alpha = 0.6$ .

and  $\alpha = 0.6$ ), the buckling loads after contact repair increased evidently compared to the original inadmissible states. In both cases we observed the highest buckling load for the delamination zone located at the boundary of the structure. This stiff boundary phenomenon was more evident when the delamination length increased. For  $\alpha = 0.4$  the buckling load of the second mode jumped down followed by a monotonic increase when relocating the center of the delamination zone towards the center of the structure. With increasing length of the delamination zone, cf  $\alpha = 0.6$ , the curves for the second mode flatten, i.e. the buckling load became less sensitive with respect to location of the delamination zone. The third buckling mode showed reverse behavior. The buckling load decreased for a relocation of the buckling zone towards the center of the structure, however, an analogous decreasing sensitivity of the buckling load with increasing delamination size was observed as noticed already for the second buckling mode.

It is worth noting that at the center positions the initially lower buckling load of the second buckling mode for  $\alpha = 0.6$  changed to a load higher than the load of the third mode after repair. Obviously the second and third buckling state changed significantly in both, buckling mode and buckling load.

### 4.3.5 A model with two delaminations

We will now demonstrate the applicability and extensibility of the proposed approach for two or more delamination zones. We used a model of a random short-fiber composite structure with two delaminations near to the surface. The problem was first analysed by WANG [213]. The geometric parameters and the delamination

parameters are shown in Figure 4.25. The length-to-thickness ratio was set to  $S = L/t = 16$ , and the center of each delamination zone was located in the middle of the structure ( $\beta = 0.5$ ). The two delamination cracks were located symmetrically to the middle surface of the structure with a deepness parameter  $t_d = 0.25t$ . The orthotropic material properties of the composite are:

$$\begin{aligned} E_1 &= 2.29 \times 10^6 \text{ psi}, & G_{13} &= G_{23} = G_{12} = 0.36 \times 10^6 \text{ psi}, \\ E_3 &= 1.2 \times 10^6 \text{ psi}, & \nu_{13} &= \nu_{23} = 0.22. \end{aligned}$$

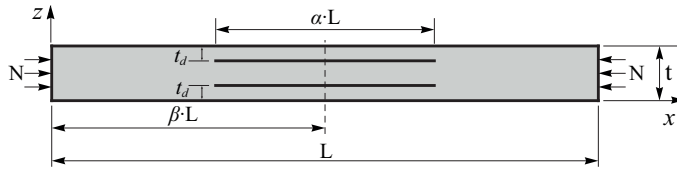


Figure 4.25: Two symmetrically located delaminations through the thickness.

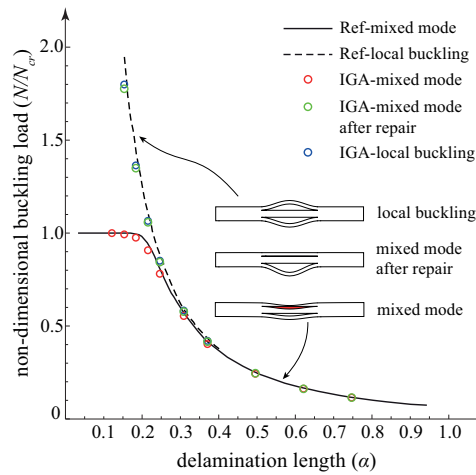


Figure 4.26: Normalized buckling loads vs delamination length for a random short-fiber composite with two delamination cracks.

In the isogeometric layerwise approach, the above model can be modeled as a four layered laminate with equivalent material properties for each layer. Two buckling modes were considered in this example, a mixed mode combining global and local buckling and a local buckling mode, which were normalized with the critical buckling load ( $N_{cr}$ ) of an undelaminated composite. The two buckling modes obtained using the isogeometric model were plotted against the delamination length parameter  $\alpha$ ,

and compared to the reference solutions provided by WANG [213], cf Figure 4.26. In Figure 4.26, the red points represent the mixed buckling modes and the blue points refer to the local buckling modes. Most of the mixed buckling modes are inadmissible buckling states as depicted in Figure 4.26. Thus, a contact treatment was added to *repair* the overlap of the above modes. The normalized *repaired* buckling load values of the mixed modes are plotted in green in Figure 4.26. Both the mixed mode and local buckling mode of the isogeometric model agreed very well with the reference solutions. The repaired buckling loads of the mixed modes were slightly lower than the local buckling modes. This seemed to be reasonable because the repaired buckling modes were locally dominant with only one buckle layer while the local buckling modes have two buckle layers.

## 4.4 Summary

A multi-model analysis technique was developed and discussed in this chapter, this enabled us to use either an equivalent-single-layer or the proposed layerwise theories within the different regions of a structural model. The approach was extended to investigate laminates with pre-existing damage, i.e. delamination. The method was compared to existing solutions and shown to be in good agreement for both the displacement and stresses values that were obtained.

In addition, the buckling of laminated composite plate-like structures with pre-existing delamination zones was studied. The particular focus of the presented analysis concept was the *repair* of physically inadmissible buckling states with overlapping plies concentrating the developed procedure and the numerical studies on the through-thickness behavior of the relevant buckling states with smallest buckling load. Based on the multi-patch strong coupling approach, the delaminated zone was enriched by additional stiffness contributions considering the normal contact force of the overlap domain. Using a step-wise procedure we demonstrated the ply overlap reduction towards physically admissible buckling modes.

Using several numerical examples we revealed the reliability and accuracy of the proposed procedure. A refinement study showed monotonic convergence of the buckling load for uniform h-refinement and uniform p-refinement of the contact enriched model. We demonstrated the influence of the free scalability of the inadmissible buckling modes from the eigenvalue analysis on the finally repaired buckling state and corresponding buckling load. We further showed the decrease of the buckling load for increasing delamination and compared our results to finite element approximations taken from the literature, with overall high agreement. A detailed study on the influence of size and position of the delamination zone was done which revealed the strong dependencies for the final buckling load and buckling shape. The buckling load tended to increase for a relocation of the buckling zone towards the boundary of the composite structure. For a  $[0^\circ/90^\circ]$  laminate, in which the material properties of the two plies vary greatly, the penetration phenomenon was observed to be more

likely than for a  $[0^\circ/0^\circ]$  stacking, with large influence on buckling load and buckling mode. Using a four layer model we showed the applicability of our proposed method for composites in the presence of multiple delaminations. A comparison of the results to a reference FEM solution proved reliability and accuracy of our method, an indispensable prerequisite for future studies of more complex shell-like structures.



## Chapter 5

# Analysis of multi-patch models for thin-walled structures<sup>1,2</sup>

Thin-walled structures demonstrate optimal load-carrying behavior and are of major importance in the design of structures in aerospace and automotive engineering. Using higher order and higher continuity NURBS basis of isogeometric analysis, a rotation-free shell element can be formulated based on the Kirchhoff-Love theory. An isogeometric rotation-free shell element does not need extra rotational degrees of freedom which saves computational efforts compared to Reissner-Mindlin type shell elements. The kinematics of the isogeometric shell formulation can be described fully with translational degrees of freedom of mid-surface. In addition, second order derivatives of the basis functions are needed to describe the change of curvature of the shell mid-surface.

The absence of rotational degrees of freedom in the formulation lends the formulation the label ‘rotation-free’ and requires special treatment of essential boundary conditions to regain control of rotatory constraints along the shell mid-surface [214]. In [215] it is shown that clamped or symmetric boundary conditions can be maintained if the direction of the tangent normal to the geometry boundary is preserved during deformation. The above is also a challenge for the continuity-preserving coupling of isogeometric rotation-free shell patches. The NURBS patches used are end-point interpolatory thus providing only  $C^0$ -continuity at the coupling interface.

---

<sup>1</sup>This chapter is based on the paper “Y. Guo, M. Ruess, Nitsche’s method for a coupling of isogeometric thin shells and blended shell structures, *Computer Methods in Applied Mechanics and Engineering*, 284, 881-905, 2015”

<sup>2</sup>This chapter is based on the paper “Y. Guo, M. Ruess, Weak Dirichlet boundary conditions for trimmed thin isogeometric shells, *Computers and Mathematics with Applications*, 70, 1425–1440, 2015”

A proper transfer of bending moments requires  $G^1$ -continuity among the coupled patches which cannot be ensured by the use of  $C^0$ -continuous functions without further model enrichment [216]. Furthermore, the inherent trimming problem adds to the difficulty of achieving accurate and reliable enforcement of both the continuity-preserving coupling constraints and the essential boundary conditions.

In this chapter we use a stabilized weak approach to enforce both essential boundary conditions and multi-patch coupling constraints of rotation-free Kirchhoff-Love shell patches including trimmed domains, non-conforming discretizations and overlapping patches.

This chapter is organized as follows: a concise summary of the Kirchhoff-Love theory for thin shells is presented in section 5.1 followed by an extension of the principle of virtual work in sections 5.2 and 5.3 to handle essential boundary conditions and coupling constraints, respectively, in a weak, integral sense. The performance of the developed extensions is documented with various test examples in sections 5.4 and 5.5. Conclusions for this chapter are drawn in section 5.6.

## 5.1 Isogeometric rotation-free Kirchhoff-Love shells

In the following, the fundamentals of a rotation-free Kirchhoff-Love shell [2] formulation are presented in compact form. Again, the upper case and lower case notations refer to the undeformed and current configurations, respectively. The geometric description of the Kirchhoff-Love shell follows the definitions introduced in chapter 3, cf. equation 3.3. The definitions of co- and contravariant bases are given in chapters 2 and chapter 3.

Based on the assumptions of Kirchhoff-Love [142, 154] the 3D strain tensor  $\mathbf{E}$  (2.20) reduces to the in-plane strain components:

$$\mathbf{E} = E_{\alpha\beta} \mathbf{G}^\alpha \otimes \mathbf{G}^\beta, \quad \alpha, \beta = \{1, 2\} \quad (5.1)$$

$$E_{\alpha\beta} = \frac{1}{2} (g_{\alpha\beta} - G_{\alpha\beta}) \quad (5.2)$$

referring to the contravariant base vectors  $\mathbf{G}^\alpha$  ( $\alpha = 1, 2$ ) of the undeformed configuration. Correspondingly  $\mathbf{g}^\alpha$  ( $\alpha = 1, 2$ ) denote the contravariant base vectors of the deformed configuration. The strain tensor (5.1) is further split into in-plane and out-of-plane contributions:

$$E_{\alpha\beta} = \varepsilon_{\alpha\beta} + \xi_3 t \kappa_{\alpha\beta} \quad (5.3)$$

with  $\varepsilon_{\alpha\beta}$  representing membrane and  $(\xi_3 t \kappa_{\alpha\beta})$  representing the bending effects independently. The membrane strains are given by:

$$\varepsilon_{\alpha\beta} = \frac{1}{2} (\mathbf{a}_{\alpha\beta} - \mathbf{A}_{\alpha\beta}) \quad (5.4)$$

$$\mathbf{a}_{\alpha\beta} = \mathbf{a}_\alpha \cdot \mathbf{a}_\beta \quad (5.5)$$

$$\mathbf{A}_{\alpha\beta} = \mathbf{A}_\alpha \cdot \mathbf{A}_\beta \quad (5.6)$$

The bending strains are defined as:

$$\kappa_{\alpha\beta} = B_{\alpha\beta} - b_{\alpha\beta} \quad (5.7)$$

$$b_{\alpha\beta} = \mathbf{a}_{\alpha,\beta} \cdot \mathbf{a}_3 \quad (5.8)$$

$$B_{\alpha\beta} = \mathbf{A}_{\alpha,\beta} \cdot \mathbf{A}_3 \quad (5.9)$$

where  $\mathbf{a}_i$  and  $\mathbf{A}_i$  ( $i = 1, 2, 3$ ) denote the basis at location  $\mathbf{r}$  and  $\mathbf{R}$ , respectively and where  $\mathbf{a}_3$  and  $\mathbf{A}_3$  are the unit normal vector of mid-surface in the deformed and undeformed configurations, respectively, cf. Figure 5.1, and where  $\kappa_{\alpha\beta}$  represents the curvature of the shell mid-surface.

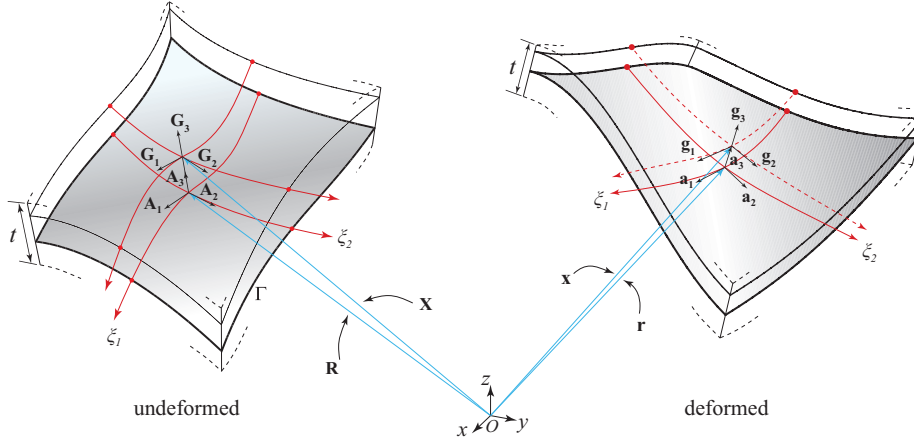


Figure 5.1: Shell geometry description in undeformed and deformed configurations.

The strain relations are defined in the contravariant basis and a transformation to the local Cartesian coordinate system is needed to apply the constitutive equations. The local Cartesian basis of a shell body is specified with the basis vectors:

$$\mathbf{e}_1 = \frac{\mathbf{G}_1}{|\mathbf{G}_1|} \quad (5.10)$$

$$\mathbf{e}_2 = \frac{\mathbf{G}_2 - (\mathbf{G}_2 \cdot \mathbf{e}_1)\mathbf{e}_1}{|\mathbf{G}_2 - (\mathbf{G}_2 \cdot \mathbf{e}_1)\mathbf{e}_1|} \quad (5.11)$$

$$\mathbf{e}_3 = \mathbf{A}_3 \quad (5.12)$$

With (5.10) to (5.12) the strain tensor in the local coordinate system follows as:

$$\bar{\mathbf{E}}_{\gamma\delta} = E_{\alpha\beta}(\mathbf{e}_\gamma \cdot \mathbf{G}^\alpha)(\mathbf{G}^\beta \cdot \mathbf{e}_\delta), \quad \gamma, \delta = 1, 2 \quad (5.13)$$

containing only in-plane strain components.

The relation between stresses and strains is established with the constitutive equations in Voigt notation:

$$\begin{bmatrix} \bar{S}^{11} \\ \bar{S}^{22} \\ \bar{S}^{12} \end{bmatrix} = \hat{\mathbf{C}} \begin{bmatrix} \bar{E}_{11} \\ \bar{E}_{22} \\ 2\bar{E}_{12} \end{bmatrix} \quad (5.14)$$

where  $S^{\alpha\beta}$  denotes the stress tensor coefficients and  $\hat{\mathbf{C}}$  is the reduced material matrix for plane stress problems [154]. Integration of the stress components over the shell thickness provides the force and moment stress resultants  $\bar{\mathbf{n}}$  and  $\bar{\mathbf{m}}$ , respectively, written in Voigt notation as:

$$\begin{bmatrix} \bar{n}^{11} \\ \bar{n}^{22} \\ \bar{n}^{12} \end{bmatrix} = t \cdot \hat{\mathbf{C}} \begin{bmatrix} \bar{\varepsilon}_{11} \\ \bar{\varepsilon}_{22} \\ 2\bar{\varepsilon}_{12} \end{bmatrix} \quad (5.15)$$

$$\begin{bmatrix} \bar{m}^{11} \\ \bar{m}^{22} \\ \bar{m}^{12} \end{bmatrix} = \frac{t^3}{12} \cdot \hat{\mathbf{C}} \begin{bmatrix} \bar{\kappa}_{11} \\ \bar{\kappa}_{22} \\ 2\bar{\kappa}_{12} \end{bmatrix} \quad (5.16)$$

In this thesis, laminate composite shells are modeled according to the classical lamination theory [154] which specifies the through-thickness homogenized elasticity properties with three matrices  $\mathbf{A}$ ,  $\mathbf{B}$ ,  $\mathbf{D}$ :

$$\mathbf{A} = \frac{t}{n} \sum_{k=1}^n \hat{\mathbf{C}}_k^{ortho} \quad (5.17)$$

$$\mathbf{B} = \frac{t^2}{n^2} \sum_{k=1}^n \hat{\mathbf{C}}_k^{ortho} \left( k - \frac{n+1}{2} \right) \quad (5.18)$$

$$\mathbf{D} = \frac{t^3}{n^3} \sum_{k=1}^n \hat{\mathbf{C}}_k^{ortho} \left[ \left( k - \frac{n+1}{2} \right)^2 + \frac{1}{12} \right] \quad (5.19)$$

where  $n$  is the number of layers and where the material matrix  $\hat{\mathbf{C}}_k^{ortho}$  is defined in the local Cartesian reference coordinate system, representing orthotropic material behavior. The matrices  $\mathbf{A}$  and  $\mathbf{D}$  represent the extensional and bending stiffness matrices, respectively, and the  $\mathbf{B}$  matrix represents the coupling of membrane and bending actions and vanishes for symmetric stacking sequences. The membrane forces and bending moments of the laminates are obtained as:

$$\begin{bmatrix} \bar{n}^{11} \\ \bar{n}^{22} \\ \bar{n}^{12} \end{bmatrix} = \mathbf{A} \cdot \begin{bmatrix} \bar{\varepsilon}_{11} \\ \bar{\varepsilon}_{22} \\ 2\bar{\varepsilon}_{12} \end{bmatrix} + \mathbf{B} \cdot \begin{bmatrix} \bar{\kappa}_{11} \\ \bar{\kappa}_{22} \\ 2\bar{\kappa}_{12} \end{bmatrix} \quad (5.20)$$

$$\begin{bmatrix} \bar{m}^{11} \\ \bar{m}^{22} \\ \bar{m}^{12} \end{bmatrix} = \mathbf{B} \cdot \begin{bmatrix} \bar{\varepsilon}_{11} \\ \bar{\varepsilon}_{22} \\ 2\bar{\varepsilon}_{12} \end{bmatrix} + \mathbf{D} \cdot \begin{bmatrix} \bar{\kappa}_{11} \\ \bar{\kappa}_{22} \\ 2\bar{\kappa}_{12} \end{bmatrix} \quad (5.21)$$

### 5.1.1 Governing equations and isogeometric discretizations

Using the principle of virtual work, we obtain a variational form of the elasticity problem satisfying the equilibrium:

$$\mathcal{W}(\mathbf{u}, \delta \mathbf{u}) = \mathcal{W}_I(\mathbf{u}, \delta \mathbf{u}) + \mathcal{W}_E(\mathbf{u}, \delta \mathbf{u}) = \mathbf{0} \quad (5.22)$$

with the internal and external work integrals:

$$\mathcal{W}_I(\mathbf{u}, \delta \mathbf{u}) = - \int_{\Omega} (\mathbf{n} : \delta \boldsymbol{\varepsilon} + \mathbf{m} : \delta \boldsymbol{\kappa}) dA \quad (5.23)$$

$$\mathcal{W}_E(\mathbf{u}, \delta \mathbf{u}) = \int_{\Omega} \mathbf{p} \cdot \delta \mathbf{u} dA + \int_{\Gamma_t} \mathbf{t}_0 \cdot \delta \mathbf{u} dS \quad (5.24)$$

where  $dA$  denotes a differential element of the mid-surface area of the shell domain and where correspondingly  $dS$  denotes a differential element of the domain boundary and where  $\delta \mathbf{u}$ ,  $\delta \boldsymbol{\varepsilon}$  and  $\delta \boldsymbol{\kappa}$  denotes the variation of displacements and strains, respectively. Vector  $\mathbf{t}_0$  denotes the traction per unit length along the Neumann boundary  $\Gamma_t$  and  $\mathbf{p}$  is the domain load per unit area on the mid-surface. At this position we assume the boundary conditions,  $\mathbf{u} = \mathbf{u}_0$ , along the Dirichlet boundary  $\Gamma_u$  to be satisfied in a strong sense by the choice of adequate interpolation functions. A more flexible weak enforcement is introduced and discussed in the following sub-section 5.2.

Following the concept of isogeometric analysis, the geometry and displacement field of the mid-surface are discretized with the same NURBS basis functions as:

$$\mathbf{u} = \sum_i R_i \mathbf{U}_i \quad (5.25)$$

where  $\mathbf{U}_i$  denotes the unknowns in terms of mid-surface control point displacements.

The first and second derivatives of the virtual work integrals with respect to the introduced unknown displacement components of (5.25) provide the residual forces and the shell stiffness, respectively:

$$\mathbf{R} = \left( \frac{\partial \mathcal{W}_I}{\partial \mathbf{U}_r} + \frac{\partial \mathcal{W}_E}{\partial \mathbf{U}_r} \right) = \mathbf{f}_I + \mathbf{f}_E \quad (5.26)$$

$$\mathbf{K} = - \left( \frac{\partial^2 \mathcal{W}_I}{\partial \mathbf{U}_r \partial \mathbf{U}_s} + \frac{\partial^2 \mathcal{W}_E}{\partial \mathbf{U}_r \partial \mathbf{U}_s} \right) = \mathbf{K}_I + \mathbf{K}_E \quad (5.27)$$

where

$$\mathbf{f}_I = - \int_{\Omega} \left( \mathbf{n} : \frac{\partial \boldsymbol{\varepsilon}}{\partial \mathbf{U}_r} + \mathbf{m} : \frac{\partial \boldsymbol{\kappa}}{\partial \mathbf{U}_r} \right) dA \quad (5.28)$$

$$\mathbf{f}_E = \int_{\Omega} \mathbf{p} \cdot \frac{\partial \mathbf{u}}{\partial \mathbf{U}_r} dA + \int_{\Gamma_t} \mathbf{t}_0 \cdot \frac{\partial \mathbf{u}}{\partial \mathbf{U}_r} dS \quad (5.29)$$

and

$$\mathbf{K}_I = \int_{\Omega} \left( \frac{\partial \mathbf{n}}{\partial \mathbf{U}_s} : \frac{\partial \boldsymbol{\varepsilon}}{\partial \mathbf{U}_r} + \mathbf{n} : \frac{\partial^2 \boldsymbol{\varepsilon}}{\partial \mathbf{U}_r \partial \mathbf{U}_s} + \frac{\partial \mathbf{m}}{\partial \mathbf{U}_s} : \frac{\partial \boldsymbol{\kappa}}{\partial \mathbf{U}_r} + \mathbf{m} : \frac{\partial^2 \boldsymbol{\kappa}}{\partial \mathbf{U}_r \partial \mathbf{U}_s} \right) dA \quad (5.30)$$

$$\mathbf{K}_E = \int_{\Omega} \frac{\partial \mathbf{p}}{\partial \mathbf{U}_s} \cdot \frac{\partial \mathbf{u}}{\partial \mathbf{U}_r} dA + \int_{\Gamma_t} \frac{\partial \mathbf{t}_0}{\partial \mathbf{U}_s} \cdot \frac{\partial \mathbf{u}}{\partial \mathbf{U}_r} dS \quad (5.31)$$

The external work contribution  $\mathbf{K}_E$  is associated with the displacement-dependent load and can be neglected when the load is constant. The partial derivatives of  $\boldsymbol{\varepsilon}$ ,  $\boldsymbol{\kappa}$ ,  $\mathbf{n}$  and  $\mathbf{m}$  with respect to the displacement variables  $\mathbf{U}_r$  and  $\mathbf{U}_s$ , respectively, is provided in Appendix A.

Confining our discussion to linear elastostatics, the linear stiffness matrix reads:

$$\mathbf{K} = \int_{\Omega} \left( \frac{\partial \mathbf{n}}{\partial \mathbf{U}_s} : \frac{\partial \boldsymbol{\varepsilon}}{\partial \mathbf{U}_r} + \frac{\partial \mathbf{m}}{\partial \mathbf{U}_s} : \frac{\partial \boldsymbol{\kappa}}{\partial \mathbf{U}_r} \right) dA \quad (5.32)$$

The area element  $dA$  is calculated using:

$$dA = \sqrt{|A_{\alpha\beta}|} d\xi_1 d\xi_2 \quad (5.33)$$

The differential boundary element  $dS$  in (5.24) is found accordingly as the line increment.

## 5.2 Weakly enforced essential boundary conditions

The essential boundary conditions of the isogeometric Kirchhoff-Love shell are expressed in terms of mid-surface displacements  $\mathbf{u}$  and rotations  $\boldsymbol{\Phi}$ , respectively:

$$\mathbf{u} - \mathbf{u}_0 = \mathbf{0} \quad \mathbf{x} \in \Gamma_u \quad (5.34)$$

$$\boldsymbol{\Phi} - \boldsymbol{\Phi}_0 = \mathbf{0} \quad \mathbf{x} \in \Gamma_{\theta} \quad (5.35)$$

where a subscript 0 denotes prescribed values, and where  $\boldsymbol{\Phi} = \mathbf{a}_3 - \mathbf{A}_3$  denotes the angle between the deformed and the undeformed shell configuration. The domain boundaries  $\Gamma_u$  and  $\Gamma_{\theta}$  denote the Dirichlet boundary of prescribed essential boundary conditions. The total domain boundary  $\Gamma$  follows by unification with the Neumann boundary  $\Gamma_t$  of prescribed natural boundary conditions such that  $\Gamma = \Gamma_u \cup \Gamma_{\theta} \cup \Gamma_t$  and  $(\Gamma_u \cup \Gamma_{\theta}) \cap \Gamma_t = \emptyset$ .

### 5.2.1 Governing equations of the Nitsche extension

The basic idea of NITSCHÉ [101] originally referred to the enforcement of essential boundary conditions for the Poisson problem. The weak form (5.22) is extended

variationally consistent considering flux terms along the Dirichlet boundary which naturally derived from a weighted residual formulation satisfying the displacement and rotational boundary conditions in an integral sense. Stabilization terms are added to ensure the ellipticity of the original problem [217, 103]. The enforcement of essential boundary conditions for solid elements in the framework of isogeometric analysis is elaborately presented in [104]. For a detailed discussion of the consistent derivation of the principle of virtual work which reveals the consistency terms presented in the following we refer the reader to [218, 219].

Considering the Nitsche extension the equilibrium follows as:

$$\mathcal{W}_E(\mathbf{u}, \delta \mathbf{u}) + \mathcal{W}_I(\mathbf{u}, \delta \mathbf{u}) - \mathcal{W}^{NIT}(\mathbf{u}, \delta \mathbf{u}) = \mathbf{0} \quad (5.36)$$

where  $\mathcal{W}^{NIT}(\mathbf{u}, \delta \mathbf{u})$  represents the work contributions of the Nitsche extension and the corresponding stabilization terms.

In the following we split the Nitsche work expression into an internal and external work contribution. For the internal work contribution follows:

$$\begin{aligned} \mathcal{W}_I^{NIT} = & - \int_{\Gamma_u} \delta (N^\alpha + b_\gamma^\alpha M^\gamma) \cdot u_{(\alpha)} dS - \int_{\Gamma_u} (N^\alpha + b_\gamma^\alpha M^\gamma) \cdot \delta u_{(\alpha)} dS \\ & - \int_{\Gamma_u} \delta (Q + M_{(d),s}) \cdot u_{(3)} dS - \int_{\Gamma_u} (Q + M_{(d),s}) \cdot \delta u_{(3)} dS \\ & - \int_{\Gamma_\theta} \delta M_{(t)} \cdot \Phi_{(d)} dS - \int_{\Gamma_\theta} M_{(t)} \cdot \delta \Phi_{(d)} dS \\ & + \int_{\Gamma_u} \tau_S \delta \mathbf{u} \cdot \mathbf{u} dS + \int_{\Gamma_\theta} \tau_S \frac{t^2}{12} \delta \Phi \cdot \Phi dS \\ & + \int_{\Gamma_u} \tau_N (\mathbf{d} \cdot \delta \mathbf{u}) (\mathbf{u} \cdot \mathbf{d}) dS + \int_{\Gamma_\theta} \tau_N \frac{t^2}{12} (\mathbf{d} \cdot \delta \Phi) (\Phi \cdot \mathbf{d}) dS \end{aligned} \quad (5.37)$$

where the first six terms in (5.37) are the Nitsche-based consistency terms, where the last four terms are stabilization terms, and where  $\mathbf{d}$  is the in-plane normal vector along the boundary  $\Gamma$ , cf. Figure 2.12(a), which is perpendicular to the normal vector  $\mathbf{a}_3$  of the shell surface, where  $dS$  denotes a differential line element of the mid-surface shell boundary and where the term  $(\Phi_{(d)} = \Phi \cdot \mathbf{d})$  denotes the rotation along the normal direction of the boundary. Further, the term  $(N^\alpha + b_\gamma^\alpha M^\gamma)$  is the effective membrane force, where  $(Q + M_{(d),s})$  is the effective shear force and where  $(M_{(t)})$  is the bending moment in direction of the boundary normal  $\mathbf{d}$  with:

$$N^\alpha + b_\gamma^\alpha M^\gamma = (n^{\beta\alpha} + 2 b_\gamma^\alpha m^{\beta\gamma}) d_\beta \quad (5.38)$$

$$Q = m^{\alpha\beta} |_\alpha d_\beta \quad (5.39)$$

$$M_{(d),s} = (m^{\alpha\beta} d_\alpha t_\beta)_{,s} \quad (5.40)$$

$$M_{(t)} = m^{\alpha\beta} d_\alpha d_\beta \quad (5.41)$$

and

$$\mathbf{u} = u_{(\alpha)} \mathbf{a}^\alpha + u_{(3)} \mathbf{a}_3 \quad (5.42)$$

$$u_{(\alpha)} = \mathbf{u} \cdot \mathbf{a}_\alpha \quad (5.43)$$

$$u_{(3)} = \mathbf{u} \cdot \mathbf{a}_3 \quad (5.44)$$

where the stress resultants  $n^{\alpha\beta}$  and bending moments  $m^{\alpha\beta}$  refer to the covariant basis, and where  $(u_{(\alpha)}, u_{(3)})$  represent the covariant displacement components expressed in the contravariant basis, where  $d_\alpha, t_\alpha$  are the covariant components of the normal and tangent vector of the boundary  $\Gamma$ , and where  $\mathbf{a}_3 = \mathbf{a}^3$ . The term  $b_\gamma^\alpha$  in (5.38) represents the mixed components of surface's second fundamental form which is expressed as:

$$b_\gamma^\alpha = a^{\alpha\beta} b_{\gamma\beta} \quad (5.45)$$

Equation (5.39) represents the shear force where the vertical stroke before the subscript  $\alpha$  denotes the covariant surface differentiation with respect to the curvilinear coordinate  $\xi_\alpha$ . The covariant derivatives of tensor and vector fields, respectively, are expressed as:

$$m^{\alpha\beta}|_\gamma = m_{,\gamma}^{\alpha\beta} + \Gamma_{\lambda\gamma}^\alpha m^{\lambda\beta} + \Gamma_{\lambda\gamma}^\beta m^{\alpha\lambda} \quad (5.46)$$

$$t_{\alpha|\beta} = t_{\alpha,\beta} - \Gamma_{\alpha\beta}^\lambda t_\lambda \quad (5.47)$$

where  $\Gamma_{\alpha\beta}^\lambda$  is the Christoffel symbol on a surface. For more details about equations (5.38)-(5.47) we refer the reader to [220, 221]. Equation (5.40) represents the derivatives of the twisting moment along the boundary, together with (5.39), they represent the effective shear force. The subscript  $(\cdot)_{,s}$  denotes the derivatives with respect to the arc length along the boundary. Equation (5.40) can be further expressed as:

$$(m^{\alpha\beta} d_\alpha t_\beta)_{,s} = (m^{\alpha\beta} d_\alpha t_\beta)_{,\gamma} t^\gamma \quad (5.48)$$

where the derivatives of the twisting moment with respect to the curvilinear coordinates is written as:

$$(m^{\alpha\beta} d_\alpha t_\beta)_{,\gamma} = m^{\alpha\beta}|_\gamma d_\alpha t_\beta + m^{\alpha\beta} d_{\alpha|\gamma} t_\beta + m^{\alpha\beta} d_\alpha t_{\beta|\gamma} \quad (5.49)$$

The first six consistency terms in (5.37) refer to the general form for linear Kirchhoff-Love shell models. For shallow shell or plate models some of the terms simplify or even vanish. For plates, equation (5.37) further simplifies since the out-of-plane curvature is equal to zero. The stabilized terms presented in equations (5.37) and (5.50) correspond to fully involved boundary conditions where both, displacements and rotations in all directions, are constrained. For partial constraints considering only part of the displacements or rotations, terms are dropped, correspondingly.

The external work integral of the Nitsche contribution is:

$$\begin{aligned}
 \mathcal{W}_E^{NIT} &= - \int_{\Gamma_u} \delta (N^\alpha + b_\gamma^\alpha M^\gamma) \cdot u_{0(\alpha)} dS - \int_{\Gamma_u} \delta (Q + M_{(d),s}) \cdot u_{0(3)} dS \\
 &\quad - \int_{\Gamma_\theta} \delta M_{(t)} \cdot \Phi_{0(d)} dS \\
 &\quad + \int_{\Gamma_u} \tau_S \delta \mathbf{u} \cdot \mathbf{u}_0 dS + \int_{\Gamma_\theta} \tau_S \frac{t^2}{12} \delta \Phi \cdot \Phi_0 dS \\
 &\quad + \int_{\Gamma_u} \tau_N (\mathbf{d} \cdot \delta \mathbf{u}) (\mathbf{u}_0 \cdot \mathbf{d}) dS + \int_{\Gamma_\theta} \tau_N \frac{t^2}{12} (\mathbf{d} \cdot \delta \Phi) (\Phi_0 \cdot \mathbf{d}) dS
 \end{aligned} \tag{5.50}$$

in which  $\mathbf{u}_0 = \{u_{0(\alpha)}, u_{0(3)}\}$  and  $\Phi_0 = \{\Phi_{0(t)}, \Phi_{0(d)}, 0\}$  represent the prescribed displacements and rotations along the Dirichlet boundary. The extensions (5.37) and (5.50) used in our framework applies two terms for stabilization. Without stabilization the formulation remains variationally consistent but coercivity is lost, i.e. the system stiffness matrix becomes singular [96]. A penalty-like stabilization with a free parameter  $\tau_S$  is used to counteract the singular system of equations. In [104, 113] the use of an additional stability term with a free parameter  $\tau_N$ , acting towards the normal part of the interface traction, is motivated from an expansion of the constitutive relation.

For optimal convergence properties we choose  $\tau_S$  and  $\tau_N$  proportional to the material properties, here the Lamé constants  $\lambda$  and  $\nu$  and inversely proportional to the element diameter  $h$ . Two remaining constants  $C_S$  and  $C_N$ , respectively, are influenced by the polynomial degree of the applied approximation space [222, 217]:

$$\tau_S = C_S(p) \frac{\nu}{h} \tag{5.51}$$

$$\tau_N = C_N(p) \frac{\lambda}{h} \tag{5.52}$$

Sufficiently large values for  $C_S$  and  $C_N$  ensure non-singularity of the governing equations and the aspired positive definiteness of the corresponding coefficient matrix.

The constants  $C_S$  and  $C_N$  can be bounded explicitly by the consideration of discrete trace inequalities [223]. Alternatively, reliable values can be determined self-controlled by the partial solution of an eigenvalue problem for the largest eigenvalue which gives a suitable value for a stable computation scheme [104, 113]. In [113] it was shown that optimal choices for  $C_S$  and  $C_N$ , optimal in terms of optimal convergence properties, exist. Beside this optimal values a wide range of values can be chosen empirically without significantly compromising the accuracy of the solution which is the preferred approach pursued in the following examples. For the moderate polynomial values used in the examples of section 5.4 and section 5.5 these values are typically of order  $\mathcal{O}(1)$ .

## 5.2.2 Discretization aspects

The internal work integrals (5.37) and (5.50) of the Nitsche extension contribute to the stiffness matrix and load vector of the governing system of equations, respectively. Following the discretization of the elastic shell in section 5.1.1, the additional stiffness and load contributions of the Nitsche terms extend the algebraic equations:

$$(K_{rs}^{INT} - K_{rs}^{NIT} - K_{sr}^{NIT} + K_{rs}^{STB}) u_r = f_r^{EXT} - f_r^{NIT} + f_r^{STB} \quad (5.53)$$

where  $(K_{rs}^{INT} u_r)$  and  $f_r^{EXT}$  denote the internal elastic and external forces of the standard shell problem. The matrix  $K_{rs}^{NIT}$ , its transpose  $K_{sr}^{NIT}$  and the vector  $f_r^{NIT}$  refer to the stiffness and load contributions of the consistency terms, respectively. The quantities  $K_{rs}^{STB}$  and  $f_r^{STB}$  are the contributions used to stabilize the formulation. Both the total number of equations and the symmetry properties are retained by the additional contributions. The matrix and vector coefficients of the discrete equations follow from the partial derivatives of equations (5.37) and (5.50) with respect to the displacement degrees of freedom in analogy to (5.30).

The discretized form of the consistency and stabilization terms of equations (5.37) follow as:

$$\begin{aligned} K_{rs}^{NIT} &= \int_{\Gamma_u} \frac{\partial (N^\alpha + b_\gamma^\alpha M^\gamma)}{\partial \mathbf{U}_r} \cdot \frac{\partial u_{(\alpha)}}{\partial \mathbf{U}_s} dS + \int_{\Gamma_u} \frac{\partial (Q + M_{(\nu),s})}{\partial \mathbf{U}_r} \cdot \frac{\partial u_{(3)}}{\partial \mathbf{U}_s} dS \\ &+ \int_{\Gamma_\theta} \frac{\partial M_{(t)}}{\partial \mathbf{U}_r} \cdot \frac{\partial \Phi_{(\nu)}}{\partial \mathbf{U}_s} dS \end{aligned} \quad (5.54)$$

$$\begin{aligned} K_{rs}^{STB} &= \int_{\Gamma_u} \tau_S \frac{\partial \mathbf{u}}{\partial \mathbf{U}_r} \cdot \frac{\partial \mathbf{u}}{\partial \mathbf{U}_s} dS + \int_{\Gamma_\theta} \tau_S \frac{t^2}{12} \frac{\partial \Phi}{\partial \mathbf{U}_r} \cdot \frac{\partial \Phi}{\partial \mathbf{U}_s} dS \\ &+ \int_{\Gamma_u} \tau_N (\mathbf{d} \cdot \frac{\partial \mathbf{u}}{\partial \mathbf{U}_r}) (\frac{\partial \mathbf{u}}{\partial \mathbf{U}_s} \cdot \mathbf{d}) dS + \int_{\Gamma_\theta} \tau_N \frac{t^2}{12} (\mathbf{d} \cdot \frac{\partial \Phi}{\partial \mathbf{U}_r}) (\frac{\partial \Phi}{\partial \mathbf{U}_s} \cdot \mathbf{d}) dS \end{aligned} \quad (5.55)$$

The transposed consistency term  $K_{sr}^{NIT}$  follows in analogy to (5.54).

The vector contributions of the consistency and stability terms of the Nitsche extension are computed according to:

$$\begin{aligned} f_r^{NIT} &= \int_{\Gamma_u} \frac{\partial (N^\alpha + b_\gamma^\alpha M^\gamma)}{\partial \mathbf{U}_r} \cdot u_{0(\alpha)} dS + \int_{\Gamma_u} \frac{\partial (Q + M_{(d),s})}{\partial \mathbf{U}_r} \cdot u_{0(3)} dS \\ &+ \int_{\Gamma_\theta} \frac{\partial M_{(t)}}{\partial \mathbf{U}_r} \cdot \Phi_{0(d)} dS \end{aligned} \quad (5.56)$$

$$\begin{aligned} f_r^{STB} &= \int_{\Gamma_u} \tau_S \frac{\partial \mathbf{u}}{\partial \mathbf{U}_r} \cdot \mathbf{u}_0 dS + \int_{\Gamma_\theta} \tau_S \frac{t^2}{12} \frac{\partial \Phi}{\partial \mathbf{U}_r} \cdot \Phi_0 dS \\ &+ \int_{\Gamma_u} \tau_N (\mathbf{d} \cdot \frac{\partial \mathbf{u}}{\partial \mathbf{U}_r}) (\mathbf{u}_0 \cdot \mathbf{d}) dS + \int_{\Gamma_\theta} \tau_N \frac{t^2}{12} (\mathbf{d} \cdot \frac{\partial \Phi}{\partial \mathbf{U}_r}) (\Phi_0 \cdot \mathbf{d}) dS \end{aligned} \quad (5.57)$$

where the partial derivatives with respect to  $\mathbf{U}_r$  follow from linearization at  $\mathbf{u} = \mathbf{0}$ :

$$\left. \frac{\partial (N^\alpha + b_\gamma^\alpha M^\gamma)}{\partial \mathbf{U}_r} \right|_{\mathbf{u}=\mathbf{0}} = (n_{,r}^{\beta\alpha} + 2 b_\gamma^\alpha m_{,r}^{\beta\gamma}) d_\beta \quad (5.58)$$

$$\left. \frac{\partial M_{(d),s}}{\partial \mathbf{U}_r} \right|_{\mathbf{u}=\mathbf{0}} = \left( (m^{\alpha\beta}|_\gamma)_{,r} d_\alpha t_\beta + m_{,r}^{\alpha\beta} d_{\alpha|\gamma} t_\beta + m_{,r}^{\alpha\beta} d_\alpha t_{\beta|\gamma} \right) t^\gamma \quad (5.59)$$

$$\left. \frac{\partial Q}{\partial \mathbf{U}_r} \right|_{\mathbf{u}=\mathbf{0}} = \left( (m_{,\alpha}^{\alpha\beta})_{,r} + \Gamma_{\lambda\alpha}^\alpha m_{,r}^{\lambda\beta} + \Gamma_{\lambda\alpha}^\beta m_{,r}^{\alpha\lambda} \right) d_\beta \quad (5.60)$$

$$\left. \frac{\partial M_{(t)}}{\partial \mathbf{U}_r} \right|_{\mathbf{u}=\mathbf{0}} = m_{,r}^{\alpha\beta} d_\alpha d_\beta \quad (5.61)$$

The derivatives and covariant derivatives of the stress resultants  $n^{\alpha\beta}$ , the bending moments  $m^{\alpha\beta}$  can be found in Appendix A. The covariant derivatives of the normal and tangential vector components  $d_\alpha$  and  $t_\alpha$  for boundary fitted NURBS shell patches can be first expanded according to equation (5.47). Then, the derivatives  $d_{\alpha,\gamma}$  and  $t_{\alpha,\gamma}$  follow the same way as the derivatives of surface normal vector  $\mathbf{a}_3$ . This issue is revisited and discussed in section 5.2.3 for trimmed NURBS boundaries. The derivatives are evaluated coefficient-wise and will assemble to a strain interpolation matrix with three columns representing  $n_{dof}$  contributions according to in-plane forces in directions  $(\alpha_1, \alpha_2)$  and according to shear forces in direction of the normal  $\mathbf{a}_3$ , with  $n_{dof}$  being the number of discrete element equations.

### 5.2.3 Treatment of trimmed boundaries

In general, the trimming curves  $\mathcal{C}(\theta)$  and the trimmed surface  $\mathbf{x}(\xi, \eta)$  have independent parameterizations  $(\theta)$  and  $(\xi, \eta)$  for which, in general, no simple analytical relation can be found. As a consequence, special attention must be given to the derivatives of the normal and tangent vector  $\mathbf{d}$  and  $\mathbf{t}$ , respectively, along the domain boundary. These derivatives are required when essential boundary conditions are satisfied weakly with the proposed Nitsche approach (5.37)-(5.50).

The covariant derivatives of  $d_{\alpha|\gamma}$  and  $t_{\beta|\gamma}$  used in (5.59) can be expressed as:

$$d_{\alpha|\gamma} = d_{\alpha,\gamma} - \Gamma_{\alpha\gamma}^\lambda d_\lambda \quad (5.62)$$

$$t_{\beta|\gamma} = t_{\beta,\gamma} - \Gamma_{\beta\gamma}^\lambda t_\lambda \quad (5.63)$$

where  $d_\lambda$  and  $t_\lambda$  can be computed based on the trimming curve  $\mathcal{C}(\theta)$  and the base vectors of the underlying shell surface  $\mathbf{x}(\xi, \eta)$  and where the derivatives  $d_{\alpha,\gamma}$  and  $t_{\beta,\gamma}$  are:

$$d_{\alpha,\gamma} = (\mathbf{d} \cdot \mathbf{A}_\alpha)_{,\gamma} = \mathbf{d}_{,\gamma} \cdot \mathbf{A}_\alpha + \mathbf{d} \cdot \mathbf{A}_{\alpha,\gamma} \quad (5.64)$$

$$t_{\beta,\gamma} = (\mathbf{t} \cdot \mathbf{A}_\beta)_{,\gamma} = \mathbf{t}_{,\gamma} \cdot \mathbf{A}_\beta + \mathbf{t} \cdot \mathbf{A}_{\beta,\gamma} \quad (5.65)$$

with

$$\hat{\mathbf{t}} = \left( \frac{\partial \mathcal{C}}{\partial \theta} \right) \quad (5.66)$$

$$\hat{\mathbf{t}}_{,\gamma} = \left( \frac{\partial \mathcal{C}}{\partial \theta} \right)_{,\gamma} = \frac{\partial^2 \mathcal{C}}{\partial \theta^2} \frac{\partial \theta}{\partial \gamma} \quad (5.67)$$

and where

$$\frac{\partial \theta}{\partial \gamma} = \frac{1}{\hat{\mathbf{t}} \cdot \mathbf{A}^\gamma} \quad (5.68)$$

We use a hat symbol to indicate that the tangential and normal vectors used in (5.66)-(5.70) are no longer of unit length and require normalization to be used in (5.64) and (5.65).

The normal vector along the trimmed boundary is constructed as:

$$\hat{\mathbf{d}} = \hat{\mathbf{t}} \times \mathbf{A}_3 = \mathbf{A}_1(\hat{\mathbf{t}} \cdot \mathbf{A}_2) - \mathbf{A}_2(\hat{\mathbf{t}} \cdot \mathbf{A}_1) \quad (5.69)$$

with the derivative

$$\begin{aligned} \hat{\mathbf{d}}_{,\gamma} &= \mathbf{A}_{1,\gamma}(\hat{\mathbf{t}} \cdot \mathbf{A}_2) + \mathbf{A}_1(\hat{\mathbf{t}}_{,\gamma} \cdot \mathbf{A}_2 + \hat{\mathbf{t}} \cdot \mathbf{A}_{2,\gamma}) \\ &\quad - \mathbf{A}_{2,\gamma}(\hat{\mathbf{t}} \cdot \mathbf{A}_1) - \mathbf{A}_2(\hat{\mathbf{t}}_{,\gamma} \cdot \mathbf{A}_1 + \hat{\mathbf{t}} \cdot \mathbf{A}_{1,\gamma}) \end{aligned} \quad (5.70)$$

### 5.3 Weakly enforced coupling constraints

Following the Nitsche extension for the weak enforcement of essential boundary conditions a modified formulation can be obtained to enforce coupling constraints between patches. The extension to a weak coupling method becomes straightforward when considering the interface of the coupled domains to be mutually influencing boundaries [113], cf. Figure 5.2. The displacement continuity and force compatibility

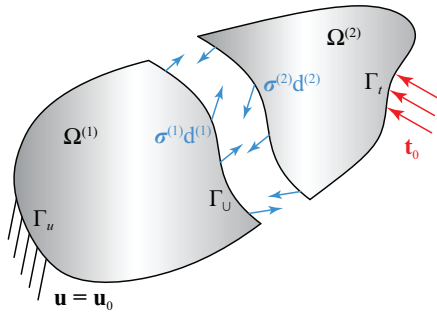


Figure 5.2: Computational domain of multiple patches.

conditions at the coupling interface of the two mutually influencing domains are:

$$\mathbf{u}^{(1)} - \mathbf{u}^{(2)} = \mathbf{0} \quad \text{on } \Gamma_{\cup} \quad (5.71)$$

$$\boldsymbol{\sigma}^{(1)} \mathbf{d}^{(1)} + \boldsymbol{\sigma}^{(2)} \mathbf{d}^{(2)} = \mathbf{0} \quad \text{on } \Gamma_{\cup} \quad (5.72)$$

where the superscripts  $(\cdot)^{(1),(2)}$  refer to the two coupling domains and where  $(\boldsymbol{\sigma} \mathbf{d})$  is the traction along the coupling interface  $\Gamma_{\cup}$ . The governing equations of the principal of virtual work (5.22) are extended according to 5.36. Notwithstanding the formulation for essential boundary conditions, the Nitsche term  $\mathcal{W}^{NIT}$  contributes only to the internal work since the external work contributions cancel out.

For a pure Kirchhoff-Love patch coupling, the consistency terms of the Nitsche extension reads:

$$\begin{aligned} \mathcal{W}_{cs}^{NIT} = & - \int_{\Gamma_{\cup}} \delta \{N^{\alpha} + b_{\gamma}^{\alpha} M^{\gamma}\} \cdot \{u_{(\alpha)}\} dS - \int_{\Gamma_{\cup}} \{N^{\alpha} + b_{\gamma}^{\alpha} M^{\gamma}\} \cdot \delta \{u_{(\alpha)}\} dS \\ & - \int_{\Gamma_{\cup}} \delta \{Q + M_{(d),s}\} \cdot \{u_{(3)}\} dS - \int_{\Gamma_{\cup}} \{Q + M_{(d),s}\} \cdot \delta \{u_{(3)}\} dS \\ & - \int_{\Gamma_{\cup}} \delta \{M_{(t)}\} \cdot \{\Phi_{(d)}\} dS - \int_{\Gamma_{\cup}} \{M_{(t)}\} \cdot \delta \{\Phi_{(d)}\} dS \end{aligned} \quad (5.73)$$

The stability terms of weak coupling extension are reformulated in terms of displacements of the mid surface  $\mathbf{u}$  and the normal vector  $\mathbf{a}_3$  as:

$$\begin{aligned} \mathcal{W}_{st}^{NIT} = & \int_{\Gamma_{\cup}} \tau_S t \delta \{\mathbf{u}\} \cdot \{\mathbf{u}\} dS + \int_{\Gamma_{\cup}} \tau_S \frac{t^3}{12} \delta \{\Phi\} \cdot \{\Phi\} dS \\ & + \int_{\Gamma_{\cup}} \tau_N t (\mathbf{d} \cdot \delta \{\mathbf{u}\}) (\{\mathbf{u}\} \cdot \mathbf{d}) dS + \int_{\Gamma_{\cup}} \tau_N \frac{t^3}{12} (\mathbf{d} \cdot \delta \{\Phi\}) (\{\Phi\} \cdot \mathbf{d}) dS \end{aligned} \quad (5.74)$$

where the terms in brackets are defined as follows:

$$\{N^{\alpha} + b_{\gamma}^{\alpha} M^{\gamma}\} := \beta (N^{\alpha} + b_{\gamma}^{\alpha} M^{\gamma})^{(1)} + (1 - \beta) (N^{\alpha} + b_{\gamma}^{\alpha} M^{\gamma})^{(2)} \quad (5.75)$$

$$\{Q + M_{(d),s}\} := \beta (Q + M_{(d),s})^{(1)} + (1 - \beta) (Q + M_{(d),s})^{(2)} \quad (5.76)$$

$$\{M_{(t)}\} := \beta M_{(t)}^{(1)} + (1 - \beta) M_{(t)}^{(2)} \quad (5.77)$$

$$\{\mathbf{u}\} := \mathbf{u}^{(1)} - \mathbf{u}^{(2)} \quad (5.78)$$

$$\{\Phi\} := \left( \mathbf{a}_3^{(1)} - \mathbf{a}_3^{(2)} \right) - \left( \mathbf{A}_3^{(1)} - \mathbf{A}_3^{(2)} \right) \quad (5.79)$$

The discretization of the consistency and stabilization terms of the coupling constraint follows in analogy to section 5.2.2. The value of  $\beta$  in (5.75) - (5.77) decides the contribution of each of the two coupled domains,  $\Omega^{(1)}$  and  $\Omega^{(2)}$ , to enforce the traction compatibility condition. In the extreme cases  $\beta = \{0, 1\}$  the condition is fully shifted to one of the participating domains, leaving the kinematic conditions (5.78) and (5.79) untouched. When not stated differently we use the setting  $\beta = 0.5$ .

## 5.4 Numerical examples: weak boundary conditions

We selected two benchmark problems to demonstrate the performance of the proposed method. The first example is the benchmark problem of Scordelis and Lo [224] to assess the convergence behaviour of our method. This problem is discretized boundary fitted. With the second example of an embedded, simply supported circular plate we introduce the finite cell method to overcome the trimming problem of CAD-derived models.

### 5.4.1 Scordelis-Lo shell problem

Using the Scordelis-Lo benchmark problems we tested the performance of our method with regard to the convergence behaviour [225] for an untrimmed NURBS shell structure. The geometry, the boundary conditions and the material properties of the shell model are given in Figure 5.3(a). The roof structure has rigid diaphragms at the curved boundaries, zero traction boundary conditions along the free edges and is subjected to a gravity load. Due to its symmetry, only a quarter of the geometry was modeled as depicted in Figure 5.3(b). The convergence of the deflection at the

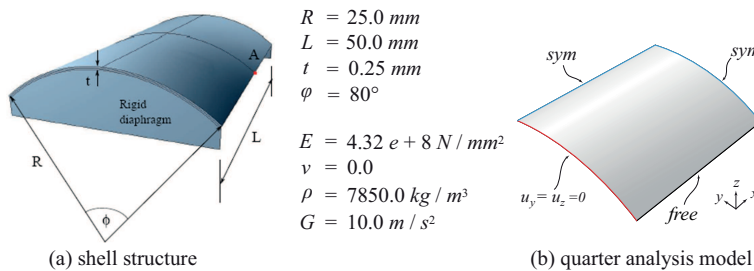


Figure 5.3: Scordelis-Lo problem: problem definition (a), applied boundary conditions (b).

midpoint of the free edge (point A) is shown in Figure 5.4 for a uniform h-refinement. For both polynomial degrees, cubic and quartic, we observed fast convergence to a value of  $u = 0.30059$  which corresponds to the value reported in [2]. In Figure 5.5 we show the convergence behavior in terms of the relative error in strain energy. An ad-hoc choice of  $C_N = C_S = 30$  was used and kept constant throughout the refinement steps which revealed an overall cubic rate. A reference strain energy value was obtained from extrapolation on the basis of the three most refined solutions of a uniform mesh refinement as proposed in [226].

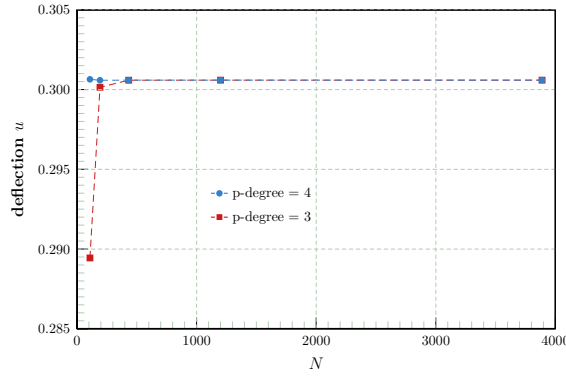


Figure 5.4: Scordelis-Lo problem: convergence for uniform mesh refinement – mid-point edge deflection.

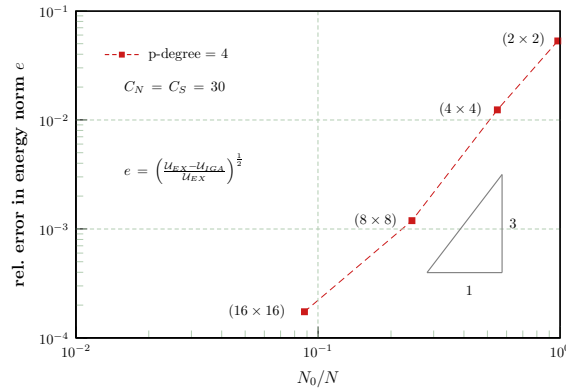


Figure 5.5: Scordelis-Lo problem: convergence for uniform mesh refinement – strain energy.

## 5.4.2 Bending of an embedded circular plate

With the following example we studied a circular plate of radius  $R$  which was embedded within a rectangular area. The geometry and material properties are shown in the Figure 5.6. The plate is subjected to uniform pressure  $\bar{p} = 1.0 \text{ N/mm}^2$ , and simply supported along the circular boundary. Due to symmetry, only a quarter of the plate was modeled. All boundary conditions were enforced weakly at the true physical domain boundary  $\Gamma$ .

An analytical reference solution for the plate deflection was taken from [227]:

$$u = -\frac{\bar{p}(R^2 - r^2)}{64D} \left( \frac{5 + \nu}{1 + \nu} R^2 - r^2 \right) \quad (5.80)$$

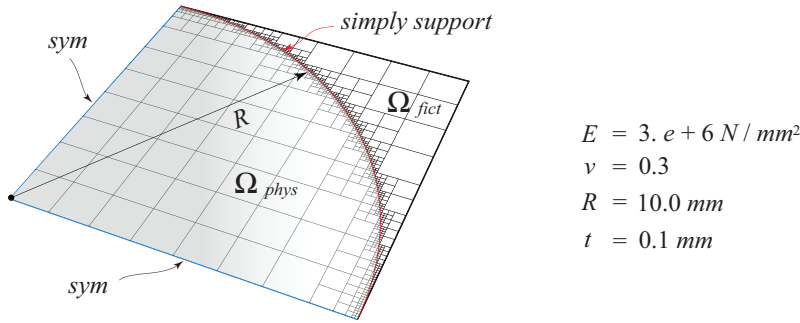


Figure 5.6: Geometry description of a simply supported circular plate embedded within a square domain.

where

$$D = \frac{Eh^3}{12(1-\nu^2)} \quad (5.81)$$

The embedding domain was discretized with  $8 \times 8$  elements of polynomial degree  $p = q = 3$ . The finite cell method used to account for the trimmed area requires integration of the governing equations inside the physical domain  $\Omega_{phys}$  and the fictitious extension domain  $\Omega_{fict}$  [114]. We used the composed integration of the equations as it was introduced in section 2.3, cf. Figure 5.6. A quadtree depth of  $m = 4$  was found to be sufficient for an accurate integration over the two domains,  $\Omega_{phys}$  and  $\Omega_{fict}$ . Constants  $C_S = C_N = 40$  were chosen empirically to stabilize sufficiently the analysis. The convergence behavior for uniform h-refinement is depicted in Figure 5.7.

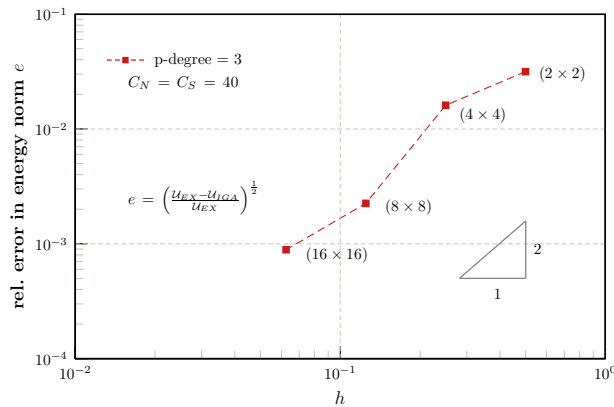


Figure 5.7: Circular plate: convergence for uniform mesh refinement.

The analysis results showed some dependency on the accuracy of the element-wise integration of the elasticity equations. The completely embedded domain boundary

was integrated with much higher accuracy for the Nitsche terms than for the domain integrals of the stiffness terms. For a higher resolution of this integration approach the quality of the analysis results will slightly increase at a much higher computational cost, see [104]. We think that the resolution used is a fair trade-off between accuracy and acceptable integration effort. Exact integration could be introduced by an element-wise use of the blending function method restricted to the numerical integration and without affecting the chosen approximation space as shown in [228].

In Figure 5.8(a) we show the deflection of the plate model and in Figure 5.8(b) we show the corresponding absolute error. For the cubic p-degree used the error distribution of the displacements is smooth and shows two peaks with a maximal error of roughly 0.001%.

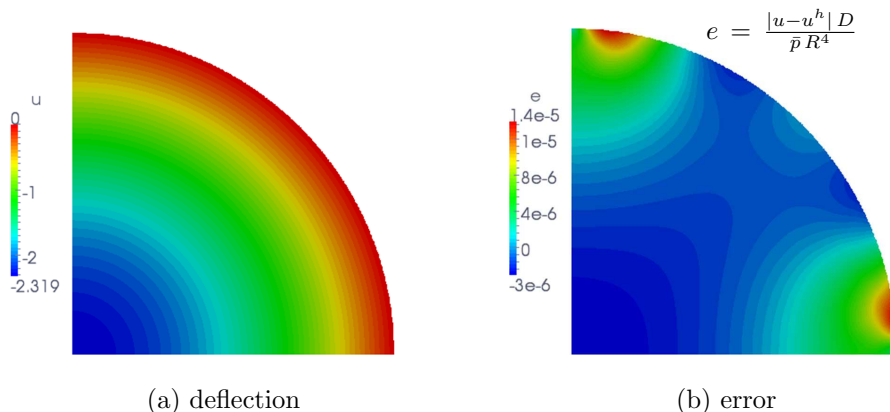


Figure 5.8: Circular plate: plate deflection (a) and absolute error (b).

We tested the error performance for a varying stability value  $C_S$ , where we set  $C_N = C_S$ , cf. Figure 5.9. The graph, Figure 5.9, shows the typical behavior with a peak indicating an optimal solution in terms of the error in strain energy. In [104, 113, 105] the computation of a suitable value for the constants  $C_S$  and  $C_N$  is documented. The computation of the values is based on a partial solution of a generalized eigenvalue problem approximating the upper bounds of a corresponding inequality typical for the estimation of the governing error bounds [223, 102]. Based on these computations we chose all values empirically in the examples shown in this manuscript.

## 5.5 Numerical examples: weak coupling constraints

In the following we reveal the overall performance of the proposed coupling approach with a series of examples to demonstrate the strength of the method for shell structures in the isogeometric analysis framework.

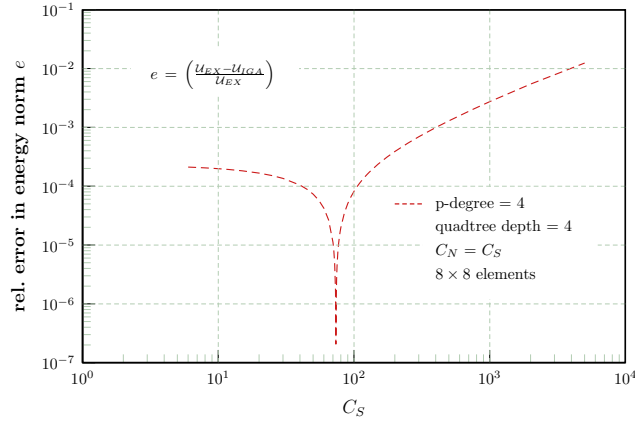


Figure 5.9: Circular plate: parameter study for stability value  $C_S$ .

First, we introduce the basic behavior and the unique properties of a pure Kirchhoff-Love patch coupling with two simple plate examples. In particular, we demonstrate the capability of the method to overcome the problem of a ‘hinge-effect’ due to the inherent  $C^0$ -continuity along the patch interfaces. We show that the bending moments are of the same quality as those for single patch models. Increasing complexity is introduced with the coupling of curve-bounded patches which assemble to the Scordelis-Lo benchmark problem. Then we select a Kirchhoff-Love shell patch T-joint model to demonstrate the successful coupling of folds. Finally, we present a joint tube problem to demonstrate the applicability of the proposed Nitsche approach for enforcing boundary conditions and coupling constraints in the complex engineering related structures.

### 5.5.1 Plate bending – simply supported rectangular domain

A two patch rectangular plate model was chosen to study the behavior along a curved coupling interface for pure bending. The geometry and the material properties of the plate model are depicted in Figure 5.10. The plate of thickness  $t$  is simply supported and subjected to a uniform pressure  $\bar{p}$ . Each of the two NURBS patches was discretized with  $8 \times 8$  elements with polynomial degrees  $p = q = 4$ . We compare the results of the coupled model with a single patch Kirchhoff-Love model of the same polynomial order with  $32 \times 16$  elements. The vertical displacement is shown on the deformed model in Figure 5.11(a). A comparison of the chosen discretization with the analytical solution shows a relative error of  $\sim 0.1\%$  for the maximum deflection. An overall impression of the quality of the bending moments is given exemplarily in Figures 5.11(b),(c). Both, the bending moment  $m_x$  and  $m_{xy}$ , respectively, show perfect smoothness of the solution field along the interface.

A representation of the bending moments  $m_x$  and  $m_y$  along the curved NURBS

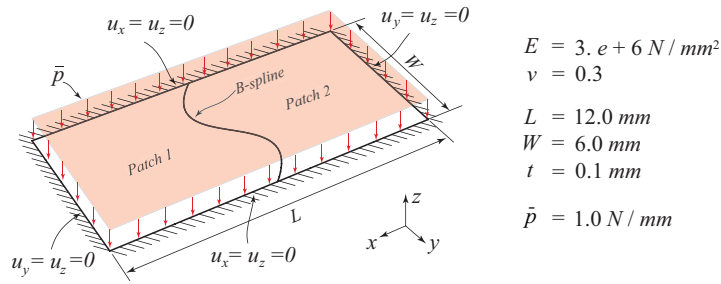


Figure 5.10: Two-patch rectangular plate domain coupled along a curved NURBS interface.

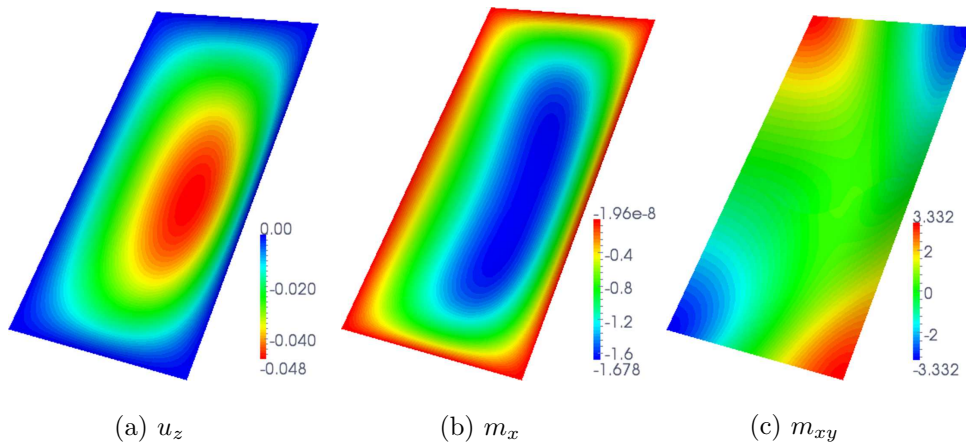


Figure 5.11: Deformed two-patch model: vertical displacements (a), bending (b) and twisting moment (c).

interface, cf. Figure 5.12, confirms the high accuracy of the results. Compared to an even more refined single patch solution there is virtually no visible difference in the solution quality. The patch coupling was stabilized using empirically chosen stability constants  $C_S = C_N = 10$ . Smaller stability constants are possible and retained the positive definiteness of the system matrix without influence on the quality of the shown solution fields.

The convergence behavior of the coupled plate model is shown in Figure 5.13. The depicted graphs, Figure 5.13, show the relative error in energy norm for a uniform h-refinement for two different coupling interfaces, the NURBS interface, shown in Figure 5.10, and a straight interface dividing the plate domain into two square coupled patches. Both models show monotonic convergence with a rate equivalent to the single patch solution for which the convergence curve was identical to the straight interface solution.

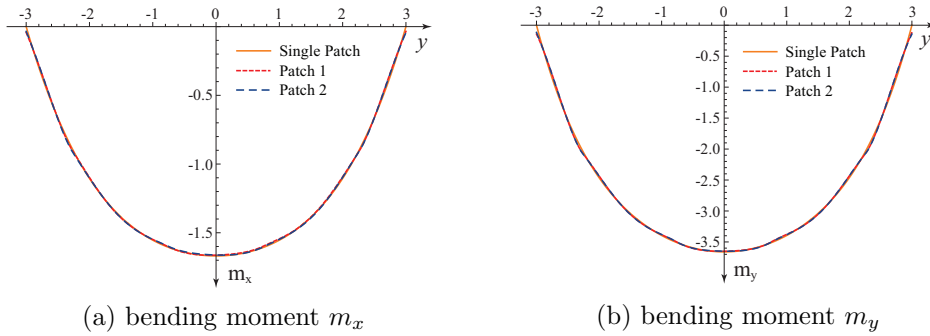


Figure 5.12: Plate bending: bending moments along the coupling interface.

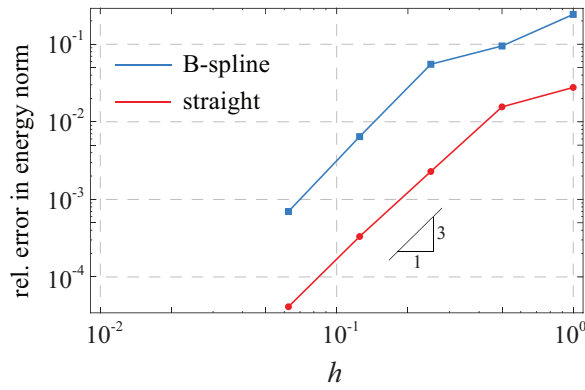


Figure 5.13: Convergence behavior of the simply supported plate.

### 5.5.2 Plate bending – cantilever plate

We choose a cantilever plate to demonstrate that the proposed approach is capable of overcoming the problem of a hinge effect due to the  $C^0$ -continuity along coupled patch boundaries. We chose a straight interface to couple two B-spline patches for this continuity test case. A strong,  $C^0$ -continuous coupling for the current configuration will fail since the hinge effect produces a kinematic system resulting in singular governing equations. The geometry, boundary conditions and material properties of the cantilever plate are depicted in Figure 5.14. The discretization was chosen in analogy to the example given in 5.5.1. Values of  $C_S$  and  $C_N$  equal to 10 were found to be sufficient to ensure a stable and accurate solution. We show the analysis results for the moment stress resultants  $m_x$  and  $m_y$  in Figure 5.15. All results show complete smoothness of the corresponding solution fields. Discontinuities are absent and the results do not show any hinge effect. This observation is supported by the plot of the moment stress resultant along the diagonal from free to clamped end,

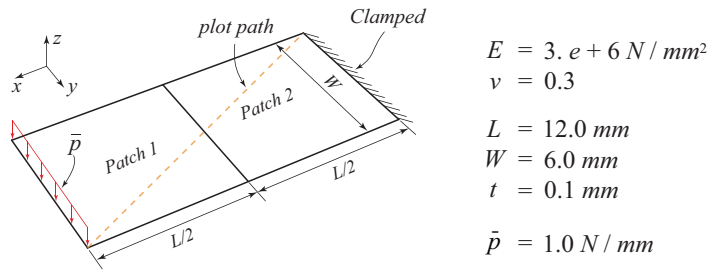


Figure 5.14: Two-patch cantilever plate domain coupled along a straight interface.

shown in Figure 5.15(c).

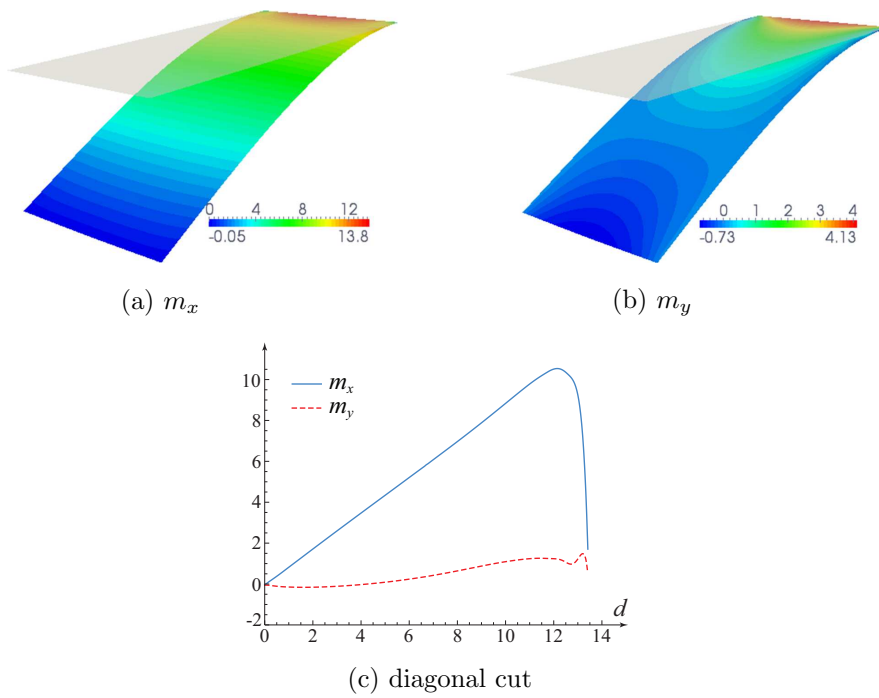


Figure 5.15: Two-patch cantilever plate model: plot of bending moments (a), (b), and results along a diagonal from free to clamped end (c).

### 5.5.3 Scordelis-Lo roof

We tested the performance of the shell coupling approach using the Scordelis-Lo benchmark [225, 224]. The geometry, the boundary conditions and the material

properties of the shell model are given in Figure 5.16(a). The roof structure has rigid diaphragms at the curved boundaries, free boundary conditions along the free edges and is subjected to a gravity load. We used a composed patch assembly consisting of three patches with curved coupling interface as depicted in Figure 5.16(b) to test for the accuracy of the coupled model. Sufficient convergence with a

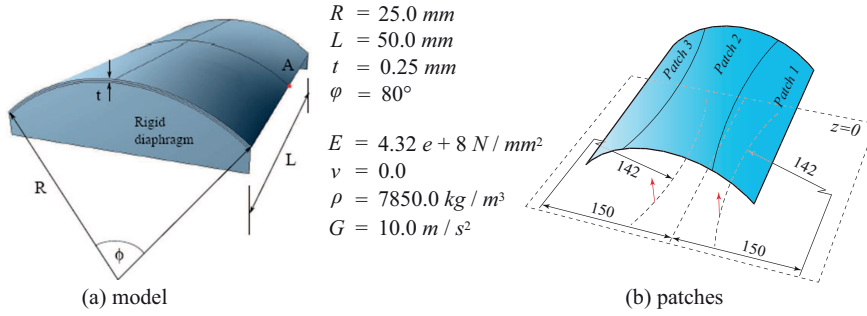


Figure 5.16: Scordelis-Lo problem: problem definition (a), three patch model (b).

relative error in energy norm below 1% was observed for a discretization with  $36 \times 6$  elements for each of the patches with a polynomial degree  $p = 4$  which resulted in conforming patch interfaces. To account for non-conforming coupling we considered a second coupled discretization with  $18 \times 6$  elements for the center patch. We used empirically chosen values  $C_S = C_N = 20$  for both models. The maximum vertical displacement at the mid-point of the outer shell rim (point A, Figure 5.16(a)) exactly met a reference value of  $u_z = 0.3006 \text{ mm}$ . The bending moments along the curved coupling interface are depicted in Figure 5.17. We show the results of the single patch solution with  $36 \times 18$  elements, and averaged values from two coupled patches of the conforming and non-conforming model in Figure 5.17. A comparison of the results shows virtually no difference in the solution results despite that we noticed an insignificant loss in quality for  $m_{11}$  of the non-conforming model. In particular, the solution is free of any discontinuity across the coupling interface as shown in Figure 5.18.

#### 5.5.4 Shell structures with folds – T-beam problem

So far we have concentrated on examples which are coupled in-plane as typically required for large and complex multi-patch shell structures, however, in practical applications different patches may meet at a specific angle other than zero leading to a fold between the patches. In the following example such a shell fold is presented with the example of a T-beam for which a  $90^\circ$  angle must be preserved during deformation. The geometry and material properties of the T-beam model are depicted in Figure 5.19. The T-beam is clamped at one end and loaded with a point load at the end of the flange of patch 1, both patches are modeled as Kirchhoff-Love shells. The coupling interface for patch 2 is defined through-the-thickness of the shell patch

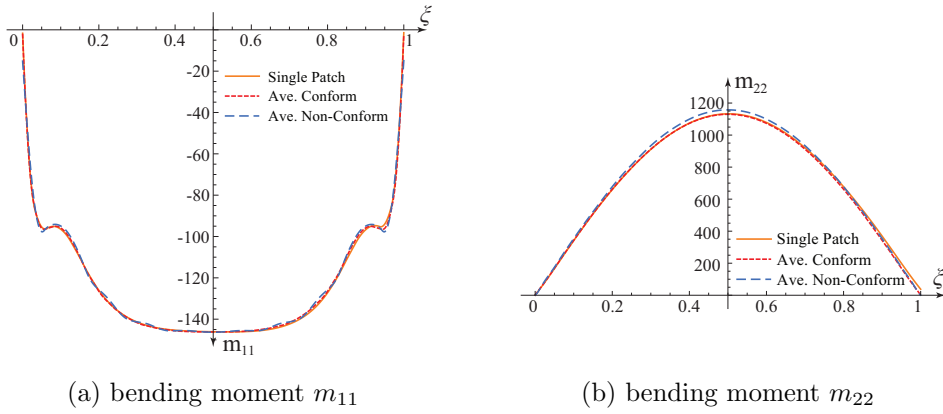


Figure 5.17: Scordelis Lo: bending moments along the coupling interface.

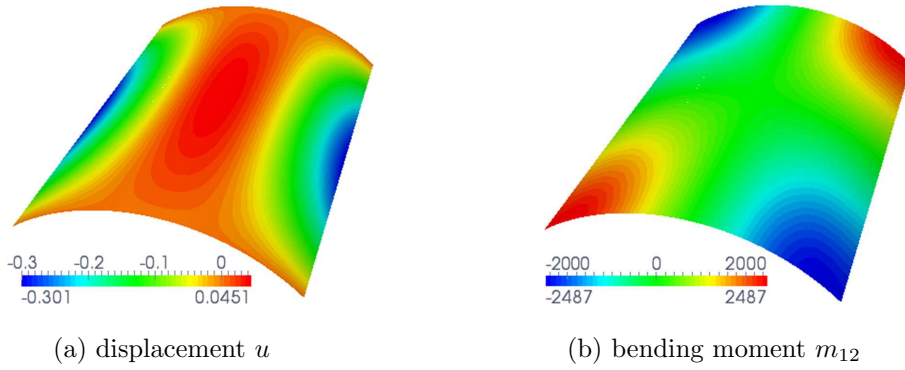


Figure 5.18: Scordelis Lo: analysis results.

while for patch 1 the interface is a strip of width  $t$  parallel to its mid surface. The

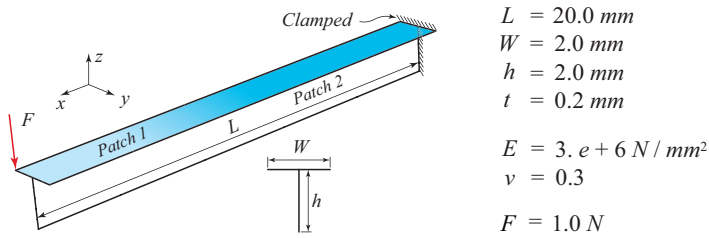


Figure 5.19: T-beam problem description.

base bar, patch 2, is discretized with  $8 \times 4$  elements. For the flange, patch 1, we consider two different discretizations. Model  $A$  consists of  $8 \times 3$  elements whereas model  $B$  consists of  $8 \times 4$  elements, cf. Fig. 5.20. For the discretization model  $A$

the coupling interface strip of the base bar touches the flange elements centrally. For the discretization model  $B$  the interface strip couples in each case three elements touching two flange elements along their element boundary. All patches use a polynomial degree of  $p = q = 3$ . A value of 40 was empirically chosen for the stabilization constants  $C_N$  and  $C_S$  which showed sufficient stability. We demonstrate

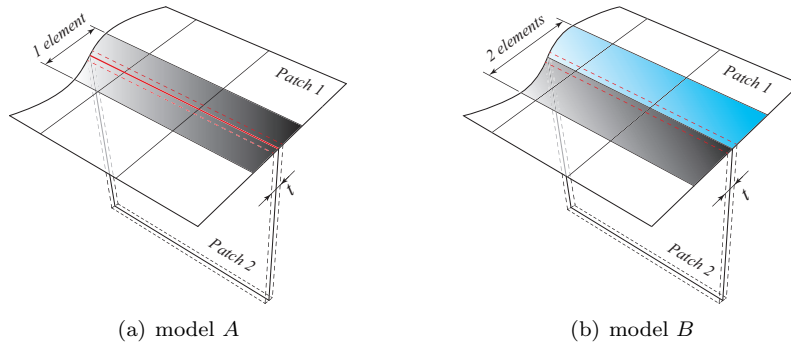


Figure 5.20: Different mesh configurations: piecewise coupling of two and three elements, respectively.

the convergence for the tip deflection of the two discretizations, model  $A$  and model  $B$ , and compare their results with a finite element shell solution obtained from an ABAQUS [187] analysis, see Figure 5.21. Uniform mesh refinement shows fast convergence for the three depicted solutions. A marginal difference in the converged solution is observed between discretization model  $A$  and the finite element reference solution. The non-conforming discretization of model  $B$ , piecewise involving three coupling elements, converges to a slightly higher value deviating by roughly 1.5% from the reference solution. Next we will demonstrate our method's capacity to

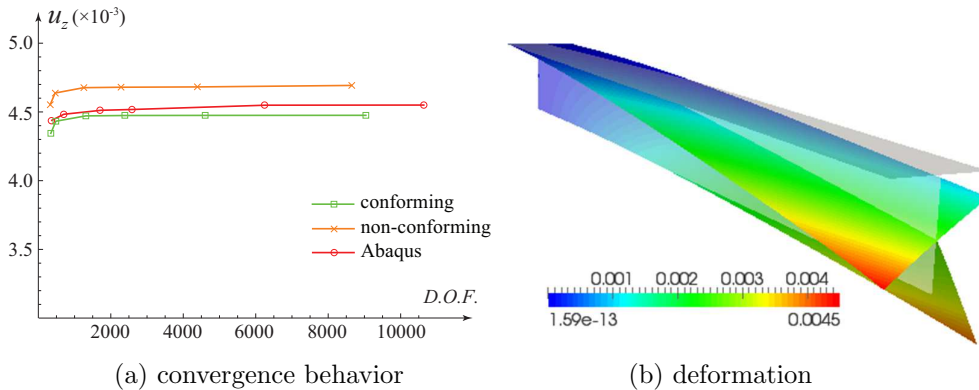


Figure 5.21: T-beam analysis results: convergence of the tip deflection (a), final configuration (b).

retain the  $90^\circ$  angle between the coupled patches. The applied tip load induces a bending and a torsional elastic response which requires an adequate corner stiffness. We show the relative error of the coupling angle along the center line of the interface strip in Figure 5.22. Between the length coordinate  $0 \leq L \leq 15$  we observe a relative error close to zero. In the last quarter the error increases by one order of magnitude, still providing an acceptable result for practical applications without significant consequence for the tip deflection. A further element-wise increase of the stability value in this last quarter by a value  $\Delta$  allows the method to be fully controlled. A value of  $\Delta = 2$  was sufficient for a reduction of the error into the prevalent range.

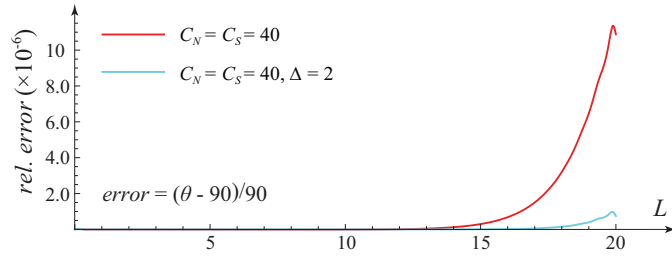


Figure 5.22: Relative error of the  $90^\circ$  angle along the length of T-beam.

### 5.5.5 Pipe junction under pressure loading

Finally, the applicability of our approach for a complex geometry of practical relevance is demonstrated. We consider in this example a junction of a pipe system. The numerical model was derived from a CAD design which was assembled of three, partially trimmed, NURBS-patches, cf. Figure 5.23. The connected pipes were assumed to be of infinite length thus calling for symmetric boundary conditions at the circumferential pipe boundaries. Symmetric boundary conditions were also applied along the symmetry axis of the structure to account for considering only its symmetric part. Additional boundary conditions were introduced at the upper face of the horizontal tube to prevent rigid body motions.

The three NURBS patches were discretized independently which resulted in non-conforming meshes. The weakly enforced essential boundary conditions and coupling constraints are depicted in Figure 5.23, indicated in blue and red, respectively, where we also provide the geometry and material properties of the model. In Figure 5.24 we provide a detail view of the connector which was derived from a connector control NURBS curve specified with the shown control net. The connector NURBS surface around the circumference of the upper tube was created with a sweep along the upper and lower model interfaces, indicated in red.

The coupling of the used three patch model results in a redundant area on the horizontal pipe surface which we trimmed by introducing a fictitious domain according

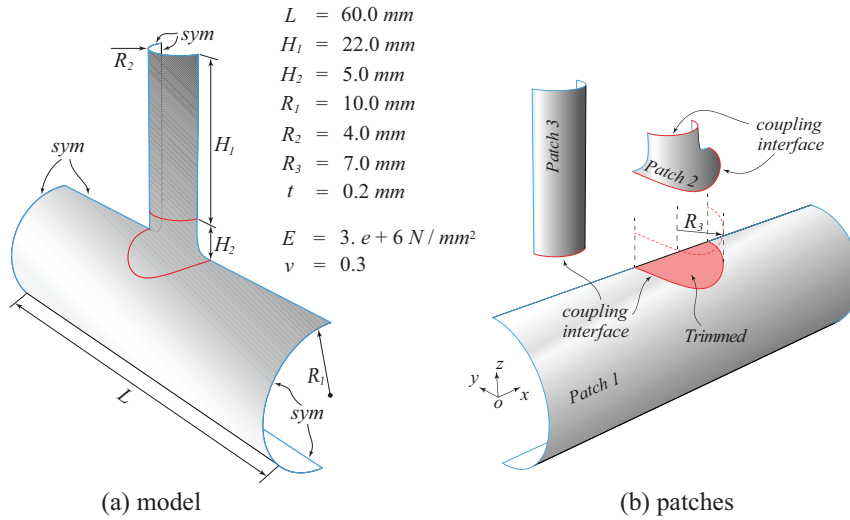


Figure 5.23: Geometry description of the cross tube (a), three patch model (b).

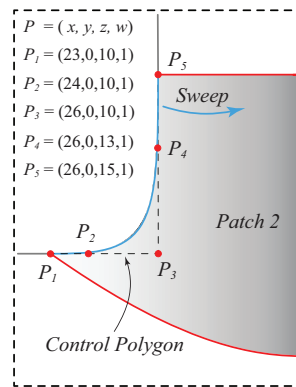


Figure 5.24: Front view of the connector and the boundary curve geometry representations

to the finite cell method. For the composed integration of the governing equations of the finite cell method we used a quadtree of tree depth four. As an alternative this redundant area can be avoided by a split of the horizontal patch into three coupled patches, each providing the topology of a quadrangle. We think that the application of the finite cell method is the more elegant approach following very closely the trimming principles of CAD software packages [143].

The tube is subjected to an inner pressure load of  $\bar{p} = 1.0 \text{ N/mm}^2$ . For simplicity, the values of  $C_S$  and  $C_N$  were set to a value of 30 for both the essential boundary conditions and the coupling constraints. Patch 1 was discretized with  $48 \times 26$  ele-

ments, patch 2 with  $28 \times 24$  elements and patch 3 with  $24 \times 16$  elements, cf. Figure 5.23(b). A p-degree  $p = 4$  was chosen for all three NURBS patches. In Figure 5.25(a) we depict the deformed model as an overlay to the undeformed structure. The deformed model is fully symmetric and has a smooth displacement field along all constraint boundaries and interfaces. In Figure 5.25(b) we show that the von Mises stresses are of the same quality as the displacement field. The stress distribution is free of any discontinuities and provides the expected higher order smoothness according to the usual properties of isogeometric single patch analysis models with strongly enforced essential boundary conditions. An equivalent solution quality was observed for the moment stress resultants, depicted in Figure 5.26 and the normal and shear stress resultants as shown in Figure 5.27. The only visible deviation from a continuous smoothness of the solution was observed for the in-plane shear moment  $m_{12}$ , Figure 5.26(c), which we consider to be insignificant since the visible jump in the moments is locally bounded and is not of influence for the overall response of the complex structure. A comparison of the displacement field along the coupling

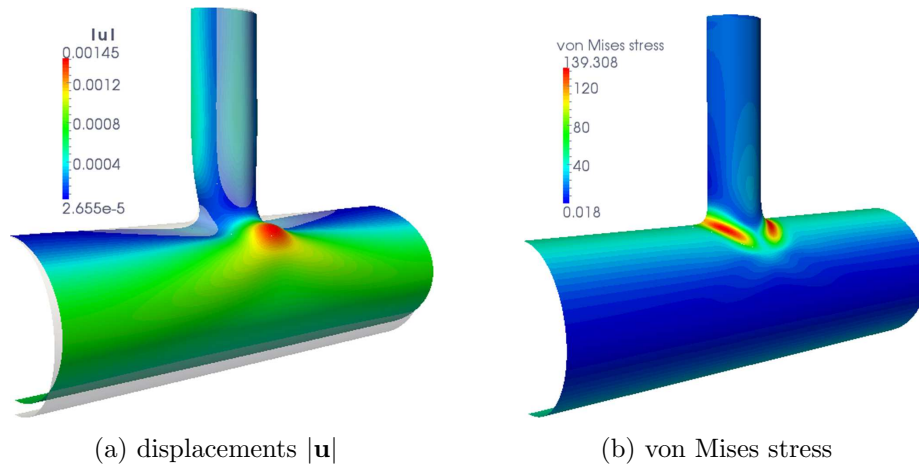


Figure 5.25: Scaled displacement field (factor 2400) of the deformed structure and von Mises stress distribution.

interfaces of the pipes is shown in Figure 5.28. The two solutions show virtually no difference. The ABAQUS reference solution was obtained with 13521 quadratic Mindlin shell elements.

## 5.6 Summary

A variationally consistent extension for the weak enforcement of essential boundary conditions and multi-patch coupling constraints of isogeometric Kirchhoff-Love shells was presented in this chapter. We showed the fundamentals of the applied

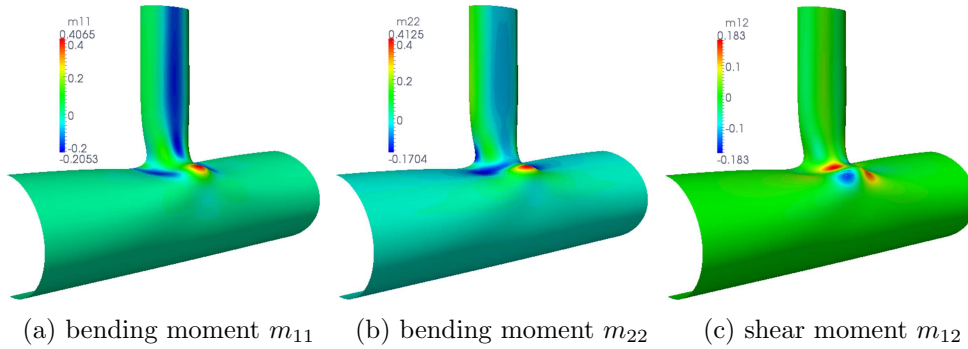


Figure 5.26: Moment bending and shear resultants.

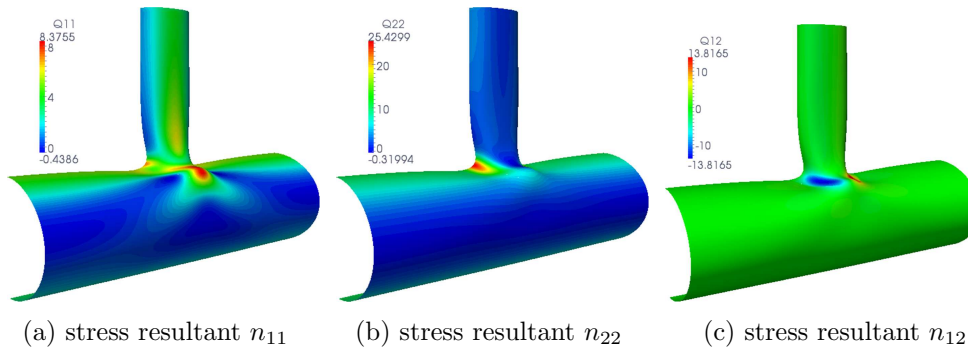


Figure 5.27: Normal and shear force resultants.

mathematical models and provided a corresponding discretization with regard to the additional consistency and stabilization terms with NURBS. The trimming of NURBS geometries was taken into account by the conceptual use of the finite cell method.

For the enforcement of essential boundary conditions, we demonstrated the potential of the proposed approach with two benchmark tests revealing a high accuracy of the results in combination with optimal convergence behavior. The method's performance was demonstrated using the Scordelis-Lo benchmark problem where symmetry boundary conditions were directly applied to the shell boundary without the need for additional control points inside the shell domain to ensure properly enforced rotational boundary constraints. The problem of trimmed NURBS structures was addressed with a circular plate problem which was embedded in a square analysis domain.

For the enforcement of coupling constraint, we demonstrated, with several examples,

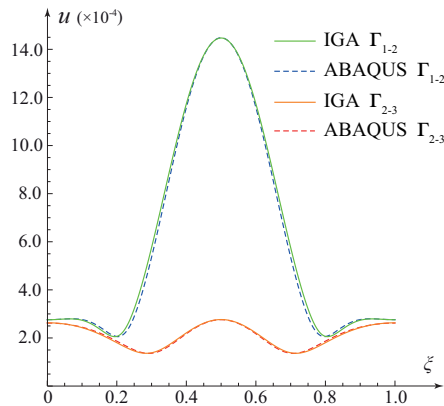


Figure 5.28: Displacements along the coupling interfaces – comparison with an ABAQUS reference solution.

that a hinge effect for  $C^0$ -continuous patch boundaries is completely removed using the proposed weak coupling strategy and that bending moments are correctly transferred between adjacent patches. The presented examples showed highest smoothness across the coupling interface for displacements and moment stress resultants in the quality of single patch solutions. The example of a T-beam was chosen to demonstrate the coupling approach for folded shell models where the angle of the fold must be preserved. The results demonstrated a reliable and accurate coupling behavior for different discretizations. Finally we used a pipe junction under inner pressure to demonstrate the reliability and applicability of the method for engineering relevant structures. The high quality of the solution in terms of displacements and moment and force stress resultants confirmed the efficiency of the proposed method and the potential for further developments. An inevitable stabilization of the weak boundary and weak coupling method was ensured on the basis of ad-hoc choices for the two free parameters to demonstrate its high robustness. None of the examples required additional studies on optimal stability values to ensure a sufficiently high solution quality.

We believe that the method has the potential to become a standard in the framework of isogeometric analysis. The method shows a high degree of robustness, it fully retains the basic and beneficial properties of higher order methods such as excellent convergence behavior and increased per-degree-of-freedom accuracy. The combination of the finite cell method with the weak enforcement of essential boundary and coupling constraints provides a highest level of flexibility in the modeling chain of NURBS-based shell structures.



## Chapter 6

# Blending of multi-patch composite shell models<sup>1</sup>

Three-dimensional continuum-like shell elements are computationally less efficient compared to their geometry-reduced shell element counterparts but provide a sound complete three-dimensional stress state. Despite the sophistication of geometry reduced shell models such as Kirchhoff-Love type shells or Reissner-Mindlin type shells, a need still exists for a highly accurate three-dimensional stress state, at least in locally bounded domains. Edge effects in composite shells [53, 229], crack models [230, 231] or the problem of delamination in laminated composites [201, 232] are examples of where the failure model requires knowledge of an accurate stress state. A blending of the two shell models, Kirchhoff-Love models and solid-like models increases the computational efficiency for large scale models which require only a locally bounded insight into the full three-dimensional stress state. The different elements request a coupling which ensures continuous displacements and force equilibrium at the interface. In [233, 234, 235], constraint equations are used to couple models with different geometric dimensions and stress states. Alternatively, transition elements are used by a number of researchers to couple beam, plate and shell elements with solid elements [236, 237, 238, 239].

In this chapter, Nitsche's method is extended to the blended coupling of isogeometric shell patches based on the theory of Kirchhoff-Love and solid-like continuum shells. The solid-like shell element used in this chapter can be naturally derived from the layerwise shell theory presented in chapter 3. We introduce an equivalent geometric model definition, a mid-surface description, for both shell types which facilitates a generalized and more flexible geometry modeling. The proposed approach further allows the coupling of conforming and non-conforming patches with trimmed cou-

---

<sup>1</sup>This chapter is based on the paper “Y. Guo, M. Ruess, Nitsche's method for a coupling of isogeometric thin shells and blended shell structures, *Computer Methods in Applied Mechanics and Engineering*, 284, 881-905, 2015”

pling interfaces which greatly facilitates the modeling and analysis of a larger class of structures in engineering and science.

This chapter is organized as follows: in section 6.1, a concise description of the solid-like shell model is presented followed by the Nitsche's extension for a blended coupling of shell patches and followed by the approach used to determine suitable stability constants. The performance of the proposed method is documented with several numerical examples in section 6.2. Conclusions and main findings are drawn in section 6.3.

## 6.1 Nitsche's method for coupling constraints in blended shell models

In a first step the principal strategy for the coupling of different shell lamina theories is developed and tested for single layer shell structures. Nitsche's method is used to couple isotropic solid-like shell elements and Kirchhoff-Love elements. Using the findings of single layer coupling the principle is extended in a second step to blended multi-layer lamina models.

### 6.1.1 Isogeometric solid-like shells

The solid-like shell model for isotropic materials can be naturally derived from the layerwise shell element of chapter 3. The differences are in the through-the-thickness interpolation of displacement field and the constitutive equations. For composite laminates, the continuity of transverse displacement field at ply interfaces is decreased to  $C^0$  to account for the balance of linear momentum of dissimilar layers, cf. Figure 3.2, while for isotropic materials, the natural continuity of the used B-spline is kept through the shell thickness. The governing equations and the corresponding discretization of both, the solid-like shell element and layerwise shell element is according to section 3.2.2.

### 6.1.2 Nitsche's extension of coupling constraints

The extended principle of virtual work (5.36) is used to introduce the Nitsche work contribution for the coupling of pure isotropic solid patches:

$$\begin{aligned} \mathcal{W}^{NIT} = & - \int_{\Gamma_U} \delta\{\mathbf{S} \mathbf{d}\} \cdot \{\mathbf{u}\} da - \int_{\Gamma_U} \delta\{\mathbf{u}\} \cdot \{\mathbf{S} \mathbf{d}\} da + \int_{\Gamma_U} \tau_S \delta\{\mathbf{u}\} \cdot \{\mathbf{u}\} da \\ & + \int_{\Gamma_U} \tau_N (\mathbf{d} \cdot \delta\{\mathbf{u}\}) (\{\mathbf{u}\} \cdot \mathbf{d}) da \quad (6.1) \end{aligned}$$

where  $\mathbf{d}$  is the in-plane unit normal vector along the coupling interface  $\Gamma_U$ , in this case is a 2D surface, where  $\mathbf{S}$  denotes the stress tensor referred to the global coordinate system, where  $\tau_S$  and  $\tau_N$  are stabilization parameters corresponding to the shear and normal related components of the traction [104, 113], and:

$$\{\mathbf{u}\} := \mathbf{u}^{(1)} - \mathbf{u}^{(2)} \quad (6.2)$$

$$\{\mathbf{S} \mathbf{d}\} := \beta \mathbf{S}^{(1)} \mathbf{d}^{(1)} + (1 - \beta) \mathbf{S}^{(2)} \mathbf{d}^{(2)}, \quad \beta = [0, 1] \quad (6.3)$$

The extension terms are expressed in terms of the unknown displacements of the formulation and thus fully contribute to a modified stiffness matrix on the left hand side of the discretized system of equations. The superscripts  $(\cdot)^{(1),(2)}$  refer to the two coupling domains.

For the blended coupling, the weak enforcement of the coupling conditions extends over the complete coupling interface, as illustrated in Figure 6.1. Integration of (6.1) over the coupling interface between the solid and Kirchhoff-Love interface requires the evaluation at integrations points in both domains. For the Kirchhoff-Love shell, the assumption of a linear displacement field through the shell thickness is taken into account. The consideration of transverse shear in the Kirchhoff-Love model can either be taken into account by an assumed parabolic shear stress distribution through the thickness or by a one-sided coupling as used here. For the former, the transverse shear force is first obtained by using force and moment equilibrium equations of the shell, then, a parabolic shape distribution is assumed for the recovering of the transverse shear stress. For the latter the parameter  $\beta$  of (6.3) is set to the extreme values such that the compatibility condition is fully shifted to the solid patch to adopt the three-dimensional stress state. The one-sided coupling results in the following consistency terms:

$$\mathcal{W}_{cs}^{NIT} = - \int_{\Gamma_U} \delta(\mathbf{S} \mathbf{d})^{(solid)} \cdot \{\mathbf{u}\} da - \int_{\Gamma_U} \delta\{\mathbf{u}\} \cdot (\mathbf{S} \mathbf{d})^{(solid)} da \quad (6.4)$$

the stability terms for isotropic shells remain as introduced in (6.1). For the coupling of laminated composite shells, the stability terms are introduced in subsection 6.1.3.

### Discrete Kirchhoff-Love shell kinematics - blended coupling

The displacement field of the Kirchhoff-Love shell follows from the shell kinematics introduced in section 5.1, and is assumed to be linear through the shell thickness:

$$\mathbf{u} = \mathbf{u}^0 + \xi_3 t (\mathbf{a}_3 - \mathbf{A}_3) \quad (6.5)$$

where we denote the mid-surface displacement of the Kirchhoff-Love shell with  $\mathbf{u}^0$ . The derivatives of  $\mathbf{u}$  with respect to the displacement variables  $\mathbf{U}_r$  follow as:

$$\mathbf{u}_{,r} = \mathbf{u}_{,r}^0 + \xi_3 t \mathbf{a}_{3,r} \quad (6.6)$$

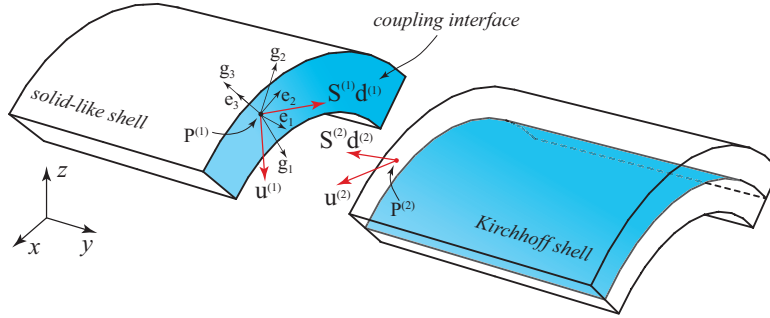


Figure 6.1: Illustration of the weak coupling of Kirchhoff-Love and solid-like shell patches.

where  $\mathbf{A}_3$  is independent of  $\mathbf{U}_r$  and therefore vanishes in the above equation. The derivatives  $\mathbf{u}_{,r}^0$  provide the interpolation rule for the components of the linear strain operator  $\mathbf{B}$ . The derivatives  $\mathbf{a}_{3,r}$  are calculated according to Appendix A.

### 6.1.3 Blended coupling of composite laminates: evaluation of stabilization constants

In general, the coupling extension (5.36) for isotropic materials in our framework applies two terms for stabilization,  $\tau_S$  and  $\tau_N$ , to counteract the singular system of equations. For optimal convergence properties, the choice of  $\tau_S$  and  $\tau_N$  should be proportional to the material properties, here the Lamé constants  $\lambda$  and  $\nu$  [208], inversely proportional to the element diameter  $h$  and in dependence of the constants  $C_S$ ,  $C_N$  which depend on the polynomial degree of the applied approximation space [222, 217], cf. (5.51) and (5.52). The constants  $C_S$  and  $C_N$  can be bounded explicitly by the consideration of discrete trace inequalities [240]. Alternatively, reliable values of  $C_S$  and  $C_N$  can be determined by the partial solution of an eigenvalue problem for the largest eigenvalue which provides a suitable estimate for a stable computation scheme [104, 113]. For laminate composite shell structures the split according to Lamé constants introduces an unnecessary complexity which is avoided in the following by a simplified approach which replaces the computation of  $C_S$  and  $C_N$  by the computation of  $\tau_S$  only. The example of sub-section 6.2.4 show that for materials values used in engineering this stabilization is sufficient to ensure optimal convergence properties. The eigenvalue problem used to compute adequate stability constants is presented in the following. First, the case of pure thin laminate composites is considered and second the blended formulation is taken into consideration.

### Thin shell patches

The stabilization terms of equation (5.74) are modified in the following:

$$\mathcal{W}_{st}^{NIT} = \int_{\Gamma_{\cup}} \alpha_u \delta\{\mathbf{u}\} \cdot \{\mathbf{u}\} da + \int_{\Gamma_{\cup}} \alpha_\theta \delta\Phi \cdot \Phi da \quad (6.7)$$

where  $\alpha_u$  and  $\alpha_\theta$  refer to the stabilization parameters of the displacements and rotations of shell's midsurface, respectively.

According to the generalized inverse estimates [241], there exist mesh-dependent positive constants  $C_F$  and  $C_M$  such that the boundary reactions of the two coupled shell patches are bounded by the strain energy of the two boundary domains in the form:

$$\|\{\mathbf{F}\}\|_{\Gamma_{\cup}}^2 \leq C_F (\mathcal{W}_I^{(1)}(\mathbf{u}, \delta\mathbf{u}) + \mathcal{W}_I^{(2)}(\mathbf{u}, \delta\mathbf{u})) \quad (6.8)$$

$$\|\{M_{(t)}\}\|_{\Gamma_{\cup}}^2 \leq C_M (\mathcal{W}_I^{(1)}(\mathbf{u}, \delta\mathbf{u}) + \mathcal{W}_I^{(2)}(\mathbf{u}, \delta\mathbf{u})) \quad (6.9)$$

where the expression  $\|\cdot\|$  denotes  $L^2$ -norm of a vector or a quantity, the subscript signifies the integration domain, and a bracket  $\{\cdot\}$  denotes the two mutually influencing coupling domains defined according to (5.75)-(5.77). The term  $\mathbf{F}$  is the force vector assembled from the effective in-plane membrane force  $N^\alpha + b_\gamma^\alpha M^\gamma$  and the effective transverse shear force  $Q + M_{(d),s}$ .

Making use of Young's inequality, a lower bound of the inner work enriched with Nitsche terms can be obtained (see [241, 113]) and the coercivity of the formulation is ensured when  $\alpha_{(*)} > 2C_{(*)}$ , where the constants  $C_{(*)}$  are chosen as the largest eigenvalue of the generalized eigenvalue problem which is defined in consideration of (6.8) and (6.9), respectively:

$$\mathbf{A}^{(*)}\mathbf{u} = \lambda_{(*)}\mathbf{B}\mathbf{u} \quad (6.10)$$

where matrix  $\mathbf{B}$  of the two coupled domains is defined as:

$$\mathbf{B} = \sum_{k=1}^2 \int_{\Omega_k} \left( \frac{\partial \mathbf{n}}{\partial \mathbf{U}_s} : \frac{\partial \boldsymbol{\varepsilon}}{\partial \mathbf{U}_r} + \frac{\partial \mathbf{m}}{\partial \mathbf{U}_s} : \frac{\partial \boldsymbol{\kappa}}{\partial \mathbf{U}_r} \right) dA \quad (6.11)$$

and  $\mathbf{A}^{(*)}$  is defined in accordance to the  $L^2$ -norm definition:

$$\mathbf{A} = \int_{\Gamma_{\cup}} [\mathbf{A}^F]^T \mathbf{A}^F da \quad (6.12)$$

$$\mathbf{A} = \int_{\Gamma_{\cup}} [\mathbf{A}^M]^T \mathbf{A}^M da \quad (6.13)$$

with

$$\mathbf{A}^F = \left[ \begin{array}{ccc|ccc} \cdots & \beta (N^1 + b_\gamma^1 M^\gamma)_{,i}^{(1)} & \cdots & \cdots & (1 - \beta) (N^1 + b_\gamma^1 M^\gamma)_{,j}^{(2)} & \cdots \\ \cdots & \beta (N^2 + b_\gamma^2 M^\gamma)_{,i}^{(1)} & \cdots & \cdots & (1 - \beta) (N^2 + b_\gamma^2 M^\gamma)_{,j}^{(2)} & \cdots \\ \cdots & \beta (Q + M_{(d,s)})_{,i}^{(1)} & \cdots & \cdots & (1 - \beta) (Q + M_{(d,s)})_{,j}^{(2)} & \cdots \end{array} \right] \quad (6.14)$$

$$\mathbf{A}^M = \left[ \begin{array}{ccc|ccc} \cdots & \beta M_{(t,i)}^{(1)} & \cdots & \cdots & (1 - \beta) M_{(t,j)}^{(2)} & \cdots \end{array} \right] \quad (6.15)$$

in which, without specific notification it is assumed that,  $\beta = 0.5$ , and that the derivatives  $(N^\alpha + b_\gamma^\alpha M^\gamma)_{,i}$ ,  $(Q + M_{(d,s)})_{,i}$  and  $M_{(t,i)}$  are linearized at  $\mathbf{u} = \mathbf{0}$  cf. (5.58)-(5.61).

### Blended shell patches

For the blended coupling of laminated composite shell patches, a single-sided coupling has proven to be a sufficient stable and accurate approach for the engineering problems considered in this thesis. For a single-sided coupling the parameter  $\beta$  takes the extreme values 0 or 1, respectively, so that the coupling conditions are fully shifted to the layerwise patch. In this case, the stabilization terms of Nitsche's extension (6.1) are:

$$\mathcal{W}_{st}^{NIT} = \int_{\Gamma_\cup} \alpha \delta\{\mathbf{u}\} \cdot \{\mathbf{u}\} da \quad (6.16)$$

where the stability parameter  $\alpha$  is estimated using (6.10). Again, it is assumed that there exist mesh-dependent positive constants  $C_L$  such that the  $L^2$ -norm of the boundary reactions of the layerwise patch is bounded by the strain energy:

$$\|(\mathbf{S} \mathbf{d})^{(solid)}\|_{\Gamma_\cup}^2 \leq C_L \int_{\Omega} (\mathbf{S} : \delta \mathbf{E})^{(solid)} d\Omega \quad (6.17)$$

The matrices  $\mathbf{A}$  and  $\mathbf{B}$  read:

$$\mathbf{A} = \int_{\Gamma_\cup} (\mathbf{S} \mathbf{d})^T (\mathbf{S} \mathbf{d}) da \quad (6.18)$$

$$\mathbf{B} = \int_{\Omega} (\mathbf{S} : \delta \mathbf{E})^{(solid)} d\Omega \quad (6.19)$$

where the coercivity of the blended coupling formulation is ensured when  $\alpha > C_L$ , and the constant  $C_L$  is chosen as the largest eigenvalue of the generalized eigenvalue problem. One may refer to [113] for more details of the estimation of stabilization parameters for solid patch coupling.

## 6.2 Numerical examples

In the following, several numerical studies are presented for the blended coupling of shell patches with different mathematical models, namely the Kirchhoff-Love shell and a 3D-solid or layerwise shell [78, 232]. Such a blended coupling will allow us to obtain a more accurate insight into the complete state of stress at selected locations of interest within larger multi-patch structures.

### 6.2.1 Consideration of refined patches – pinched cylinder problem

In the following example of a pinched cylinder we turn to blended shell structures and study the options for simple model refinement using a locally bounded solid patch around the loading zone. The geometry, boundary conditions and the material properties for this problem are depicted in Figure 6.2. The cylinder is supported by rigid diaphragms at both ends and subjected to a pair of concentrated opposing unit forces  $F$ . As the cylinder is symmetric we modeled only half of the cylinder

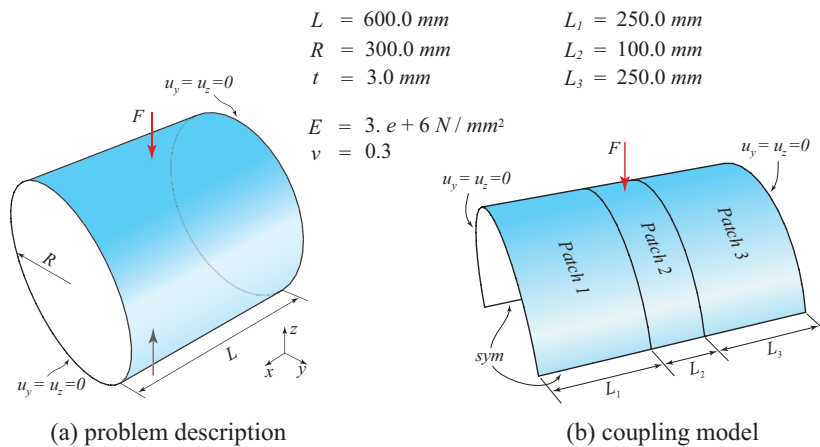


Figure 6.2: Pinched cylinder problem: (a) geometry, material properties and boundary conditions, (b) multi-patch analysis model.

which is assembled from three NURBS patches. The patches are coupled in radial direction along straight interfaces and symmetry boundary conditions are applied along the symmetry boundary. We avoid a further model reduction along the remaining symmetry axes to allow visual inspection of the symmetry properties of the analysis results. Furthermore, a locally more bounded refinement area is avoided to keep the number of patches to a minimum and to avoid sharp patch corners or trimmed patches which would require additional extensions and modifications of the presented theory. The discretization of the outer patches consists of  $10 \times 37$

elements. The refined inner solid patch of smaller dimension was discretized with  $18 \times 37 \times 1$  elements. The results were compared to a three patches pure Kirchhoff-Love model with equivalent discretization. The polynomial degree was kept constant for all patches of the two models at  $p^1 = p^2 = 4$ . This degree was also chosen for the through-thickness direction of the solid-like patch. The empirically chosen stability values were chosen to be  $C_S = C_N = 20$  for both, the pure Kirchhoff-Love shell coupling and the blended coupling.

In Figure 6.3 we show the convergence of the displacements under a unit point load and compare the result with a reference value of  $1.8248 \times 10^{-5}$  provided in [225]. Both models converge with two refinement steps, starting from the initial minimal NURBS-patch configurations, to the reference value. Both solutions overshoot insignificantly as already reported in [72]. A considerable difference in the number

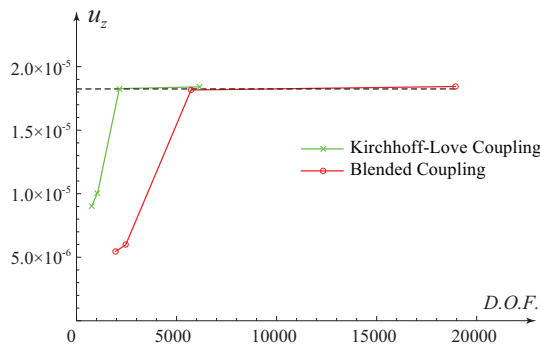
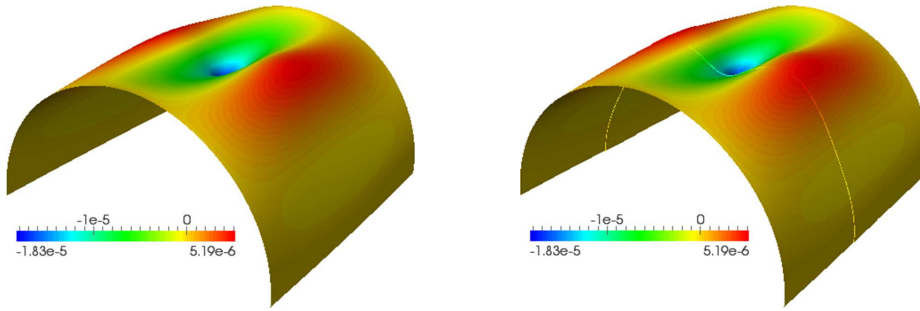


Figure 6.3: Pinched cylinder problem: convergence of the displacements.

of degrees of freedom is attributed to the different mathematical models used for the center patch, namely two geometry-reduced Kirchhoff-Love patches and a 3D thin solid model. This difference again supports the attempt to couple various shell models for an optimal performance trade off in terms of computational effort and expected accuracy. The total displacements of the shell are shown at the deformed model in Figure 6.4 with virtually no visible difference in quality. In Figure 6.5 we depict a cut of the solid patch through the point load location showing the transverse normal and transverse shear stress in full quality of the 3D elasticity theory. The Kirchhoff-Love theory does not provide these stress quantities as part of the mathematical model. In general they are retrieved in a post-processing step from the 3D equilibrium equations, typically at a much lower quality since second and third order derivatives of the displacement quantities are involved.

## 6.2.2 Blended coupling of Scordelis-Lo roof

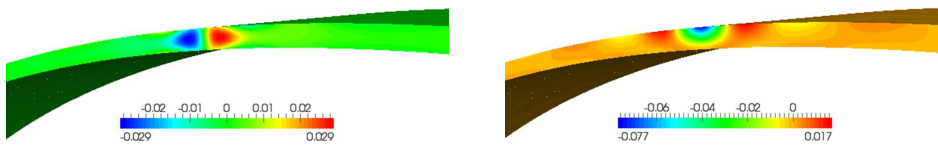
We reconsider the Scordelis-Lo roof from sub-section 5.5.3 for a blended coupling with refined solid boundary patches of the model. The middle patch, cf. Figure



(a) KL–KL–KL

(b) KL–solid–KL

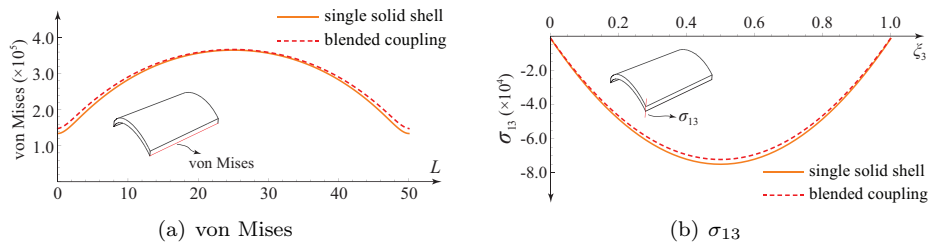
Figure 6.4: Total displacement of pinched cylinder problem: three patch Kirchhoff-Love (KL) model (a) and blended Kirchhoff-Love–solid model (b).


 (a)  $s_{23}$ 

 (b)  $s_{33}$ 

Figure 6.5: Pinched cylinder problem: transverse shear stress (a) transverse normal stress (b).

5.16 (b), remains a Kirchhoff-Love patch. We have chosen this example to show that the proposed method provides sufficient accurate stress results in the solid refinement patch. The discretization follows sub-section 5.5.3 with a single quartic element through thickness to model the solid-like patches. Again we compare our solution with a single patch solution of equivalent discretization. For both models,



(a) von Mises

 (b)  $\sigma_{13}$ 

 Figure 6.6: Stress plot of blended coupled and single solid-like shell patch Scordelis-Lo roof: (a) von Mises, (b) transverse shear stress  $\sigma_{13}$ .

the pure Kirchhoff-Love model and the blended model, convergence in the energy

norm under uniform  $k$ -refinement was observed. A reference value was obtained from extrapolation of the three most refined solutions of a single patch model. A comparison of the models reveal a difference in the modeling error expressed by the relative error in energy norm. For the three patches Kirchhoff-Love model we observed a relative error of  $\sim 1.0\%$  while the error of the blended model was at  $\sim 5.0\%$ .

In Figure 6.6 (a) we compare the von Mises stresses in the solid patch along the free boundary with the corresponding single patch solution. In Figure 6.6 (b) the accuracy of transverse shear stresses through the shell thickness are disclosed. Both results, compared to the single patch solution, showed an equivalent accuracy and smoothness. We noticed only a slight difference of the solution curves with a maximum deviation of roughly 5% which we consider to be an acceptable result.

### 6.2.3 Frequency analysis of a stringer stiffened shell panel

The example of a stringer stiffened shell panel is used to demonstrate the applicability of the presented method for industry relevant structures, cf. Figure 6.7. The surface of the panel was modeled with a solid-like shell patch while the stiffeners were modeled as Kirchhoff-Love shell patches. The panel surface was discretized with  $16 \times 16 \times 1$  elements and a quartic polynomial degree was chosen in the solid shell in-plane directions and a quadratic degree was used in thickness direction. The stringer stiffeners were discretized with  $16 \times 26$  elements, with a polynomial degree  $p^1 = p^2 = 4$ . We used empirically chosen stability constants  $C_S = C_N = 80$  to ensure a reliable coupling between stiffener and shell surface. The frequency anal-

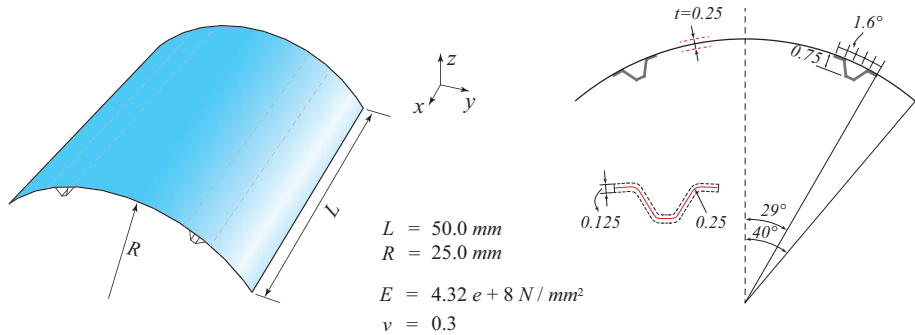


Figure 6.7: Model of a stringer stiffened panel.

ysis was performed for a free and undamped system with a row-sum lumped mass matrix. The mode shapes of the first three non-zero frequencies are shown in Figure 6.8. The mode shapes and the frequencies were verified using an ABAQUS reference model. Our model reproduced the mode shapes of the reference solution with slightly deviating frequencies which we attribute to the simplified cross-section modeling of

the stringer stiffeners of the ABAQUS reference model. The first modes corresponding to the smallest eigenvalues show torsion and bending of the significantly weaker shell surface compared to the stiffeners. All modes depicted in Figure 6.8 show the expected symmetry and asymmetry axes according to the symmetry in the patch geometry.

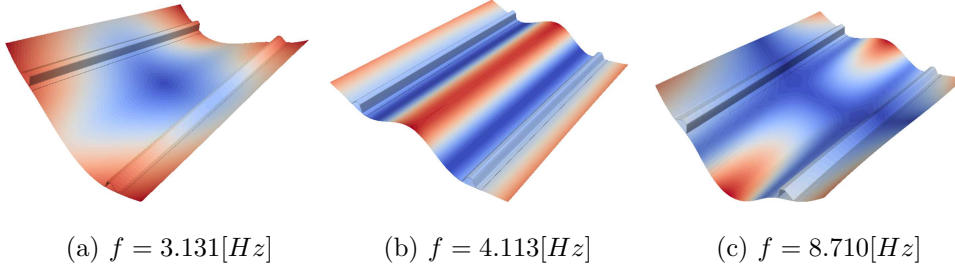


Figure 6.8: Stringer stiffened panel: mode shapes of lowest non-zero frequencies.

#### 6.2.4 Laminated plate with hole: free edge analysis

In this example, the laminated composite plate with a centrally located hole of section 3.4 is reconsidered. The plate was modeled with four layers with ply thickness equals to  $t_{ply} = 0.125mm$  and with dimensions and material properties as given in section 3.4. Material failure such as delamination is more likely to initiate around the hole due to free edge effects, while the remaining domain is relatively resistant. The blended patch concept was adopted here to capture the complete state of stress around the hole. The plate was modeled as a Kirchhoff-Love patch using classical lamina theory while a layerwise patch was used in the vicinity of the hole, cf. Figure 6.9 (a). Two different models were considered: the model depicted in Figure 6.9 (b) uses three Kirchhoff-Love patches to describe exactly the geometry of the thin plate domain. The three patches were discretized with  $8 \times 8$  elements for patch 1 and  $16 \times 8$  elements for patches 2 and 3, respectively. The model shown in Figure 6.9 (c) uses a trimmed single patch with  $17 \times 16$  elements to represent the thin plate domain. All Kirchhoff-Love patches use polynomial degrees  $p^1 = p^2 = 4$ . The layerwise model patch around the hole was chosen with a radial dimension  $L_1 = 2.5mm$ . Larger values for  $L_1$  were used but did not show any effect on the solution quality. The layerwise patch was discretized with  $10 \times 16$  elements for model 6.9 (b) and with  $11 \times 16$  elements for model 6.9 (c) and a polynomial degree  $p^1 = p^2 = 4$  in the in-plane direction. Through the thickness of the layerwise patch 4 and 8 elements of cubic polynomial were considered, respectively. We compare the blended models with a three-dimensional ABAQUS [187] finite element solution which was discretized with 20-node quadratic brick elements (*C3D20R*). The model data is summarized in table 6.1, where IGA-BL(b)-4 and IGA-BL(c)-8 refer to the blended coupling model shown in Figure 6.9 (b) and 6.9 (c) with 4 and 8 elements through the thickness,

respectively.

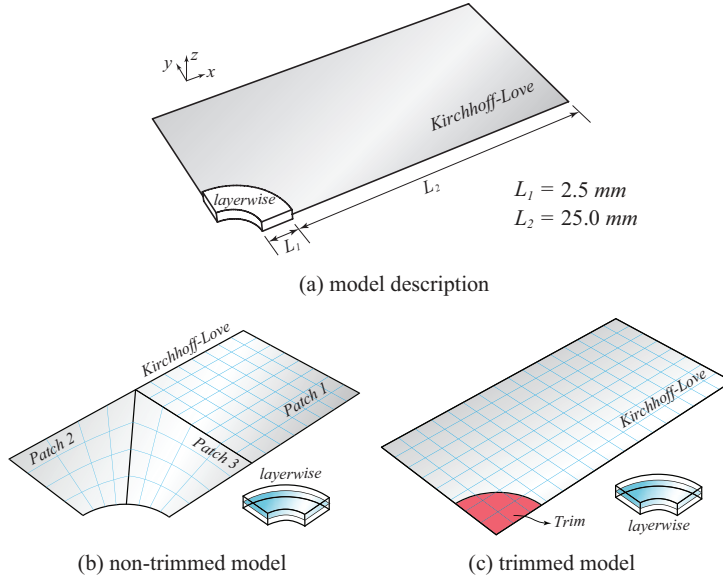


Figure 6.9: Blended coupling of laminated composite plate with hole: (a) model illustration, (b) blended coupling model of layerwise shell with non-trimming Kirchhoff-Love patches, (c) blended coupling of layerwise shell with trimmed Kirchhoff-Love shell patch.

Table 6.1: Used model data: ABAQUS reference model and IGA blended coupling model.

model	no elements	$(p^1, p^2, p^3)$ -degree	no degrees of freedom
ABAQUS	50160	2, 2, 2	643077
IGA-BL(b)-4	4264	4, 4, 3	12792
IGA-BL(b)-8	5384	4, 4, 3	16152
IGA-BL(c)-4	4320	4, 4, 3	12960
IGA-BL(c)-8	5520	4, 4, 3	16560

A comparison of the transverse stresses along the circular hole of the three models is shown in Figure 6.10. The stresses are evaluated in a distance of  $(r - R)/R = 0.001$  around the circular hole and at the lower  $[90^\circ/0^\circ]$  interface which is opposite to the previous example of section 3.4. We used one element through the thickness of each layer to evaluate  $\sigma_z$  for the two blended coupling models IGA-BL(b)-4 and IGA-BL(c)-4. For the evaluation of  $\sigma_{xz}$  and  $\sigma_{yz}$ , two elements per layer were used in both models. It was observed that, the transverse stresses of both blended coupling

models were in an overall good agreement with the reference ABAQUS solution showing smooth stress curves, however, even for the more refined IGA-BL-8 model, the number of elements and degrees of freedom of the IGA models are far less than the ABAQUS models. It is also worth to note that the model refinement, in particular the doubling of elements through the thickness, results only in a moderate increase ( $< 30\%$ ) of degrees of freedom which is attributed to the inherent overlapping support of NURBS basis functions. In addition, using the finite cell method, three coupled Kirchhoff-Love shell patches in Figure 6.9 (b) can be replaced with single trimmed patch, which facilitates the modeling efforts on the one hand, while on the other, the good agreement of the transverse stresses are maintained.

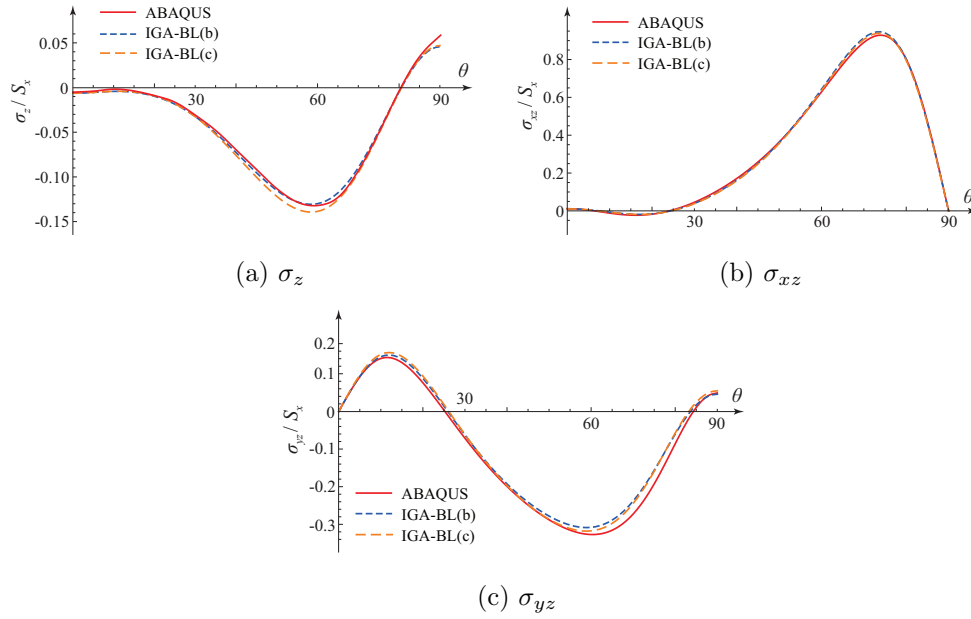


Figure 6.10: Plate with hole - comparisons of transverse stresses with different models: (a)  $\sigma_z$ , (b)  $\sigma_{xz}$ , (c)  $\sigma_{yz}$ .

## 6.2.5 Stiffened cylinder panel with opening

The applicability of the proposed blended coupling approach is shown for a stiffened cylinder panel with a circular opening. The geometry of the model is shown in Figure 6.11 (a) where the thickness of the cylinder skin and the stiffeners are  $t_{skin} = 0.5 \text{ mm}$  and  $t_{stiff} = 0.1 \text{ mm}$ , respectively. The stacking sequence of the cylinder is  $[90^\circ/0^\circ/90^\circ]$  with a  $0^\circ$  fiber angle parallel to the longitudinal direction of the cylinder ( $\xi_1$ ). The two stiffeners have a  $[0^\circ/90^\circ]_s$  stacking sequence with  $0^\circ$  and  $90^\circ$  fiber angles corresponding to the directions ( $\xi_1$ ) and ( $\xi_2$ ), respectively. The material properties of the laminate were chosen according to the example of sub-section 3.4.

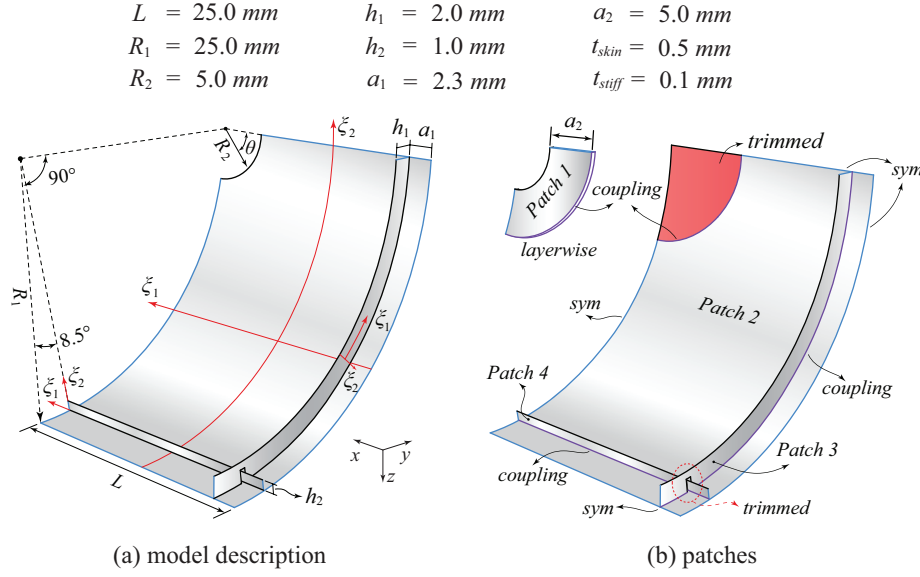


Figure 6.11: Geometry description of the cylinder with hole and stiffeners (a), four patch model (b).

The cylinder was subjected to an inner pressure load of  $\bar{p} = 1.0 \text{ N/mm}^2$ . Symmetry boundary conditions were applied along the longitudinal direction and along the symmetry axis, shown with blue curves in Figure 6.11. In order to capture the three dimensional stresses better around the free edge of the hole, we replaced a sub-domain around the hole with a layerwise shell patch, cf. Figure 6.11 (b). The radial patch dimension was chosen to be  $a_2 = 5.0 \text{ mm}$ . The analysis model was assembled from four patches: one cylinder, two stiffeners, and a layerwise patch. The cylinder was trimmed around the hole to fit with the coupling boundary of the layerwise patch. Equivalently, the crossing of the two stiffeners was modeled with a trimmed cut-out, cf. Figure 6.11 (b). The layerwise patch was discretized with  $19 \times 32$  elements in the in-plane direction with polynomial degrees  $p^1 = p^2 = 4$ . Through the thickness of the cylinder, 3 elements with  $p^3 = 3$  and 6 elements with  $p^3 = 2$  were tested, respectively. The cylinder, the circular and longitudinal stiffeners were discretized with  $24 \times 32$ ,  $16 \times 2$  and  $16 \times 2$  elements, respectively, with  $p^1 = p^2 = 4$ . A reference solution was obtained from an ABAQUS [187] model which used quadratic brick (*C3D20R*) elements and shell elements (*S8R*). The details of the model data are shown in table 6.2. The stabilization parameters of the Nitsche coupling were derived from an element-wise solution of the generalized eigenvalue problem (6.10). As demonstrated already in [104, 113] the computed stability values vary with the physical domain share of the trimmed element. With a decreasing share of the physical domain contributing to the element domain the stability values increase. An empirically chosen threshold value for the stability values was set to  $\sqrt[3]{E(p+1)}$

to prevent a degeneration of the formulation to a pure penalty approach. For the circular cut elements the stability values were in the range between  $8.0 \times 10^5$  and  $7.8 \times 10^6$ , and stayed below the threshold. A comparison of the transverse stresses

Table 6.2: Model data, stiffened panel: ABAQUS reference model and IGA blended coupling model of cylinder with hole and stiffener problem.

model	no elements	$(p^1, p^2, p^3)$ -degree	no degrees of freedom
ABAQUS	63151	2, 2, 2	811966
IGA-BL-3	2656	4, 4, 3	28584
IGA-BL-6	4480	4, 4, 2	28584

along the circular cut-out is shown for the two analysis models in Figure 6.12. The depicted stress components were evaluated along the rim of the circular cut-out at the  $[90^\circ/0^\circ]$  layer interface. In Figure 6.12 (a) and (b), respectively, the transverse shear stress  $\sigma_{23}$  and the transverse normal stress  $\sigma_{33}$  of the IGA-BL-3 and IGA-BL-6 is shown. The comparison of the transverse shear stress  $\sigma_{23}$  with the significantly more refined ABAQUS solution showed an overall good agreement of the two models. In contrast, the transverse normal stress  $\sigma_{33}$  showed a significant discrepancy within the domain between  $0^\circ$ - $40^\circ$ . The reason for this discrepancy can be attributed to the model differences between the ABAQUS model and the IGA models. In particular, the stiffeners were identified as the critical components, as demonstrated in the following. The blended isogeometric model coupled the stiffeners to the mid-surface according to the model properties of Kirchhoff-Love. the ABAQUS model was a three-dimensional continuum model where the stiffeners were coupled to the lower surface of the solid cylinder. Removing the stiffeners from both models clearly revealed their influence. The IGA-solution for the unstiffened panel was in very good agreement with the solution of the ABAQUS model as shown in Figure 6.13. It is noteworthy that the total degrees-of-freedom of the ABAQUS reference model was almost 30 times larger than the number of degrees-of-freedom for the blended coupling model.

### 6.3 Summary

In this chapter, Nitsche's method was used to couple thin shell patches and solid-like shell patches within the isogeometric analysis framework. We presented a variationally consistent extension of the principle of virtual work for blended shell models assembled from Kirchhoff-Love and solid-like patches and extended to the coupling of laminated composite shells. We revealed the method's potential to enrich locally Kirchhoff-Love models with solid sub-models to profit from the full three-dimensional stress state in highest quality. Such blended models are of interest in engineering practice and are of special relevance in e.g. the field of laminated composite structures. Using a blended pinched cylinder example we illustrated excellent properties

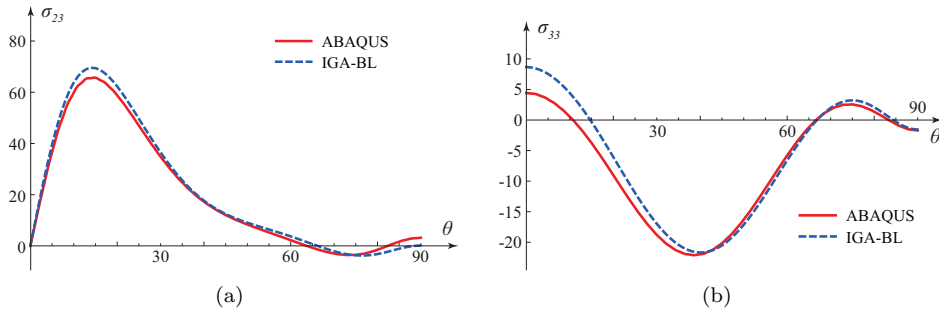


Figure 6.12: Stiffened panel - comparisons of transverse stresses with different models: (a)  $\sigma_{23}$ , (b)  $\sigma_{33}$ .

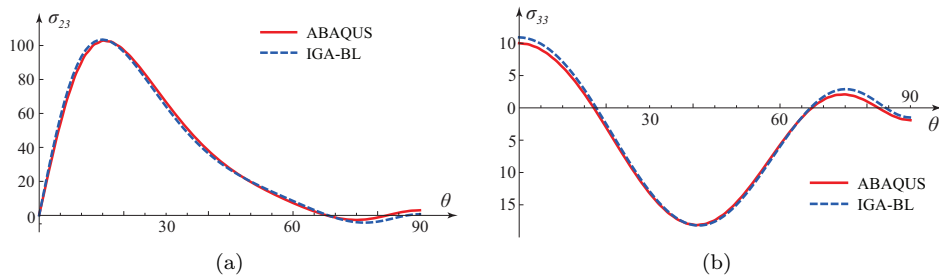


Figure 6.13: Stiffened panel - comparisons of transverse stresses with different models: (a)  $\sigma_{23}$ , (b)  $\sigma_{33}$ .

in terms of convergence and accuracy of the results. A similar solution quality was observed for a blended Scordelis-Lo model with smooth and accurate transverse shear stresses. An inevitable stabilization of the weak coupling method was ensured on the basis of ad-hoc choices for the two free parameters to demonstrate its high robustness. None of the examples required additional studies on optimal stability values to ensure a sufficiently high solution quality. Using a stringer stiffened panel, a frequency analysis was performed to demonstrate the applicability of the blended coupling approach for different type of analysis.

For the blended coupling of laminated composite shell structures, a laminated plate with hole and a stiffened cylinder panel were studied. The stabilization constants needed to ensure ellipticity of the coupled problem were estimated using the element-wise partial solution of an eigenvalue problem. We revealed the accuracy of the coupling method for the evaluation of curved free edge stresses around the hole. Compared to a ABAQUS reference solution, the blended model needs far fewer degrees-of-freedom than the reference while maintaining an overall equivalent quality of the stress results.

# Chapter 7

## Conclusions and future work

### 7.1 Summary

The work presented in this thesis was aimed at improving the modeling and analysis of thin-walled laminate composite structures in the framework of isogeometric methods. To this end two major aspects were highlighted throughout the thesis: under the aspect of an efficient through-the-thickness modeling of laminate composites the capacity of NURBS was considered and systematically tested, including linear stress, ply interface and buckling analysis. Under the aspect of highly performant analyses of engineering-relevant structures an essential part of the thesis was dedicated to the coupling of thin-walled, trimmed multi-patch shell structures to offer a suitable solution approach for one of the most prevalent challenges in isogeometric analysis.

The main developments and results are summarized as follows:

- a displacement-based isogeometric layerwise method for laminated composite was developed, tested and discussed. The method was able to capture accurately transverse shear and normal stresses in laminate composite structures. In combination with the finite cell method the proposed layerwise model handled efficiently trimmed NURBS geometries as they commonly appear in CAD-derived models. The combined approach demonstrated a highest degree of flexibility in terms of modeling and provided highly accurate stress components, even along free and trimmed edges.
- in comparison with equivalent-single-layer methods the layerwise approach provided the complete three-dimensional stress state, excels by a highest level of accuracy but is computationally more expensive. Therefore, a focus of this thesis was the combination of the two methods to profit from both, a computationally efficient, flexible analysis model for laminate composites and a model which allows insight into the complete state of stresses in critical, locally

bounded sub-domains. A strong coupling on the basis of boundary degrees of freedom of adjacent sub-domains was chosen for the analysis of cylindrical bending states of laminate composite plates. It was shown that a small layer-wise sub-domain was sufficient to receive transverse shear and normal stresses with high accuracy. The method was further extended to a model pre-existing delamination.

- the layerwise approach was applied to linear buckling analyses of delaminated laminates. Physically inadmissible buckling states of overlapping plies were suppressed by a normal contact model which repaired the penetration problem in a stepwise manner. Within a few iteration steps the physically meaningful and relevant buckling states were recovered.
- the special importance of thin-walled structures in aerospace engineering was also central to this thesis with regard to flexible, reliable and accurate NURBS modeling. Thin-walled structures are often modeled as Kirchhoff-Love-type thin-shells which manifold profit from the higher continuity and higher order approximation properties of NURBS in the isogeometric framework. A Nitsche-type extension to a rotation-free Kirchhoff-Love shell model was developed which satisfies essential boundary condition weakly. Thus, the non-interpolatory NURBS and trimmed-domain boundary was handled independent of the domain interpolation. Both, constrained translatory and rotational kinematics were reliably enforced without the need for additional degrees of freedom.
- the Nitsche formulation used to enforce essential boundary conditions weakly was extended to a coupling scheme for multi-patch shell models. The interpolation character of NURBS does not provide the indispensable continuity properties of the Kirchhoff-Love theory across patch interfaces with severe consequences for the kinematics and statics of strongly coupled shell structures. The developed coupling approach overcame these problems satisfying both, continuity and compatibility conditions, in an integral sense. With a carefully chosen stabilization approach the coupling method retained the algebraic properties of single-patch problems and provided the overall smoothness properties of NURBS across the interface without showing any discontinuity in displacements and stresses.
- a blended coupling of Kirchhoff-Love-type and solid-type shell patches used the weak coupling idea to allow a local enrichment of thin-shell models with stress components equivalent to a three-dimensional continuum shell theory. In particular, the blended coupling was a necessary step for a multi-lamina-model shell coupling including classical lamination theory and a layerwise theory to combine computational efficiency and highest model accuracy in regions of interest.

The developments presented in this thesis were tested with benchmark problems and with problems of practical relevance from engineering practice. A major aspect

considered in all tests was the performance of the development in terms of accuracy and reliability and in terms of convergence properties and modeling flexibility. The main findings and conclusions can be summarized as follows:

- in equivalent-single-layer methods, the strain field is assumed to be continuous through the thickness which results in a discontinuous stress field at the layer interface. In contrast, the proposed isogeometric layerwise method uses  $C^0$ -continuous B-spline functions through the thickness to account for the material discontinuities at ply interfaces and allows for a significantly more accurate representation of the complete stress state. Knot-insertion was found to be a simple mechanism to control the required continuity property at the ply level. The presented test results confirmed the superiority of the NURBS functions compared to a standard Lagrange basis with regard to convergence of the stress components to the analytical reference solution.
- the finite cell method, used to model trimmed domains, significantly reduced model complexity and prevented the need for a domain reparametrization to capture parametrically the desired solution domain. The test results revealed accurate displacement and stress results at the ply interface along trimmed edges. A comparison of transverse stresses with a classical finite element model confirmed the efficiency and accuracy of the proposed method. A similar solution quality was observed for an IGA model size of almost one order of magnitude fewer degrees of freedom.
- The mutual influence domain of the different models was tested using the strong coupling of equivalent single layer and layerwise patches. The study provided the dimensions of the layerwise patch needed to provide stress results which are sufficiently close to a given analytic reference solution. The coupling approach was extended to investigate laminates with pre-existing delaminations. A layerwise model with delamination was easily obtained by  $(p + 1)$ -fold knot insertion at the layer interface to generate discontinuous displacements.
- linear buckling was studied with several multi-patch models for laminated composite plate-like structures with pre-existing delamination zones showing good convergence of the buckling load under uniform p-refinement. It was further demonstrated that a contact algorithm can be successfully used to repair step-wise inadmissible buckling states with overlapping plies. Several benchmark problems demonstrated that the approach is capable to reproduce reliably the finite-element reference solutions reported in literature, even for multiple delaminated plies. A detailed study on the influence of size and position of the delamination zone with regard to the final buckling load and buckling shape revealed the basic model sensitivity.
- the weak enforcement of essential boundary conditions and coupling constraints was demonstrated with several examples. The Nitsche formulation is variationally consistent but requires a penalty-like stabilization to ensure coercivity. For optimal convergence properties the stability parameters were chosen propor-

tional to the material properties and element diameter. A remaining constant in the stability parameters, which depend on the order of applied approximation space was approximated by the partial solution of a generalized eigenvalue problem. It was further shown in the majority of examples that in many cases a wide range for an empirical selection of this constant exists which ensures optimal convergence rates.

- for the presented shell problems we showed highest smoothness and continuity across the coupling interfaces in terms of displacements and, in particular, in terms of stresses. The weak coupling approach for Kirchhoff-Love shells considered in addition transverse shear stresses which ensured kinematic compatibility and which removed completely a *hinge effect* among  $C^0$ -continuous coupled patches. The bending moments and stress resultants of all examples showed highest smoothness across the coupling interface. In addition, the coupling approach was successfully applied to folded shell problems and retained accurately the angle of the fold during deformation. The applicability of the Nitsche approach to reliably enforce boundary and coupling constraints was illustrated with a stress analysis of a trimmed, non-conforming multi-patch pipe problem and a frequency analysis for a stringer stiffened panes for which in both cases excellent results were achieved.
- using the example of a trimmed multi-model laminated plate with a hole and a stiffened cylinder with a hole, the practical relevance for aerospace engineering problems was demonstrated. In a comparison with a finite element reference solution the developed multi-patch and multi-model modeling and analysis platform outperformed the reference model on a degree-of-freedom basis with comparable analysis results

Isogeometric analysis has been proven, throughout the thesis, that it is a suitable competitor to the well-established finite element method in terms of accuracy and convergence properties. It outperforms finite element solutions in many respects, in particular, where the high-order continuity and high-order approximation properties become dominant as demonstrated for the multi-patch analysis of thin shells. Still, a limiting factor exists in terms of modeling of large-scale multi-patch models including non-conforming discretizations and trimming. This thesis was intended as a contribution to relax the modeling difficulties of isogeometric analysis and to contribute to a better and more flexible modeling pipeline for the future. Furthermore, the thesis sheds light on the applicability of isogeometric analysis for laminate composite models in aerospace engineering and beyond.

## 7.2 Future work

The modeling aspects of isogeometric analysis were found to be a major challenge and is a problem that requests more attention in the future to provide a competitive analysis framework for industry relevant models compared to established methods.

Modeling aspects also dominated the work of this thesis which provided functional solutions and suitable directions for further development. Based on the developments discussed in this thesis the following topics would prove very interesting for future research.

### Geometric nonlinear deformation and buckling of shell structures

The developments discussed in this thesis concentrated on problems of linear elasticity, however, geometric nonlinearity is central to thin shell problems and should be addressed with regard to the presented weak coupling approach. One of the major challenges of the weak coupling formulation for nonlinear problems is the derivation and implementation of the covariant derivatives of the corresponding moment and force stress resultants of the shell. Compared to the linear case, a consistent coupling extension results in a much larger number of additional terms which depend on current deformation state. The results of a first study presented here revealed stable and accurate numerical properties as demonstrated below.

A simple benchmark problem of a two-patch plate model subjected to an end shear force was studied. To keep the example simple the coupling interface was chosen to be a straight line and the coupled patches were conforming. The geometry description and material properties are shown in Figure 7.1. Both, the residual forces

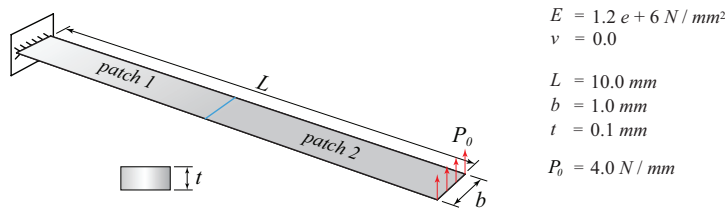


Figure 7.1: Cantilever plate problem under large deformation.

(5.26) and corresponding stiffness contributions (5.27) and the coupling extensions (5.73) depend nonlinearly on the current displacement state and are linearized for a stepwise iterative Newton-Raphson solution. A discretization of  $16 \times 2$  elements with cubic basis functions is used in this example. In Figure 7.2, the horizontal and vertical tip deflection of cantilever plate are plotted against the shear force and compared with the reference solutions [242]. The predicted deflection is in very good agreement with the reference solution. The solution converged within 5-7 iterations per step.

Using a geometric nonlinear coupling formulation the nonlinear buckling behavior of thin shells can be analysed. It is expected that the modeling of geometric imperfections especially will profit from the smoothness properties of NURBS representation, and used in combination with the finite cell method, the modeling of holes and cut-outs would be significantly facilitated.

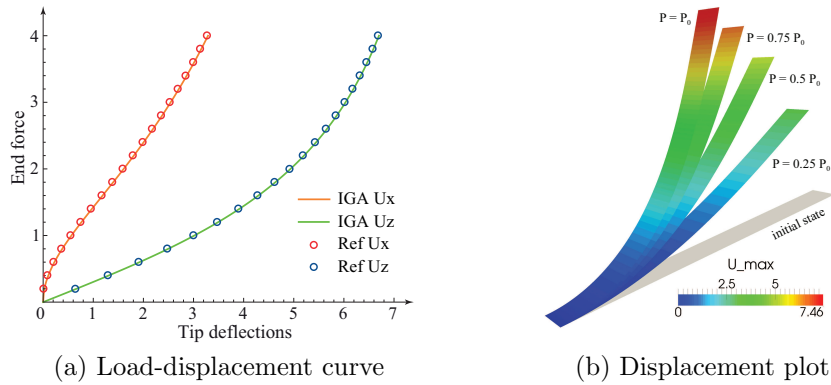


Figure 7.2: (a) Load-displacement plot at tip, (b) contour plot of displacement at equally four load steps.

### Damage prediction and propagation

Using the three-dimensional stress state provided by the layerwise approach and utilized in the blended coupling the door is open for the prediction of damage in large-scale models. In particular, the prediction of delamination is of major importance for laminate composites, and this would profit from the proposed combined multi-model approach. The existing framework can be easily extended to a cohesive zone model which is capable of predicting the initiation and propagation of delamination within a layerwise modeled sub-domain of large aerospace or wind energy wing models.

## Appendix A

# Derivatives of Kirchhoff-Love shell quantities w.r.t the displacement variables

The derivatives of Kirchhoff-Love's normal vector with respect to the displacement variables  $\mathbf{U}_r$  is written as:

$$\mathbf{a}_{3,r} = \frac{\hat{\mathbf{a}}_{3,r} \cdot \bar{\mathbf{a}}_3 - \hat{\mathbf{a}}_3 \cdot \bar{\mathbf{a}}_{3,r}}{\bar{a}_3^2} \quad (\text{A.1})$$

with:

$$\hat{\mathbf{a}}_3 = \mathbf{a}_1 \times \mathbf{a}_2 \quad (\text{A.2})$$

$$\hat{\mathbf{a}}_{3,r} = \mathbf{a}_{1,r} \times \mathbf{a}_2 + \mathbf{a}_1 \times \mathbf{a}_{2,r} \quad (\text{A.3})$$

$$\bar{a}_3 = |\mathbf{a}_1 \times \mathbf{a}_2| \quad (\text{A.4})$$

and:

$$\bar{a}_{3,r} = \frac{\hat{\mathbf{a}}_3 \cdot \hat{\mathbf{a}}_{3,r}}{\bar{a}_3} \quad (\text{A.5})$$

The membrane strain is defined in equation (5.4), and its derivative w.r.t. displacement variable  $\mathbf{U}_r$  is:

$$\varepsilon_{\alpha\beta,r} = \frac{\partial \varepsilon_{\alpha\beta}}{\partial \mathbf{U}_r} = \frac{1}{2}(a_{\alpha\beta} - A_{\alpha\beta})_{,r} = \frac{1}{2}a_{\alpha\beta,r} = \frac{1}{2}(\mathbf{a}_{\alpha,r} \cdot \mathbf{a}_\beta + \mathbf{a}_\alpha \cdot \mathbf{a}_{\beta,r}) \quad (\text{A.6})$$

where:

$$\mathbf{a}_{\alpha,r} = R_{,\alpha}^r \mathbf{e}_i \quad (\text{A.7})$$

---

where  $R_{,\alpha}^r$  is the first derivative of  $r$ -th shape function, and  $\mathbf{e}_i$  is the unit vector of Cartesian grid.

The derivatives of the bending strains (5.7) w.r.t. displacement variables  $\mathbf{U}_r$  are:

$$\kappa_{\alpha\beta,r} = (B_{\alpha\beta} - b_{\alpha\beta}),_r = -b_{\alpha\beta,r} = -(\mathbf{a}_{\alpha,\beta,r} \cdot \mathbf{a}_3 + \mathbf{a}_{\alpha,\beta} \cdot \mathbf{a}_{3,r}) \quad (\text{A.8})$$

where:

$$\mathbf{a}_{\alpha,\beta} = \sum_i R_{,\alpha\beta}^i \mathbf{u}_i \quad (\text{A.9})$$

$$\mathbf{a}_{\alpha,\beta,r} = R_{,\alpha\beta}^r \mathbf{e}_i \quad (\text{A.10})$$

Similarly, the derivatives of the force and moment stress resultants w.r.t. displacement variables are derived from equations (5.15), (5.16), (5.20) and (5.21).

# Bibliography

- [1] T.J.R. Hughes, J.A. Cottrell, and Y. Bazilevs. Isogeometric analysis: CAD, finite elements, NURBS, exact geometry and mesh refinement. *Computer Methods in Applied Mechanics and Engineering*, 194:4135–4195, 2005.
- [2] J. Kiendl, K.-U. Bletzinger, J. Linhard, and R. Wüchner. Isogeometric shell analysis with Kirchhoff-Love elements. *Computer Methods in Applied Mechanics and Engineering*, 198:3902–3914, 2009.
- [3] D.J. Benson, Y. Bazilevs, M.C. Hsu, and T.J.R. Hughes. Isogeometric shell analysis: the Reissner-Mindlin shell. *Computer Methods in Applied Mechanics and Engineering*, 199:276–289, 2010.
- [4] R. Echter, B. Oesterle, and M. Bischoff. A hierarchic family of isogeometric shell finite elements. *Computer Methods in Applied Mechanics and Engineering*, 254:170–180, 2013.
- [5] C.V. Verhoosel, M.A. Scott, R. de Borst, and T.J.R. Hughes. An isogeometric approach to cohesive zone modeling. *International Journal for Numerical Methods in Engineering*, 87:336–360, 2010.
- [6] C.V. Verhoosel, M.A. Scott, T.J.R. Hughes, and R. de Borst. An isogeometric analysis approach to gradient damage models. *International Journal for Numerical Methods in Engineering*, 86(1):115–134, 2011.
- [7] E. Luycker, D. J. Benson, T. Belytschko, Y. Bazilevs, and M.C. Hsu. X-FEM in isogeometric analysis for linear fracture mechanics. *International Journal for Numerical Methods in Engineering*, 87(6):541–565, 2011.
- [8] R. L. Taylor. Isogeometric analysis of nearly incompressible solids. *International Journal for Numerical Methods in Engineering*, 87(1-5):273–288, 2011.
- [9] R.N. Simpson, S.P.A. Bordas, H. Lian, and J. Trevelyan. An isogeometric boundary element method for elastostatic analysis: 2D implementation aspects. *Computers & Structures*, 118:2–12, 2013.
- [10] M. Borden, T.J.R. Hughes, C.M. Landis, and C.V. Verhoosel. A higher-order phase-field model for brittle fracture: Formulation and analysis within the

---

isogeometric analysis framework. *Computer Methods in Applied Mechanics and Engineering*, 273:100–118, 2014.

- [11] J.F. Caseiro, Valente R.A.F., A. Reali, J. Kiendl, F. Auricchio, and R.J. Alves de Sousa. On the assumed natural strain method to alleviate locking in solid-shell NURBS-based finite elements. *Computational Mechanics*, 53:1341–1353, 2014.
- [12] X. Deng, A. Korobenko, J. Yan, and Y. Bazilevs. Isogeometric analysis of continuum damage in rotation-free composite shells. *Computer Methods in Applied Mechanics and Engineering*, 284:349–372, 2015.
- [13] R. Bouclier, T. Elguedj, and A. Combescure. An isogeometric locking-free NURBS-based solid-shell element for geometrically nonlinear analysis. *International Journal for Numerical Methods in Engineering*, 101:774–808, 2015.
- [14] Y. Bazilevs, V.M. Calo, Y. Zhang, and T.J.R. Hughes. Isogeometric fluid-structure interaction analysis with applications to arterial blood flow. *Computational Mechanics*, 38:310–322, 2006.
- [15] Y. Zhang, Y. Bazilevs, S. Goswami, C. Bajaj, and T.J.R. Hughes. Patient-specific vascular nurbs modeling for isogeometric analysis of blood flow. *Computer Methods in Applied Mechanics and Engineering*, 196(29-30):2943–2959, 2007.
- [16] Y. Bazilevs and T.J.R. Hughes. NURBS-based isogeometric analysis for the computation of flows about rotating components. *Computational Mechanics*, 43:143–150, 2008.
- [17] Y. Bazilevs and A. Akkerman. Large eddy simulation of turbulent Taylor-Couette flow using isogeometric analysis and the residual-based variational multiscale method. *Journal of Computational Physics*, 229(9):3402–3414, 2010.
- [18] M. Hsu, I. Akkerman, and Y. Bazilevs. High-performance computing of wind turbine aerodynamics using isogeometric analysis. *Computers & Fluids*, 49(1):93–100, 2011.
- [19] M. Hsu, D. Kamensky, Y. Bazilevs, M.S. Sacks, and T.J.R. Hughes. Fluid-structure interaction analysis of bioprosthetic heart valves: significance of arterial wall deformation. *Computational Mechanics*, 54:1055–1071, 2014.
- [20] A. Tagliabue, L. Dedè, and A. Quarteroni. Isogeometric analysis and error estimates for high order partial differential equations in fluid dynamics. *Computers & Fluids*, 102:277–303, 2014.
- [21] D. Kamensky, M. Hsu, D. Schillinger, J.A. Evans, A. Aggarwal, Y. Bazilevs, M.S. Sacks, and T.J.R. Hughes. An immersogeometric variational framework for fluid-structure interaction: Application to bioprosthetic heart valves. *Computer Methods in Applied Mechanics and Engineering*, 284:1005–1053, 2015.

- 
- [22] J.A. Cottrell, A. Reali, Y. Bazilevs, and T.J.R. Hughes. Isogeometric analysis of structural vibrations. *Computer Methods in Applied Mechanics and Engineering*, 195 (41-43):5257–5296, 2006.
- [23] A. Reali. An isogeometric analysis approach for the study of structural vibrations. *Journal of Earthquake Engineering*, 10:1–30, 2006.
- [24] S. Shojaee, E. Izadpanah, N. Valizadeh, and J. Kiendl. Free vibration analysis of thin plates by using a NURBS-based isogeometric approach. *Finite Elements in Analysis and Design*, 61:23–34, 2012.
- [25] R. Dhote, H. Gomez, R. Melnik, and J. Zu. Isogeometric analysis of coupled thermo-mechanical phase-field models for shape memory alloys using distributed computing. *Procedia Computer Science*, 18:1068–1076, 2013.
- [26] M. Yoon, S. Ha, and S. Cho. Isogeometric shape design optimization of heat conduction problems. *International Journal of Heat and Mass Transfer*, 62:272–285, 2013.
- [27] H. Jari, H.R. Atri, and S. Shojaee. Nonlinear thermal analysis of functionally graded material plates using a NURBS based isogeometric approach. *Composite Structures*, 119:333–345, 2015.
- [28] Í. Temizer, P. Wriggers, and T.J.R Hughes. Contact treatment in isogeometric analysis with NURBS. *Computer Methods in Applied Mechanics and Engineering*, 200:1100–1112, 2011.
- [29] L. De Lorenzis, Í. Temizer, P. Wriggers, and G. Zavarise. A large deformation frictional contact formulation using NURBS-based isogeometric analysis. *International Journal for Numerical Methods in Engineering*, 87:1278–1300, 2011.
- [30] Í. Temizer, P. Wriggers, and T.J.R Hughes. Three-dimensional mortar-based frictional contact treatment in isogeometric analysis with NURBS. *Computer Methods in Applied Mechanics and Engineering*, 209-212:115–128, 2012.
- [31] L. De Lorenzis, P. Wriggers, and G. Zavarise. A mortar formulation for 3D large deformation contact using NURBS-based isogeometric analysis and the augmented Lagrangian method. *Computational Mechanics*, 49:1–20, 2012.
- [32] M.E. Matzen, T. Cichosz, and M. Bischoff. A point to segment contact formulation for isogeometric, NURBS based finite elements. *Computer Methods in Applied Mechanics and Engineering*, 255:27–39, 2013.
- [33] R. Dimitri, L.D. Lorenzis, M.A. Scott, P. Wriggers, R.L. Taylor, and G. Zavarise. Isogeometric large deformation frictionless contact using T-splines. *Computer Methods in Applied Mechanics and Engineering*, 269:394–414, 2014.

- 
- [34] A. Buffa, G. Sangalli, and R. Vázquez. Isogeometric analysis in electromagnetics: B-splines approximation. *Computer Methods in Applied Mechanics and Engineering*, 199(17-20):1143–1152, 2010.
- [35] P. Nrtoft, J. Gravesen, and M. Willatzen. Isogeometric analysis of sound propagation through laminar flow in 2-dimensional ducts. *Computer Methods in Applied Mechanics and Engineering*, 284:1098–1119, 2015.
- [36] R.N. Simpson, M.A. Scot, M. Taus, D.C. Thomas, and H. Lian. Acoustic isogeometric boundary element analysis. *Computer Methods in Applied Mechanics and Engineering*, 269:265–290, 2014.
- [37] W.A. Wall, M.A. Frenzel, and C. Cyron. Isogeometric structural shape optimization. *Computer Methods in Applied Mechanics and Engineering*, 197(33-40):2976–2988, 2008.
- [38] S. Cho and S. Ha. Isogeometric shape design optimization: exact geometry and enhanced sensitivity. *Structural and Multidisciplinary Optimization*, 38(1):53–70, 2009.
- [39] Y. Seo, H. Kim, and S. Youn. Shape optimization and its extension to topological design based on isogeometric analysis. *International Journal of Solids and Structures*, 47(11-12):1618–1640, 2010.
- [40] K. Li and X. Qian. Isogeometric analysis and shape optimization via boundary integral. *Computer-Aided Design*, 43(11):1427–1437, 2011.
- [41] D. Schillinger, L. Dedé, M.A. Scott, J.A. Evans, M.J. Borden, E. Rank, and T.J.R. Hughes. An isogeometric design-through-analysis methodology based on adaptive hierarchical refinement of NURBS, immersed boundary methods, and T-spline CAD surfaces. *Computer Methods in Applied Mechanics and Engineering*, 249-252:116–150, 2012.
- [42] N.J. Pagano. Exact solutions for composite laminates in cylindrical bending. *Journal of Composite Materials*, 3:398–411, 1969.
- [43] N.J. Pagano. Exact solutions for rectangular bidirectional composites and sandwich plates. *Journal of Composite Materials*, 4:20–34, 1970.
- [44] J.M. Whitney. Stress analysis of thick laminated composite and sandwich plates. *Journal of Composite Materials*, 6(4):426–440, 1972.
- [45] R.B. Pipes. Interlaminar stresses in composite laminates under uniform axial extension. *Journal of Composite Materials*, 4(4):538–548, 1970.
- [46] G.M. Kulikov and S.V. Plotnikova. Advanced formulation for laminated composite shells: 3D stress analysis and rigid-body motions. *Composite Structures*, 95:236–246, 2013.

- 
- [47] H.T. Wu and F. Chang. Transient dynamic analysis of laminated composite plates subjected to transverse impact. *Computers & Structures*, 31(3):453–466, 1989.
- [48] D.R. Mahapatra and S. Gopalakryshna. A spectral finite element model for analysis of axial-flexural-shear coupled wave propagation in laminated composite beams. *Composite Structures*, 59(1):67–88, 2003.
- [49] R.K. Kapania and S. Raciti. Recent advances in analysis of laminated beams and plates, part ii: Vibrations and wave propagation. *Composite Structures*, 27(7):935–946, 1989.
- [50] I. Mechab, B. Mechab, and S. Benaissa. Static and dynamic analysis of functionally graded plates using Four-variable refined plate theory by the new function. *Composites Part B: Engineering*, 45(1):748–757, 2013.
- [51] M. Savoia. Three-dimensional thermal analysis of laminated composite plates. *International Journal of Solids and Structures*, 32(5):593–608, 1995.
- [52] A.S.D. Wang. Edge effects on thermally induced stresses in composite laminates. *Journal of Composite Materials*, 11:300–312, 1977.
- [53] M. Tahani and A. Nosier. Free edge stress analysis of general cross-ply composite laminates under extension and thermal loading. *Composite Structures*, 60:91–103, 2003.
- [54] S. Brischetto and E. Carrera. Heat conduction and thermal analysis in multi-layered plates and shells. *Mechanics Research Communications*, 38(6):449–455, 2011.
- [55] F. Chang and K. Chang. A progressive damage model for laminated composites containing stress concentrations. *Journal of Composite Materials*, 21:834–855, 1987.
- [56] P.P. Camanho and F.L. Matthews. A progressive damage model for mechanically fastened joints in composite laminates. *Journal of Composite Materials*, 33(24):2248–2280, 1999.
- [57] H.Y. Choi and F. Chang. A model for predicting damage in graphite/epoxy laminated composites resulting from low-velocity point impact. *Journal of Composite Materials*, 26(14):2134–2169, 1992.
- [58] M.A. Caminero, M. Lopez-Pedrosa, C. Pinna, and C. Soutis. Damage monitoring and analysis of composite laminates with an open hole and adhesively bonded repairs using digital image correlation. *Composite Part B: Engineering*, 53:76–91, 2013.
- [59] K.L. Reifsnider and A. Talug. Analysis of fatigue damage in composite laminates. *International Journal of Fatigue*, 2(1):3–11, 1980.

- 
- [60] K.L. Reifsnider and R. Jamison. Fracture of fatigue-loaded composite laminates. *International Journal of Fatigue*, 4(4):187–197, 1982.
- [61] E. Persson, I. Eriksson, and L. Zackrisson. Effects of hole machining defects on strength and fatigue life of composite laminates. *Composites Part A: Applied Science and Manufacturing*, 28(2):141–151, 1997.
- [62] J. Zhang, L. Peng, L. Zhao, and B. Fei. Fatigue delamination growth rates and thresholds of composite laminates under mixed mode loading. *International Journal of Fatigue*, 40:7–15, 2012.
- [63] H. Chai, C.D. Babcock, and W.B. Knauss. One-dimensional modelling of failure in laminated plates by delamination buckling. *International Journal of Solids and Structures*, 17:1069–1083, 1981.
- [64] M.K. Yeh. Buckling of elliptically delaminated composite plates. *Journal of Composite Materials*, 28(1):36–52, 1994.
- [65] H. Gu and A. Chattopadhyay. Delamination buckling and postbuckling of composite cylindrical shells. *AIAA Journal*, 34(6):1279–1286, 1996.
- [66] C. Bisagni. Numerical analysis and experimental correlation of composite shell buckling and post-buckling. *Composites Part B: Engineering*, 31(8):655–667, 2000.
- [67] C. Bisagni. Dynamic buckling of fiber composite shells under impulsive axial compression. *Thin-Walled Structures*, 43(3):499–514, 2005.
- [68] G. Soremekun, Z. Gürdal, R.T. Haftka, and L.T. Watson. Composite laminate design optimization by genetic algorithm with generalized elitist selection. *Computers & Structures*, 79(2):131–143, 2001.
- [69] R.L. Riche and R.T. Haftka. Optimization of laminate stacking sequence for buckling load maximization by genetic algorithm. *AIAA Journal*, 31(5):951–956, 1993.
- [70] M.M. Abdalla, S. Setoodeh, and Z. Gürdal. Design of variable stiffness composite panels for maximum fundamental frequency using lamination parameters. *Composite Structures*, 81(2):283–291, 2007.
- [71] Z. Gürdal, B.F. Tatting, and C.K. Wu. Variable stiffness composite panels: Effects of stiffness variation on the in-plane and buckling response. *Composite Structures*, 39(5):911–922, 2008.
- [72] J. A. Cottrell, T. J. R. Hughes, and Y. Bazilevs. *Isogeometric analysis: Towards Integration of CAD and FEM*. John Wiley & Sons, 2009.
- [73] C.H. Thai, L.V. Tran, D.T. Tran, T. Nguyen-Thoi, and H. Nguyen-Xuan. Analysis of laminated composite plates using higher-order shear deformation plate theory and node-based smoothed discrete shear gap method. *Applied Mathematical Modelling*, 36:5657–5677, 2012.

- 
- [74] Chien H. Thai, A. J. M. Ferreira, E. Carrera, and H. Nguyen-Xuan. Isogeometric analysis of laminated composite and sandwich plates using a layerwise deformation theory. *Composite Structures*, 104:196–214, 2013.
- [75] Chien H. Thai, A. J. M. Ferreira, S. P. A. Bordas, T. Rabczuk, and H. Nguyen-Xuan. Isogeometric analysis of laminated composite and sandwich plates using a new inverse trigonometric shear deformation theory. *European Journal of Mechanics A/Solids*, 43:89–108, 2014.
- [76] S. Hosseini, J.J.C. Remmers, C.V. Verhoosel, and R.D. Borst. An isogeometric continuum shell element for nonlinear analysis. *Computer Methods in Applied Mechanics and Engineering*, 271:1–22, 2014.
- [77] Loc V. Tran, Chien H. Thai, Hien T. Le, Buntara S. Gan, Jaehong Lee, and H. Nguyen-Xuan. Isogeometric analysis of laminated composite plates based on a four-variable refined plate theory. *Engineering Analysis with Boundary Elements*, 47:68–81, 2014.
- [78] Y. Guo, A.P. Nagy, and Z. Gürdal. A layerwise theory for laminated composites in the framework of isogeometric analysis. *Composite Structures*, 107:447–457, 2014.
- [79] Chien H. Thai, H. Nguyen-Xuan, N. Nguyen-Thanh, T-H. Le, T. Nguyen-Thoi, and T. Rabczuk. Static, free vibration, and buckling analysis of laminated composite Reissner-Mindlin plates using NURBS-based isogeometric approach. *International Journal for Numerical Methods in Engineering*, 91:571–603, 2012.
- [80] S. Shojaee, N. Valizadeh, E. Izadpanah, T. Bui, and T. Vu. Free vibration and buckling analysis of laminated composite plates using the NURBS-based isogeometric finite element method. *Composite Structures*, 94:1677–1693, 2012.
- [81] Anh-Tuan Luu, Nam-Il Kim, and Jaehong Lee. NURBS-based isogeometric vibration analysis of generally laminated deep curved beams with variable curvature. *Composite Structures*, 119:150–165, 2015.
- [82] H. Kapoor and R.K. Kapania. Geometrically nonlinear NURBS isogeometric finite element analysis of laminated composite plates. *Composite Structures*, 94:3434–3447, 2012.
- [83] Tuan Le-Manh and Jaehong Lee. Postbuckling of laminated composite plates using NURBS-based isogeometric analysis. *Composite Structures*, 109:286–293, 2014.
- [84] Y. Guo and M. Ruess. A layerwise isogeometric approach for NURBS-derived laminate composite shells. *Composite Structures*, 124:300–309, 2015.
- [85] H. Kapoor, R.K. Kapania, and S.R. Soni. Interlaminar stress calculation in composite and sandwich plates in NURBS isogeometric finite element analysis. *Composite Structures*, 106:537–548, 2013.

- 
- [86] Vinh Phu Nguyen, Pierre Kerfriden, and Stéphane P. A. Bordas. Two- and three-dimensional isogeometric cohesive elements for composite delamination analysis. *Composites Part B: Engineering*, 60:193–212, 2014.
- [87] A.P. Nagy, S.T. IJsselmuiden, and M.M. Abdalla. Isogeometric design of anisotropic shells: optimal form and material distribution. *Computer Methods in Applied Mechanics and Engineering*, 264:145–162, 2013.
- [88] Tuan Le-Manh and Jaehong Lee. Stacking sequence optimization for maximum strengths of laminated composite plates using genetic algorithm and isogeometric analysis. *Composite Structures*, 116:357–363, 2014.
- [89] Manudha T. Herath, S. Natarajan, B. Gangadhara Prusty, and Nigel St. John. Isogeometric analysis and genetic algorithm for shape-adaptive composite marine propellers. *Computer Methods in Applied Mechanics and Engineering*, 284:835–860, 2015.
- [90] J.A. Cottrell, T.J.R. Hughes, and A. Reali. Studies of refinement and continuity in isogeometric structural analysis. *Computer Methods in Applied Mechanics and Engineering*, 196:4160–4183, 2007.
- [91] I. Babuška. The finite element method with penalty. *Mathematics of Computation*, 27(122):221–228, 1973.
- [92] T. Zhu and S.N. Atluri. A modified collocation method and a penalty formulation for enforcing the essential boundary conditions in the element free Galerkin method. *Computational Mechanics*, 21:211–222, 1998.
- [93] M. Breitenberger, A. Apostolatos, B. Philipp, R. Wüchner, and K.-U. Bletzinger. Analysis in computer aided design: Nonlinear isogeometric b-rep analysis of shell structures. *Computer Methods in Applied Mechanics and Engineering*, 284:401–457, 2015.
- [94] I. Babuška. The finite element method with Lagrangian multipliers. *Mathematics of Computation*, 20:179–192, 1973.
- [95] P. Hansbo, C. Lovadina, I. Perugia, and G. Sangalli. A Lagrange multiplier method for the finite element solution of elliptic interface problems using non-matching meshes. *Numerische Mathematik*, 100(1):91–115, 2005.
- [96] E. Burman and P. Hansbo. Fictitious domain finite element methods using cut elements: II. a stabilized Nitsche method. *Applied Numerical Mathematics*, 62(4):328–341, 2012.
- [97] A. Gerstenberger and W. Wall. An extended finite element method/Lagrange multiplier based approach for fluid-structure interaction. *Computer Methods in Applied Mechanics and Engineering*, 197:1699–1714, 2008.
- [98] W. Dornisch and S. Klinkel. Boundary conditions and multi-patch connections in isogeometric analysis. *Proceedings in Applied Mathematics and Mechanics*, 11:207–208, 2011.

- 
- [99] W. Dornisch, S. Klinkel, and G. Vitucci. Coupling of non-conforming NURBS patches with the weak substitution method. *Proceedings in Applied Mathematics and Mechanics*, 14:269–270, 2014.
- [100] W. Dornisch, G. Vitucci, and S. Klinkel. The weak substitution method - an application of the mortar method for patch coupling in nurbs-based isogeometric analysis. *International Journal for Numerical Methods in Engineering*, 103(3):205–234, 2015.
- [101] J. Nitsche. Über ein Variationsprinzip zur Lösung von Dirichlet Problemen bei Verwendung von Teilräumen, die keinen Randbedingungen unterworfen sind. *Abhandlung aus dem Mathematischen Seminar der Universität Hamburg*, 36:9–15, 1970.
- [102] M. Griebel and MA. Schweitzer. *A Particle-Partition of Unity Method. Part V: Boundary Conditions*. Springer-Verlag: Berlin, 2002.
- [103] P. Hansbo. Nitsche’s method for interface problems in computational mechanics. *GAMM Mitteilungen*, 28/2:183–206, 2005.
- [104] M. Ruess, D. Schillinger, Y. Bazilevs, V. Varduhn, and E. Rank. Weakly enforced essential boundary conditions for NURBS-embedded and trimmed NURBS geometries on the basis of the finite cell method. *International Journal for Numerical Methods in Engineering*, 95:811–846, 2013.
- [105] A. Embar, J. Dolbow, and I. Harari. Imposing Dirichlet boundary conditions with Nitsche’s method and spline-based finite elements. *International Journal for Numerical Methods in Engineering*, 83(7):877–898, 2010.
- [106] M. Ruess, D. Tal, N. Trabelsi, Z. Yosibash, and E. Rank. The finite cell method for bone simulations: verification and validation. *Biomechanics and Modeling in Mechanobiology*, 11(3-4):425–437, 2012.
- [107] N. Zander, S. Kollmannsberger, M. Ruess, Z. Yosibash, and E. Rank. The Finite Cell Method for linear thermoelasticity. *Computers & Mathematics with Applications*, 64(11):3527–3541, 2012.
- [108] C. D’Angelo and P. Zunino. Numerical approximation with Nitsche’s coupling of transient Stokes’/Darcy’s flow problems applied to hemodynamics. *Applied Numerical Mathematics*, 62:378–395, 2012.
- [109] S. Kollmannsberger, A. Özcan, J. Baiges, M. Ruess, E. Rank, and A. Reali. Parameter-free, weak imposition of dirichlet boundary conditions and coupling of trimmed and non-conforming patches. *International Journal for Numerical Methods in Engineering*, 101(9):670–699, 2015.
- [110] Y. Bazilevs, C. Michler, V.M. Calo, and T.J.R. Hughes. Weak Dirichlet boundary conditions for wall-bounded turbulent flows. *Computer Methods in Applied Mechanics and Engineering*, 196:4853–4862, 2007.

- 
- [111] Y. Bazilevs, C. Michler, V.M. Calo, and T.J.R. Hughes. Isogeometric variational multiscale modeling of wall-bounded turbulent flows with weakly-enforced boundary conditions on unstretched meshes. *Computer Methods in Applied Mechanics and Engineering*, 199:780–790, 2010.
- [112] A. Apostolatos, R. Schmidt, R. Wüchner, and K.-U. Bletzinger. A Nitsche-type formulation and comparison of the most common domain decomposition methods in isogeometric analysis. *International Journal for Numerical Methods in Engineering*, 97:473–504, 2014.
- [113] M. Ruess, D. Schillinger, A. I. Özcan, and E. Rank. Weak coupling for isogeometric analysis of non-matching and trimmed multi-patch geometries. *Computer Methods in Applied Mechanics and Engineering*, 269:46–71, 2014.
- [114] D. Schillinger, M.J. Borden, and H.K. Stolarski. Isogeometric collocation for phase-field fracture models. *Computer Methods in Applied Mechanics and Engineering*, 284:583–610, 2015.
- [115] J.D. Foley, A. van Dam, S.K. Feiner, and Hughes J. *Computer Graphics: Principles and Practice 2nd Edition in C*. Addison-Wesley, 1995.
- [116] J. Kiendl, Y. Bazilevs, M.-C. Hsu, R. Wüchner, and K.-U. Bletzinger. Isogeometric shell analysis with Kirchhoff-Love elements. *Computer Methods in Applied Mechanics and Engineering*, 199:2403–2416, 2010.
- [117] D.J. Benson, S. Hartmann, Y. Bazilevs, M.C. Hsu, and T.J.R. Hughes. Blended isogeometric shells. *Computer Methods in Applied Mechanics and Engineering*, 255:133–146, 2013.
- [118] W. Dornisch and S. Klinkel. Treatment of Reissner-Mindlin shells with kinks without the need for drilling rotation stabilization in an isogeometric framework. *Computer Methods in Applied Mechanics and Engineering*, 276:35–66, 2014.
- [119] H.-J. Kim, Y.-D. Seo, and S.-K. Youn. Isogeometric analysis for trimmed CAD surfaces. *Computer Methods in Applied Mechanics and Engineering*, 198:2982–2995, 2009.
- [120] R. Schmidt, R. Wüchner, and K.-U. Bletzinger. Isogeometric analysis of trimmed NURBS geometries. *Computer Methods in Applied Mechanics and Engineering*, 241-244:93–111, 2012.
- [121] D. Schillinger, M. Ruess, N. Zander, Y. Bazilevs, A. Düster, and E. Rank. Small and large deformation analysis with the p- and B-spline versions of the finite cell method. *Computational Mechanics*, 50:445–478, 2012.
- [122] E. Rank, M. Ruess, S. Kollmannsberger, D. Schillinger, and A. Düster. Geometric modeling, isogeometric analysis and the finite cell method. *Computer Methods in Applied Mechanics and Engineering*, 249-252:104–115, 2012.

- 
- [123] J. Parvizian, A. Düster, and E. Rank. Finite cell method - h- and p-extension for embedded domain problems in solid mechanics. *Computational Mechanics*, 41:121–133, 2007.
- [124] A. Düster, J. Parvizian, Z. Yang, and E. Rank. The finite cell method for three-dimensional problems of solid mechanics. *Computer Methods in Applied Mechanics and Engineering*, 197:3768–3782, 2008.
- [125] D. Schillinger, A. Düster, and E. Rank. The hp-d-adaptive finite cell method for geometrically nonlinear problems of solid mechanics. *International Journal for Numerical Methods in Engineering*, 89:1171–1202, 2012.
- [126] A.P. Nagy and D.J. Benson. On the numerical integration of trimmed isogeometric elements. *Computer Methods in Applied Mechanics and Engineering*, 284:165–185, 2015.
- [127] R. Glowinski and Y. Kuznetsov. Distributed Lagrange multipliers based on fictitious domain method for second order elliptic problems. *Computer Methods in Applied Mechanics and Engineering*, 196:1498–1506, 2007.
- [128] B. Flemisch and B. I. Wohlmuth. Stable Lagrange multipliers for quadrilateral meshes of curved interfaces in 3D. *Computer Methods in Applied Mechanics and Engineering*, 196(8):1589–1602, 2007.
- [129] A. Gerstenberger and W. A. Wall. An embedded Dirichlet formulation for 3D continua. *International Journal of Numerical Methods in Engineering*, 82:537–563, 2010.
- [130] E.A. Nasr and A.K. Kamrani. *Computer-Based Design and Manufacturing: An Information-Based Approach*. Springer, 2007.
- [131] E. Cohen, T. Martin, R.M. Kirby, T. Lyche, and R.F. Riesenfeld. Analysis-aware modeling: Understanding quality considerations in modeling for isogeometric analysis. *Computer Methods in Applied Mechanics and Engineering*, 199:334–356, 2010.
- [132] Y. Bazilevs, V.M. Calo, J.A. Cottrell, J.A. Evans, T.J.R. Hughes, S. Lipton, M.A. Scott, and T.W. Sederberg. Isogeometric analysis using T-splines. *Computer Methods in Applied Mechanics and Engineering*, 199:229–263, 2010.
- [133] I. Akkerman, Y. Bazilevs, V. M. Calo, T. J. R. Hughes, and S. Hulshoff. The role of continuity in residual-based variational multiscale modeling of turbulence. *Computational Mechanics*, 41(3):371–387, 2008.
- [134] J.A. Evans, Y. Bazilevs, I. Babuška, and T.J.R. Hughes. n-Widths, supinfs, and optimality ratios for the k-version of the isogeometric finite element method. *Computer Methods in Applied Mechanics and Engineering*, 198(21-26):1726–1741, 2009.
- [135] L. Piegl and W. Tiller. *The NURBS book - Monographs in Visual Communication*. Springer-Verlag Publishing Company, Inc., Heidelberg, 1997.

- 
- [136] K. Höllig. *Finite Element Methods with B-Splines*. Society for Industrial and Applied Mathematics, Philadelphia, 2003.
- [137] G. Farin. *Curves and Surfaces for Computer Aided Geometric Design*. Academic press, fourth edition, 1997.
- [138] A.P. Nagy. *Isogeometric Design Optimization*. Ph.D thesis. Delft University of Technology, 2011.
- [139] M. E. Gurtin. *An introduction to continuum mechanics*. Academic Press, 1981.
- [140] J. E. Marsden and T. J. R. Hughes. *Mathematical foundations of elasticity*. Dover Publishing Company, New York, 1994.
- [141] Y. Başar and D. Weichert. *Nonlinear continuum mechanics of solids*. Springer-Verlag Publishing Company, Heidelberg, 2000.
- [142] M. Bischoff, W.A. Wall, K.U. Bletzinger, and E. Ramm. Models and finite elements for thin-walled structures. In E. Stein, R. de Borst, and T.J.R. Hughes, editors, *Encyclopedia of Computational Mechanics*, pages 59–137. John Wiley & Sons, Ltd., New York, 2004.
- [143] flexiCAD. *Rhinoceros — NURBS modeling for Windows*. <http://www.de.rhino3d.com/>, 2011.
- [144] Autodesk. *Maya User’s Guide*. <http://http://www.autodesk.de/products/autodesk-maya/overview>, 2013.
- [145] Subodh Kumar and Dinesh Manocha. Efficient rendering of trimmed nurbs surfaces. *Computer-Aided Design*, 7:509–521, 1995.
- [146] D. Schillinger and M. Ruess. The finite cell method: A review in the context of higher-order structural analysis of cad and image-based geometric models. *Archives of Computational Methods in Engineering*, 22:391–455, 2015.
- [147] N. Zander, T. Bog, M. Elhaddad, R. Espinoza, H. Hu, A.F. Joly, C. Wu, P. Zerbe, A. Düster, S. Kollmannsberger, J. Parvizian, M. Ruess, D. Schillinger, and E. Rank. FCMLab: A Finite Cell Research Toolbox for MATLAB. *Advances in Engineering Software*, 74:49–63, 2014.
- [148] M. Ruess, V. Varduhn, Z. Yosibash, and E. Rank. A parallel high-order fictitious domain approach for biomechanical applications. In *Proc. ISPDC 2012-International Symposium on Parallel and Distributed Computing*, pages 279–285, 2012.
- [149] Z. Yang, S. Kollmannsberger, A. Duster, M. Ruess, E. Grande Garcia, R. Burgkart, and E. Rank. Non-standard bone simulation: Interactive numerical analysis by computational steering. *Computing and Visualization in Science*, 14(5):207–216, 2012.

- 
- [150] Z. Yang, M. Ruess, S. Kollmannsberger, A. Duster, and E. Rank. An efficient integration technique for the voxel-based finite cell method. *International Journal for Numerical Methods in Engineering*, 91:457–471, 2012.
- [151] C.V. Verhoosel, G.J. Zwieten, B. van Rietbergen, and R. de Borst. Image-based goal-oriented adaptive isogeometric analysis with application to the micro-mechanical modeling of trabecular bone. *Computer Methods in Applied Mechanics and Engineering*, 284:138–164, 2015.
- [152] C. Mittelstedt and W. Becker. Free-edge effects in composite laminates. *Applied Mechanics Reviews*, 60:217–245, 2007.
- [153] E. Carrera. Theories and finite elements for multilayered, anisotropic, composite plates and shells. *Archives of Computational Methods in Engineering*, 9(2):87–140, 2002.
- [154] J.N. Reddy. *Mechanics of laminated composite plates and shells*. CRC Press LLC, Boca Raton, 2004.
- [155] R. Rolfes, A.K. Noor, and H. Sparr. Evaluation of transverse thermal stresses in composite plates based on first-order shear deformation theory. *Computer Methods in Applied Mechanics and Engineering*, 167:355–368, 1998.
- [156] J.N. Reddy and Arciniega R.A. Shear deformation plate and shell theories: from Stavsky to present. *Mechanics of Advanced Materials and Structures*, 11:535–582, 2004.
- [157] J.N. Reddy. A simple higher-order theory for laminated composite plates. *Journal of Applied Mechanics*, 51:745–752, 1984.
- [158] J.N. Reddy and C.F. Liu. A higher-order shear deformation theory of laminated elastic shells. *International Journal of Engineering Science*, 23:319–330, 1985.
- [159] E. Carrera. Mixed layer-wise models for multilayered plates analysis. *Composite Structures*, 43:57–70, 1998.
- [160] E. Carrera. Multilayered shell theories accounting for layerwise mixed description, part 1: governing equations. *AIAA Journal*, 37:1107–1116, 1999.
- [161] E. Carrera. Multilayered shell theories accounting for layerwise mixed description, part 2: numerical evaluations. *AIAA Journal*, 37:1117–1124, 1999.
- [162] S. Srinivas. Refined analysis of laminated composites. *Journal of Sound and Vibration*, 30:495–507, 1973.
- [163] A. Nosier, R.K. Kapania, and J.N. Reddy. Free vibration analysis of laminated plates using a layer-wise theory. *AIAA Journal*, 31:2335–2346, 1993.
- [164] E.J. Barbero, J.N. Reddy, and J.L. Teply. General two-dimensional theory of laminated cylindrical shells. *AIAA Journal*, 28:544–553, 1990.

- 
- [165] E. Carrera. A class of two-dimensional theories for anisotropic multilayered plates analysis. *Accademia delle Scienze di Torino*, 19–20:1–39, 1995.
- [166] E. Carrera.  $c_z^0$  requirements - Models for the two dimensional analysis of multilayered structures. *Composite Structures*, 37:373–384, 1997.
- [167] T.M. Hsu and J.T.S. Wang. Rotationally symmetric vibrations of orthotropic layered cylindrical shells. *Journal of Sound and Vibration*, 16(4):473–487, 1971.
- [168] K.N. Cho, C.W. Bert, and A.G. Striz. Free vibrations of laminated rectangular plates analyzed by higher order individual-layer theory. *Journal of Sound and Vibration*, 145(3):429–442, 1991.
- [169] M Braun, M. Bischoff, and E. Ramm. Nonlinear shell formulations for complete three-dimensional constitutive laws including composite and laminates. *Computational Mechanics*, 15:1–18, 1994.
- [170] D.H. Robbins and J.N. Reddy. Modelling of thick composites using a layerwise laminate theory. *International Journal for Numerical Methods in Engineering*, 36:655–677, 1993.
- [171] J.N. Reddy. A generalization of two-dimensional theories of laminated composite plates. *Communications in Applied Numerical Methods*, 3:173–180, 1987.
- [172] J. Lee, Z. Gürdal, and O.H. Griffin. Layer-wise approach for the bifurcation problem in laminated composites with delaminations. *AIAA Journal*, 31(2):331–338, 1993.
- [173] E. Carrera. Theories and finite elements for multilayered plates and shells: A unified compact formulation with numerical assessment and benchmarking. *Archives of Computational Methods in Engineering*, 10(3):215–296, 2003.
- [174] H. Man, C. Song, T. Xiang, W. Gao, and F. Tin-Loi. High-order plate bending analysis based on the scaled boundary finite element method. *International Journal for Numerical Methods in Engineering*, 95(4):331–360, 2013.
- [175] T.K. Varadan and K. Bhaskar. Bending of laminated orthotropic cylindrical shells-an elasticity approach. *Composite Structures*, 17:141–156, 1991.
- [176] D. Schillinger, S.J. Hossain, and T.J.R. Hughes. Reduced bézier element quadrature rules for quadratic and cubic splines in isogeometric analysis. *Computer Methods in Applied Mechanics and Engineering*, 277:1–45, 2014.
- [177] R Byron and N.J. Pagano. Interlaminar stresses in composite laminates under uniform axial extension. *Journal of Composite Materials*, 4:538–548, 1970.
- [178] N.J. Pagano and R.B. Pipes. The influence of stacking sequence on laminate strength. *Journal of Composite Materials*, 5:50–57, 1971.

- 
- [179] A. Harris and O. Orringer. Investigation of angle-ply delamination specimen for interlaminar strength test. *Journal of Composite Materials*, 12:285–299, 1978.
- [180] I.S. Raju and JR. Crews, J.H. Interlaminar stress singularities at a straight free edge in composite laminates. *Computers and Structures*, 14:21–28, 1981.
- [181] C. Kassapoglou. Determination of interlaminar stresses in composite laminates under combined loads. *Journal of Reinforced Plastics and Composites*, 9:33–58, 1990.
- [182] E.F. Rybicki and D.W. Schmueser. Effect of stacking sequence and lay-up angle on free edge stresses around a hole in a laminated plate under tension. *Journal of Composite Materials*, 12:300–313, 1978.
- [183] C.C. Ko and C.C. Lin. Method for calculating the interlaminar stresses in symmetric laminates containing a circular hole. *AIAA Journal*, 30(1):197–204, 1992.
- [184] F.Z. Hu and Soutis C. Interlaminar stresses in composite laminates with a circular hole. *Composite Structures*, 37:223–232, 1997.
- [185] E.V. Iarve. Spline variational three dimensional stress analysis of laminated composite plates with open holes. *International Journal of Solids and Structures*, 33(14):2095–2118, 1996.
- [186] E.V. Iarve and N.J. Pagano. Singular full-field stresses in composite laminates with open holes. *International Journal of Solids and Structures*, 38:1–28, 2001.
- [187] Hibbit, Karlsson, and Sorensen. *ABAQUS/Standard Analysis User's Manual*. Hibbit, Karlsson, Sorensen Inc., USA, 2007.
- [188] L. Demasi and W. Yu. Assess the accuracy of the variational asymptotic plate and shell analysis (vapas) using the generalized unified formulation (guf). *Mechanics of Advanced Materials and Structures*, 20:227–241, 2013.
- [189] J.N. Reddy. An evaluation of equivalent-single-layer and layerwise theories of composite laminates. *Composite Structures*, 25:21–35, 1993.
- [190] J.D. Whitcomb and K. Woo. Application of iterative global/local finite element analysis. part 1: linear analysis. *Communications in Numerical Methods in Engineering*, 9(9):745–756, 1993.
- [191] J.D. Whitcomb and K. Woo. Application of iterative global/local finite element analysis. Part 2: geometrically non-linear analysis. *Communications in Numerical Methods in Engineering*, 9(9):757–766, 1993.
- [192] M.A. Aminpour, S.L. McCleary, and J.B. Ransom. A global/local analysis method for treating details in structural design. *Adaptive, Multilevel, and Hierarchical Computational Strategies*, A K Noor, Ed., 157:119–137, 1992.

- 
- [193] C.L. Liao, J.N. Reddy, and S.P. Engelstad. A solid-shell transition element for geometrically nonlinear analysis of composite structures. *International Journal for Numerical Methods in Engineering*, 26:1843–1854, 1988.
- [194] D.H. Robbins and J.N. Reddy. Global/local analysis of laminated composite plates using variable kinematic finite elements. In *Proceedings of the AIAA/ASME/ASCE/AHS/ASC 33rd Structures, Structural Dynamics, and Materials (SDM) Conference*, 1992.
- [195] M.A. Kouchakzadeh. Buckling analysis of rectangular laminated composite plates with an edge delamination under compressive load. *Journal of Aerospace Science and Technology*, 4:1–8, 2007.
- [196] D. Dash and B.N. Singh. Buckling and post-buckling of laminated composite plates. *Mechanics Research Communications*, 46:1–7, 2012.
- [197] K. Liang, M. Ruess, and M. Abdalla. The Koiter-Netwon approach using von Kármán kinematics for buckling analyses of imperfection sensitive structures. *Computer Methods in Applied Mechanics and Engineering*, 279:440–468, 2014.
- [198] G.J. Simiteses, S. Sallam, and W.L. Yin. Effect of delamination of axially loaded homogeneous laminated plates. *AIAA Journal*, 23:1437–1444, 1985.
- [199] S. Sallam and G.J. Simiteses. Delamination buckling and growth of flat, cross-ply laminates. *Composite Structures*, 4:361–381, 1985.
- [200] G.A. Kardomateas and D.W. Schmueser. Buckling and postbuckling of delaminated composites under compressive loads including transverse shear effects. *AIAA Journal*, 26:337–343, 1988.
- [201] H.P. Chen. Shear deformation theory for compressive delamination buckling and growth. *AIAA Journal*, 29:813–819, 1991.
- [202] E.J. Barbero and J.N. Reddy. Modeling of delamination in composite laminates using a layer-wise plate theory. *International Journal of Solids and Structures*, 28(3):373–388, 1991.
- [203] S.O. Peck and G.S. Springer. The behavior of delaminations in composite plates - analytically and experimental results. *Journal of Composite Materials*, 25:907–929, 1991.
- [204] H. Suemasu, K. Gozu, and K. Hayashi. Compressive buckling of rectangular composite plates with a free-edge delamination. *AIAA Journal*, 33:312–319, 1995.
- [205] H. Sekine, N. Hu, and M.A. Kouchakzadeh. Buckling analysis of elliptically delaminated composite laminates with consideration of partial closure of delamination. *Journal of Composite Materials*, 34:551–574, 2000.

- 
- [206] N. Hu. Buckling analysis of delaminated laminates with consideration of contact in buckling mode. *International Journal for Numerical Methods in Engineering*, 44:1457–1479, 1999.
- [207] J.N. Wook and J.N. Reddy. Delamination in cross-ply laminated beams using the layerwise theory. *Asian Journal of Civil Engineering (Building and Housing)*, 10(4):451–480, 2009.
- [208] K.J. Bathe. *Finite element procedures*. Prentice Hall, 1996.
- [209] P. Wriggers. *Computational contact mechanics*. Springer, Berlin, Heidelberg, 2006.
- [210] P. Wriggers. *Nonlinear Finite Element Methods*. Springer, Berlin, Heidelberg, 2008.
- [211] J. Lu. Isogeometric contact analysis: Geometric basis and formulation for frictionless contact. *Computer Methods in Applied Mechanics and Engineering*, 200:726–741, 2011.
- [212] B.A. Szabó. Estimation and control of error based on p convergence. In I. Babuška, O.C. Zienkiewicz, J. Gago, and E.R. de A. Olivera, editors, *Accuracy estimates and adaptive refinements in finite element computations*, pages 61–70. John Wiley & Sons, 1986.
- [213] S.S. Wang, N.M. Zahlan, and H. Suemasu. Compressive stability of delaminated random short-fiber composites, part II - experimental and analytical results. *Journal of Composite Materials*, 19:317–333, 1985.
- [214] Y. Guo and M. Ruess. Weak Dirichlet boundary conditions for trimmed thin isogeometric shells. *Computers and Mathematics with Applications*, 70:1425–1440, 2015.
- [215] F. Auricchio, L. Beirao da Veiga, A. Buffa, C. Lovadina, A. Reali, and G. Sangalli. A fully "locking-free" isogeometric approach for plane linear elasticity problems: A stream function formulation. *Computer Methods in Applied Mechanics and Engineering*, 197:160–172, 2007.
- [216] Y. Guo and M. Ruess. Nitsche's method for a coupling of isogeometric thin shells and blended shell structures. *Computer Methods in Applied Mechanics and Engineering*, 284:881–905, 2015.
- [217] Anita Hansbo and Peter Hansbo. An unfitted finite element method, based on Nitsche's method, for elliptic interface problems. *Computer Methods in Applied Mechanics and Engineering*, 191(47-48):5537–5552, 2002.
- [218] P.M. Naghdi. *Foundations of Elastic Shell Theory*. Applied mechanics. Institute of Engineering Research, University of California, 1962.

- 
- [219] M. Ruess. *Analysis-Controlled Design & Prognosis in the Framework of Higher Order Approximation*. Habilitation thesis. Technische Universität München, 2014.
- [220] P.G. Ciarlet. An introduction to differential geometry with applications to elasticity. *Journal of Elasticity*, 78(1-3):1–215, 2005.
- [221] P.J. Pahl and R. Damrath. *Mathematical Foundations of Computational Engineering*. Springer-Verlag Publishing Company, Inc., Heidelberg, 2001.
- [222] Y. Bazilevs and T.J.R. Hughes. Weak imposition of Dirichlet boundary conditions in fluid mechanics. *Computers and Fluids*, 36:12–26, 2007.
- [223] J.A. Evans and T.J.R. Hughes. Explicit trace inequalities for isogeometric analysis and parametric hexahedral finite elements. *Numerische Mathematik*, 123(2):259–290, 2013.
- [224] A.C. Scordelis and K.S. Lo. Computer analysis of cylindrical shells. *Journal of the American Concrete Institute*, 61:539–561, 1969.
- [225] T. Belytschko, H. Stolarski, W.K. Liu, N. Carpenter, and J.S.-J. Ong. Stress projection for membrane and shear locking in shell finite elements. *Computer Methods in Applied Mechanics and Engineering*, 51:221–258, 1985.
- [226] B.A. Szabó and I. Babuška. *Finite element analysis*. John Wiley & Sons, 1991.
- [227] S. Timoshenko and S. Woinowsky-Krieger. *Theory of plates and shells*. McGraw-Hill, 1959.
- [228] L. Kudela. Highly accurate subcell integration in the context of the finite cell method. Master’s thesis, Technische Universität München, München, 2013.
- [229] J. Lindemann and W. Becker. Analysis of the free-edge effect in composite laminates by the boundary finite element method. *Mechanics of Composite Materials*, 36(3):207–214, 2000.
- [230] P. Maimi, J.A. Mayugo, and P.P. Camanho. A three-dimensional damage model for transversely isotropic composite laminates. *Journal of composite Materials*, 42(25):2717–2745, 2008.
- [231] P.P. Camanho, C.G. D’avila, S.T. Pinho, L. Iannucci, and P. Robinson. Prediction of in situ strengths and matrix cracking in composites under transverse tension and in-plane shear. *Composites Part A: Applied Science and Manufacturing*, 37:165–176, 2006.
- [232] Y. Guo, M. Ruess, and Z. Gürdal. A contact extended isogeometric layer-wise approach for the buckling analysis of delaminated composites. *Composite Structures*, 116:55–66, 2014.
- [233] M.S. Shephard. Linear multipoint constraints applied via transformation as part of a direct stiffness assembly process. *International Journal for Numerical Methods in Engineering*, 20:2107–2112, 1984.

- 
- [234] R.W. McCune, C.G. Armstrong, and D.J. Robinson. Mixed-dimensional coupling in finite element models. *International Journal for Numerical Methods in Engineering*, 49:725–750, 2000.
- [235] H.M. Song and D.H. Hodges. Rigorous joining of asymptotic beam models to three-dimensional finite element models. *Computer Modeling in Engineering and Sciences*, 85(3):239–277, 2012.
- [236] T.C. Gmür and A.M. Schorderet. A set of three-dimensional solid to shell transition elements for structural dynamics. *Computers and Structures*, 46:583–591, 1993.
- [237] C.R. Dohrmann and S.W. Key. A transition element for uniform strain hexahedral and tetrahedral finite elements. *Mechanics of Advanced Materials and Structures*, 44:1933–1950, 1999.
- [238] E. Garusi and A. Tralli. A hybrid stress-assumed transition element for solid-to-beam and plate-to-beam connections. *Computers and Structures*, 80:105–115, 2002.
- [239] K.S. Chavan and P. Wriggers. Consistent coupling of beam and shell models for thermo-elastic analysis. *International Journal for Numerical Methods in Engineering*, 59:1861–1878, 2004.
- [240] J.A. Evans and T.J.R. Hughes. Isogeometric divergence-conforming B-splines for the steady Navier-Stokes equations. *Mathematical Models and Methods in Applied Sciences*, 23:1421, 2013.
- [241] I. Harari and E. Shavelzon. Embedded kinematic boundary conditions for thin plate bending by Nitsche’s approach. *International Journal for Numerical Methods in Engineering*, 92:99–114, 2012.
- [242] K.Y. Sze, X.H. Liu, and S.H. Lo. Popular benchmark problems for geometric nonlinear analysis of shells. *Finite Elements in Analysis and Design*, 40:1551–1569, 2004.



# Acknowledgements

At the completion of this thesis, I noticed that it's the most difficult part to write, simply because there are so many people and things to thank on my journey to finish this PhD.

Firstly, I would like to thank Prof. Dr. C. Bisagni for supporting this thesis and being my promoter. I am also very thankful to Prof. Dr. Z. Gürdal for giving me the chance of pursuing a PhD in the AeS group. I still remember that almost every time, when we met occasionally in the corridor, you were always asking "Do you have something for a meeting?". Actually, it is a very good way to stimulate a student to work hard.

Special thanks to my daily supervisor Dr. Martin Ruess, without your patience and continuous support I never would have finished my PhD within four years. The most frequently words you said to me were "Any results?" which I think has the same effect as Professor Gürdal's words. I will never forget the time we spent together on discussing, debugging codes and revising papers again and again. Your enthusiasm on computational mechanics encouraged me during my PhD study.

I would also like to thank Dr. Mostafa Abdalla for the constructive suggestions and fruitful discussion on my work. I am really enjoyed every talk with you.

My gratitude also goes out to Professor C. Vuik, Professor S. Klinkel, Professor L. De Lorenzis, Dr. A. Reali and of course, Professor Rothwell for kindly agreeing to devote time and effort to acting as the committee members.

Many thanks to my office mates: To Attila, thanks for taking the responsibility to teach me isogeometric analysis and for your valuable input to the first paper I published. To Zhenpei, Sonell, Ali, Martin, Fardin, Darun, Huy, Linus, Adriaan, Nils, Jusuf, it was my pleasure to share an office with you and it was definitely a good time together. Thanks to Laura for helping me with lots of administrative things. My gratitude also goes out to the group members: Professor Arbocz, Jan, Sergio, Christos, Roeland, Gillian, Javad, Julien, Eddy, Louis, Weiling, Ke, Dan, Zhi, Luca, Sathis, Jaco, Juriij, Sam, Sourena, Daniël, Noud, Erik, Kris, Mohammed, JP, Etana, Lars and of course to all other members not mentioned in this incomplete list of colleagues.

---

During my four years study at Delft, I have been very lucky to make many good friends, especially my room mates. I definitely had a good time with all of you, often discussing all things of life, politics, economics, culture, arts, traveling etc.

I am very grateful for the financial support provided by the Chinese Scholarship Council. In particular, I would like to thank Prof. Wencheng Tang who was my supervisor during my master studies in Southeast University, China.

To Miranda Aldham-Breary: thank you very much for teaching me a pure English, for the careful reading of my papers and my thesis.

Last but never least, I would like to express my gratitude to my parents and my wife Mengyuan. Without your love and support I could not have come this far.

# Curriculum Vitae

Yujie Guo was born on April 6th, 1986, in a small city named Gaoyou<sup>1</sup>, famous for its double yolk duck eggs, Jiangsu Province, China. He was educated there until he graduated from high school.

In September of 2004, he started his Bachelor degree at the School of Mechanical Engineering, Nanjing Institute of Technology, majoring machine design. During his Bachelor's study, he became very interested in mechanical engineering and attended, by chance, the 1<sup>st</sup> creative mechanical design competition held at Southeast University which he found both his expertise and practical abilities needed to be improved. In 2006, he decided to take the Chinese national entrance examinations for post-graduate schools and was enrolled by Southeast University as a master student at the School of Mechanical Engineering in 2008. During his postgraduate study, he joined Prof. Tang's lab after one year of courses and he started to become familiar with the field of structural design and optimization and relevant design tools. At that time, he thought he would never continue studies on to do a PhD and he had a strong aversion to this idea, however, reality is sometimes dramatic.

In 2011, he decided to pursue a PhD at the Aerospace Structures and Computational Mechanics group of Delft University of Technology where he had the chance to work on the topic of isogeometric analysis and where he had the chance to meet a lot of experts and good colleagues and friends. He started to learn photography, especially landscape photography, in his spare times and traveled to lots of places.

In 2012, he got married in China to his lovely and wonderful wife, and they share each other happiness and sadness in life although much of it has been long distance. With the support of his wife and the knowledge that not even a long distant relationship can pull them apart, Yujie and his wife look forward to the future.

---

<sup>1</sup>A county-level city founded in 223 BC, where the name of the city was related to the establishment of a post office during Ming Dynasty.

---

# List of Publications

## Journal papers:

**Y. Guo**, M. Ruess: “Weak Dirichlet boundary conditions for trimmed thin isogeometric shells.” *Computers and Mathematics with Applications*, **70**: 1425–1440, 2015

**Y. Guo**, M. Ruess: “A layerwise isogeometric approach for NURBS-derived laminate composite shells.” *Composite Structures*, **124**: 300-309, 2015

**Y. Guo**, M. Ruess: “Nitsche’s method for a coupling of isogeometric thin shells and blended shell structures.” *Computer Methods in Applied Mechanics and Engineering*, **284**: 881-905, 2015

**Y. Guo**, M. Ruess, Z. Gürdal: “A contact extended isogeometric layerwise approach for the buckling analysis of delaminated composites.” *Composite Structures*, **116**: 55-66, 2014

**Y. Guo**, A.P. Nagy, Z. Gürdal: “A layerwise theory for laminated composites in the framework of isogeometric analysis.” *Composite Structures*, **107**: 447-457, 2014

N. Xu, W. Tang, Y. Cheng, D. Bao, **Y. Guo**: “Modeling analysis and experimental study for the friction of a ball screw.” *Mechanism and Machine Theory*, **87**: 57-69, 2015

## Conference papers/contributions:

**Y. Guo**, M. Ruess: “Isogeometric design and analysis framework for multi-patch laminate composite shells.” *Invited speaker at 3rd ECCOMAS Young Investigators Conference*, Aachen, Germany, July, 2015

**Y. Guo**, M. Ruess: “A lamina-theory-based model refinement approach for isogeometric thin shells.” *3rd International Conference on Isogeometric Analysis*, Trondheim, Norway, June, 2015

**Y. Guo**, M. Ruess: “Isogeometric weak coupling of shell structures.” *56th AIAA/ASCE/AHS/ASC Structures, Structural Dynamics, and Materials Conference*, Kissimmee, USA, January, 2015

- 
- M. Ruess, **Y. Guo**: “Coupling and boundary constraints for a NURBS-based immersed boundary approach.” *3rd International Workshop on Computational Engineering*, Stuttgart, Germany, October, 2014
- Y. Guo**, M. Ruess: “Weak coupling of thin isogeometric shell structures.” *17th Engineering Mechanics Symposium*, Arnhem, The Netherlands, October, 2014 (poster)
- S. Duckitt, **Y. Guo**, M. Ruess: “Isogeometric modeling of delamination of laminated composite structures.” *27th Nordic Seminar on Computational Mechanics*, Stockholm, Sweden, October, 2014
- Y. Guo**, M. Ruess, Z. Gürdal: “Coupling of laminated composite structures in the framework of isogeometric analysis.” *11th World Congress on Computational Mechanics (WCCM)*, Barcelona, Spain, July, 2014
- M. Ruess, **Y. Guo**: “Weak enforcement of boundary conditions and coupling constraints.” *Sixth International Workshop on Higher-Order Finite Element and Isogeometric Methods (HOFEIM)*, Frauenchiemsee Island, Germany, July, 2014
- M. Ruess, **Y. Guo**: “Coupling of trimmed NURBS patches in the framework of isogeometric analysis.” *85th Annual Meeting of GAMM*, Erlangen, Germany, March, 2014
- Y. Guo**, M. Ruess, Z. Gürdal: “A layerwise approach for the analysis of laminate composites in the framework of isogeometric analysis.” *IGA 2014 - Isogeometric Analysis: Integrating Design and Analysis*, Austin, USA, January, 2014
- Y. Guo**, M. Ruess, Z. Gürdal: “A contact extended isogeometric layerwise approach for the buckling analysis of delaminated composites.” *16th Engineering Mechanics Symposium*, Lunteren, The Netherlands, October, 2013 (poster)
- Y. Guo**, M. Ruess, Z. Gürdal: “An isogeometric layerwise approach for the buckling analysis of composite laminates with delaminations.” *17th International Conference on Composite Structures*, Porto, Portugal, June, 2013
- Y. Guo**, A.P. Nagy, Z. Gürdal: “Model adaptation approach for composite laminates based on isogeometric refinement.” *54th AIAA/ASME/ASCE/AHS/ASC Structures, Structural Dynamics, and Materials Conference*, Boston, USA, April, 2013
- Y. Guo**, A.P. Nagy, Z. Gürdal: “Model adaptation approach for composite laminates based on isogeometric refinement.” *15th Engineering Mechanics Symposium*, Lunteren, The Netherlands, November, 2012 (poster)
- Y. Guo**, A.P. Nagy, Z. Gürdal: “An isogeometric layerwise model for composite laminates.” *3rd Aircraft Structural Design Conference*, Delft, The Netherlands, October, 2012